Experimental Investigation of Multi-Component Jets Issuing from Model Pipeline Geometries with Application to Hydrogen Safety

by

Majid Soleimani nia
B.Sc., Islamic Azad University, Iran, 2002
M.Sc., Eastern Mediterranean University, Turkish Republic of North Cyprus, 2010

A Dissertation Submitted in Partial Fulfillment of the
Requirements for the Degree of

DOCTOR OF PHILOSOPHY

in the Department of Mechanical Engineering

Experimental Investigation of Multi-Component Jets Issuing from Model Pipeline Geometries with Application to Hydrogen Safety

by

Majid Soleimani nia
B.Sc., Islamic Azad University, Iran, 2002
M.Sc., Eastern Mediterranean University, Turkish Republic of North Cyprus, 2010

Supervisory Committee

Dr. Ned Djilali, Co-Supervisor
(Department of Mechanical Engineering)

Dr. Peter Oshkai, Co-Supervisor
(Department of Mechanical Engineering)

Dr. Adam Monahan, Outside Member
(School of Earth & Ocean Science)

Supervisory Committee

Dr. Ned Djilali, Co-Supervisor
(Department of Mechanical Engineering)

Dr. Peter Oshkai, Co-Supervisor
(Department of Mechanical Engineering)

Dr. Adam Monahan, Outside Member
(School of Earth & Ocean Science)

ABSTRACT

Development of modern safety standards for hydrogen storage infrastructure requires fundamental insight into the physics of buoyant gas dispersion into ambient air. Also, from a practical engineering stand-point, flow patterns and dispersion of gas originating from orifices in the side wall of circular pipe or storage tank need to be studied. In this thesis, novel configurations were considered to investigate the evolution of turbulent jets issuing from realistic pipeline geometries. First, the effect of jet densities and Reynolds numbers on vertical jets were investigated, as they emerged from the side wall of a circular pipe, through a round orifice. The resulting jet flow was thus issued through a curved surface from a source whose original velocity components were nearly perpendicular to the direction of the ensuing jets. Particle image velocimetry (PIV) and planar laser-induced fluorescence (PLIF) techniques were employed simultaneously to provide instantaneous and time-averaged flow fields of velocity and concentration. The realistic flow arrangement resulted in an asymmetric flow pattern and a significant deflection from the vertical axis of jets. The deflection was influenced by buoyancy, where heavier gases deflected more than lighter gases. These realistic jets experienced faster velocity decay, and asymmetric jet spreading compared to round jets due to significant turbulent mixing in their near field.

In addition to that, horizontal multi-component jets issuing from a round orifice on the side wall of a circular tube were also investigated experimentally by the means of simultaneous velocity and concentration measurements. A range of Reynolds numbers and gas densities were considered to study the effects of buoyancy and asymmetry on the resulting flow structure. The realistic pipeline jets were always exhibited an asymmetry structure and found to deflect about the jet's streamwise axis in the near field. In the far field, the buoyancy dominated much closer to the orifice than expected in the axisymmetric round jet due to the realistic leak geometry along with the pipeline orientation considered in this study. In general, significant differences were found between the centreline trajectory, spreading rate, and velocity decay of conventional horizontal round axisymmetric jets issuing through flat plates and the pipeline leak-representative jets considered in the present study.

Finally, the dispersion of turbulent multi-component jets issuing from high-aspect-ratio slots on the side wall of a circular tube were studies experimentally by employing simultaneous PIV and PLIF techniques. Two transversal & longitudinal oblong geometries in respect to the longitudinal axes of the tube , and with an aspect ratio of 10 were considered in this study. Both horizontal and vertical orientations along with broad range of Reynolds numbers and gas densities were considered to investigate the effects of buoyancy and asymmetry on the resulting flow structure. The ensuing jets were found to deflect along the jet streamwise axis, once more, due to the realistic pipeline leak-representative configuration. It was also found that increases in aspect ratio of these realistic jets caused a reduction in the angle of deflection, jet centreline decay rates and the width growth on both velocity and scalar fields compared to their round jets counterparts, most notably in the far field.

These findings indicate that conventional jets (those that are issuing through flat surfaces) assumptions are inadequate to predict gas concentration, entrainment rates and, consequently, the extent of the flammability envelope of realistic gas leaks. Thus, extreme caution is required when using conventional jet assumptions to describe the physics of a buoyant jet emitted from realistic geometries.

Contents

List of Tables

List of Figures

ACKNOWLEDGEMENTS

I would like to express my sincere and deep appreciation for the support, guidance and thoughtful consideration provided to me by my co-supervisors, Prof. Ned Djilali and Prof. Peter Oshkai throughout my PhD studies. Their approach has taught me many lessons that extend beyond my research and I am deeply thankful for the opportunity to achieve this personal goal under their supervision. I am also sincerely appreciative for the insightful feedback provided by Prof. Adam Monahan and Prof. Mark Tachie as this information provided additional clarity in my dissertation.

I would also like to extend my appreciation to the wonderful staff at the Institute for Integrated Energy Systems at the University of Victoria (IESVic), Susan Walton, Pauline Shepherd and Peggy White. I would also like to extend a special thank you to my friends and colleagues, Dr. Hadi Vafadar Moradi, Dr. Oleksandr Barannyk, Dr. Hamed Akbari Khorami, Dr. Alireza Akhgar, Mr. Jonathan Reaume, Mr. Andrew Richards, Mr. Mostafa Rahimpour, Mr. Razzi Movassaghi and Mr. Arash Ashtiani.

Further to this, I would like to thank Mr. Krishna Ravi for his contributions to the initial design of experimental system. In addition, I would like to thank Dr. Jay Sui and Dr. Te-Chun Wu for sharing their expertise in experimental fluid mechanics during the initial stages of the project. A special thank you is also extended to Dr. Brian Maxwell for sharing his expertise in numerical fluid dynamics and for the development of LES simulation, which complemented this experimental work. Thank you also to Dr. Steve Anderson from LaVision Inc., who helped me to overcome the challenges related to measurement techniques that were used in this study.

My deepest appreciation goes to my amazing wife, Ms. Laurie Barnas, my loving parents and supportive sisters, as well as their extended families. They have provided me with an unlimited source of encouragement, patience and understanding that sustained me through my PhD studies.

I would also like to extend my appreciation to the Natural Sciences and Engineering Research Council of Canada (NSERC) for their financial support.

DEDICATION

To Laurie,
my wonderful wife,
whose unconditional love, endless support and encouragement
made it possible for me to complete this work,
and to my beloved parents and sisters,
Mahmoud, Shokat, Marjan, Mojgan, and Mina,
who have always offered me their infinite love and encouragement during
my graduate studies journey.
I am forever grateful for having you all in my life.

Chapter 1

Introduction

1.1 Background and Motivations

Global reliance on fossil fuels has resulted in unprecedented build up of atmospheric carbon dioxide and global warming. Achieving clean, safe and sustainable energy is key to reducing carbon emissions and mitigating greenhouse effects. Technologies that enhance sustainability rely on renewable energy sources (i.e. wind energy, solar energy, geothermal energy, wave power, tidal power, hydroelectricity) and can be used to produce hydrogen, as a renewable energy vector.

Hydrogen is the simplest, and also the most plentiful element in the universe – though not readily available in its molecular form on earth. Hydrogen has high energy capacity, and is a carbon-free energy carrier; it can burn in an engine with almost no pollution or it can be consumed in electrochemical cells (fuel cells) to power vehicles and electrical devices. It therefore has the potential to be a key solution for renewable energy storage.

Worldwide attempts continue to improve the production of renewable energy as an alternative energy for traditional power supply in the grid. However, peak period shortfalls and the intermittent nature of some types of renewable energy sources do not offer similar reliability. This increases the need to store renewable energy when it is available. Short term storage can be handled with batteries, but these do not have the capacity to store enough energy to supply the grid beyond several days, and as such, batteries are a limited solution. Pumped-hydro energy storage (PHES) can be helpful if there are no geographical and cost limitations, but these factors often introduce challenges as well. "Virtual storage" made possible by emerging smart grid technologies and advanced demand response control are being developed with some success [7].

The only other realistic large-scale storage option is storing energy in a gas system, also known as power-to-gas technology [38]. Surplus energy generated by renewable sources is used to produce hydrogen from water, among other sources. The hydrogen is then stored and later injected into the natural gas grid or sent to hydrogen infrastructure reservoirs. It can either be used in PEMFC fuel cells to create electricity directly, burned in an engine to power vehicles, or converted to methane and used to power conventional gas turbine generators.

Modern safety standards for hydrogen storage infrastructure must be assured before widespread public use of hydrogen can become possible for PEMFC fuel cells and other end-uses. To develop these new safety standards and to properly predict the phenomena of hydrogen dispersion, a better understanding of the flow structures associated with hydrogen outflow from pipelines or compressed vessels, as well as the resulting flammability region must be achieved. Knowledge of the flammable envelope surrounding a site of an uncontrolled hydrogen release can be estimated from the concentration field. The levels of hydrogen concentration in the air where it is capable of producing a flash of fire in the presence of an ignition source (e.g. arc, flame, spark, and heat) are known as the Lower Flammable Limit (LFL) and the Upper Flammable Limit (UFL). Table 1.1 shows the LFL and UFL limits of hydrogen with other common fuels. In an accidental dispersal of hydrogen, if it is not ignited immediately or is above its UFL on release, it will form an unconfined vapour cloud over a large area which is a very serious hazard. The H_2 concentration will decrease when it is mixed with ambient air as long as dispersion continues. However the risk of hydrogen ignition is negligible, even in the presence of ignition sources, after its concentration falls below the LFL.

The behaviour of the hydrogen jet flow, when released in an enclosure, depends on different parameters (e.g. initial conditions, jet geometry, jet aspect ratio, enclosure geometry, obstacles, and ventilation). In this dissertation, the effects of the initial conditions along with jet geometry and aspect ratio are investigated using measurements and numerical simulations. Also, from a practical engineering stand-point, flow patterns and dispersion of gas originating from orifices in the side wall of circular pipe or storage tank need to be studied. To date, and to our knowledge, no such investigation has been formally researched and published. For this reason, the subsonic release of hydrogen through possible leak geometries from a pipe surface

Table 1.1: Flammability limits of several fuels in air and oxygen, obtained from [19]

Gas or vapour	Limits in air, volume %		Limits in O_2, volume %		O_2 percentage below which no mixture is flammable	
	Lower	Higher	Lower	Higher	N_2 as diluent of air	CO_2 as diluent of air
Hydrogen	4.0	75	4.0	94	5.0	5.9
Carbon monoxide	12.5	74	15.5	94	5.6	5.9
Methane	5.3	14	5.1	61	12.1	14.6
Ethane	3.0	12.5	3.0	66	11.0	13.4
Propane	2.2	9.5	2.3	55	11.4	14.3
Butane	1.9	8.5	1.8	49	12.1	14.5
Hexane	1.2	7.5	——	——	11.9	14.5
Ethylene	3.1	32	3.0	80	10.0	11.7
Benzene	1.4	7.1	——	——	11.2	13.9
Methanol	7.3	36	——	——	10.3	13.5
Ethanol	4.3	19	——	——	——	——
Toluene	1.4	6.7	——	——	——	——
Acetone	3.0	11	——	——	13.5	15.6
Benzine	1.1	——	——	——	——	——
Gasoline	1.4	7.6	——	——	11.6	14.4
Natural gas	4.8	13.5	——	——	12.0	14.4

was experimentally simulated using helium as a substitute working fluid. The research presented in this dissertation seeks to provide insight into the flow structure of turbulent multi-component jets issuing through realistic pipeline leak geometries. Specifically, a state-of-art experimental system was designed and implemented to accurately predict the gas concentration levels and entrainment rates and, consequently, the extent of the flammability envelope of realistic gas leaks was realized.

To summarize, the main aim of this study is to provide a comprehensive measurement dataset in the absence of a complete and accurate experimental database. Thus it can be a prime tool for validation of CFD codes or analytical models that cover the relevant range of realistic conditions which can be found in hypothetical accidental leak scenarios.

In the following section (1.2), a brief summary of the literature review for turbulent jets is discussed, whereas a more detailed discussion on the related studies and findings are provided in chapters 3, 4 and 5.

1.2 Turbulent Jets

The flow is considered jet flow when a single fluid stream dispersed and released in an ambient environment, creating a shear layer (or mixing zone) between the entering and ambient fluids, which results in a mixing of jet fluid with ambient fluid. In general, jets are produced by a continuous source of momentum, and become turbulent above a critical Reynolds number ($\sim Re > 10^3$). Turbulent jets have been the centre of attention in the scientific community, due to their ability to effectively mix entrained fluids at a molecular scale and serve a wide range of applications in different engineering industries (e.g. aerospace, chemical and mechanical). A recent review on round turbulent jets [5] (where the turbulent flow issues through a round orifice) presents experimental and numerical advances over the course of the last 86 years, starting with the work of Tollmien (1926) [118]. In general, axial regions of the axisymmetric round jet can be defined as: the near field, the intermediate field and the far field. In the near field, at the jet orifice, the mixing zone is established upon dispersing the jet fluid into the ambient fluid, which has caused the development of turbulence flow structures. The initial mixing zone (or shear layer) is thin highly unstable, as axial gradients are much smaller than radial gradients. The instabilities originating at the jet orifice, produce vortical structures, which will roll up and then pair-up. As a result, strong turbulent fluctuations are created and continuous growth of the shear layer can be observed downstream. Consequently, the jet spreads radially outward and the width of shear layer increases as the jet velocity decreases downstream. Along the centre of the jet, in the near field region, is a characteristic feature known as the potential core, where almost uniform mean velocity can be expected. However, at the end of the near field region, the shear layers are expanded towards the jet centreline and merged together, and eventually the potential core vanishes. The near field region originates at the jet orifice and can be expanded axially downstream by a distance of up to 7 times the diameter of the nozzle [5], depending on the initial jet conditions.

Beyond the near field region, turbulent coherent structures continue to evolve and interact within the intermediate field region which is axially located downstream by a distance of 7 to 70 diameters from the nozzle [5]. This transitional region, located between the near and far fields, is believed to be the main player in governing the development of jet flow along with the near field region, and is strongly influenced by the initial jet conditions and Reynold number [34]. It is at these near and intermediate regions that varying upstream conditions have vital impacts on both the velocity and scalar fields, and result in the ability to control the development of the jet flow. Previous studies on this region of non-reactive turbulent jets reveal that jet flow, with a minimum Reynolds number of $Re \simeq 10^4$, experiences significantly enhanced turbulent mixing compared to lower Reynolds numbers [24, 34, 5].

In the far field region, located downstream a distance beyond 70 times the diameter from the nozzle [5], the flow becomes self-similar (or self-preserved) when the flow statistical quantities can be assumed by simple scale factors which depend only on one of the variables. Consequently, both velocity and scalar pseudo-similarity solutions, in constant or variable density jets, evolve in similar ways when appropriate similarity variables have been used [83, 85, 15]. However, it is well known that the turbulent structure throughout the entire flow field is particularly influenced by the initial jet outflow conditions. As a result, different self-similarity states in the far field are possible [35, 77]. In the following sections (1.2.1, 1.2.2 and 1.2.3), the effect of buoyancy, initial conditions and nozzle geometry on the turbulent jet flow are discussed briefly, respectively. More detailed discussion of these important parameters and their effects on turbulent jets are provided in chapters 3, 4 and 5.

1.2.1 Buoyant Jets

In variable density jets, whether the jet fluid has a lower or higher density compared to the ambient fluid, buoyancy force plays a significant role in the development of jet flows. The flow field of a turbulent buoyant jet can be classified according to the relative strength of the initial momentum flux (M) and the initial specific buoyancy flux (B). It becomes a pure jet when B is smaller than M; it is considered a steady plume when M is negligible compared to B. On the other hand, it is a buoyant jet when the importance of these two parameters, B and M, are comparable. In general, the three distinct regions of a turbulent buoyant jet can be defined as: the non-buoyant jet region (NBJ), the intermediate or buoyant jet region (BJ) and the buoyant plume region (BP) [15]. The non-buoyant jet region (NBJ), where B is not important, occurs near the jet exit. The flow field in this region develops similar to a pure, momentum-driven jet, and can be similarly analysed. The following region, the intermediate or buoyant jet region (BJ), exists where B and M play equally significant roles in governing the characteristics of the jet. Beyond the BJ region, the buoyant plume region (BP) occurs far from the source. In this region, the effects of M

are negligible and the effect of buoyancy (B) becomes dominant, and the plume-like scaling is perceived in the flow field.

To quantify the axial extent of these regions, the following non-dimensional buoyancy length scale (along the jet axial coordinate, x-axis) [15] can be used:

$$x_b = Fr^{-\frac{1}{2}}(\frac{\rho_j}{\rho_\infty})^{-\frac{1}{4}}x \tag{1.1}$$

where the Froude number is Fr ($= \frac{\boldsymbol{u}_j^2\rho_j}{(\rho_\infty-\rho_j)gD}$), $\boldsymbol{u}$ represents the mean velocity, g is the acceleration due to gravity, D refers to the diameter of jet orifice, ρ is the density of the fluid, and the subscripts 'j' & '∞' refer to the conditions at the nozzle and ambient areas, respectively. The flow is in the non-buoyant jet region (NBJ) when $x_b \leq 0.5$, whereas for $x_b \geq 5$, the jet flow is in the BP region and plume-like scaling pertains. It should be noted that based on data acquisition domains ($0 < x < 40D$) and flow parameters (Table. 2.1) in the current measurements, all experiments are only extended through the NBJ and BJ regions.

1.2.2 Initial Conditions

As previously discussed, the initial outflow conditions of a jet play a remarkable role in governing the turbulent structure throughout the entire flow field [35, 77]. In general, the initial conditions of a jet can be defined by the initial radial profiles of mean velocity and turbulence intensity, the density ratio of the jet fluid to ambient fluid ($R_\rho = \frac{\rho_j}{\rho_\infty}$), as well as the Reynolds number at the nozzle. Practically, different nozzle types are commonly used to introduce a distinctly different initial conditions in the jet flow, defined as: sharp-edged orifice plate (OP), smooth contraction (SC) and a long pipe (LP). Among these three different nozzle types, the most detailed research has been performed on SC nozzles [131, 83]. It has been shown that SC jets have a nearly laminar flow profile at the jet exit with a uniform 'top-hat' velocity profile. LP nozzles [85, 86, 77], on the other hand, produce a nearly Gaussian velocity profile due to fully developed turbulent conditions at the pipe exit. These jets also have thicker initial shear layers compared to SC jets. Sharp-edged OP jets have received recent attention in the last decade, where detailed measurements [74, 89] have revealed that this configuration has the highest mixing rates downstream from the release nozzle. The saddle-back radial velocity profile has always been observed at the OP jet exit.

There has been a remarkable amount of experimental and numerical investigation into the effects of initial conditions on the axisymmetric round jets [10, 77, 89, 3, 76, 133, 95, 93]. It has been well established that the mean centreline decay and mean spreading, in both velocity and scalar fields, experience the highest rate in the OP jet and lowest rate in the LP jet. Also, a significantly higher generation rate of primary vortical structures has been observed in the OP jet compared to the SC jet; whereas the vortical structures in the LP jet, if any, have a considerably lower coherence. These coherent vortical structures are found to be distributed more asymmetrically, with respect to the axis of the jet, in the OP jets compared to the SC jets. Consequently, the OP jet flow experiences more complex three dimensional structures, and a higher turbulent mixing rate is expected downstream of the OP jet compared to the other two nozzle types. In addition, the shortest length of the potential core is found in the OP jet, followed by the SC jet, and then the LP jet which has the longest potential core length.

On the other hand, in the far field region, the flow field is believed to attain a self-similarity (self-preservation) state. However, whether this asymptotic state is universal or influenced by the initial conditions continues to be debated in the scientific community. Based on classical views (e.g. [50, 119]), the asymptotic values that describe the flow field are independent of the initial conditions, except for the addition of the rate of momentum. In contrast, an analytical study [35] suggests that turbulent structures throughout the entire flow field are particularly influenced by initial jet outflow conditions. As a consequence, different self-similarity states in the far field are possible [35]. The latter hypothesis of the local self-similarity has been supported through experimental and numerical studies, and suggests that a universal self-similarity state of turbulence is unlikely to exist [10, 77, 27]. Nevertheless, a comparative review of the studies on turbulent jets and plumes [13] proposes that jets and plumes have different states of partial or local self-similarity. But, the global evolution of jets and plumes have a tendency to evolve towards complete self-similarity through a universal route, in the far-field [13]. However, this recent hypothesis requires qualification. More detailed discussion on self-similarity states of turbulent jets and results of current studies are provided in chapter 4.

1.2.3 Nozzle Geometry

In general, the geometry of a jet nozzle can be divided into round and the non-circular geometry categories. In the following sections (1.2.3-1.2.3) the effects of nozzle geometry on the development of a jet flow are briefly summarized. More in-depth discussions on this important parameter are further detailed in chapters 3, 4 and 5.

Round axisymmetric nozzle

The round nozzle can be found in many engineering applications due to its simplicity and economical production. Also, owing to its simple geometry and axisymmetric nature, which has made measurements and numerical simulations along with statistical analyses much easier, the round jet has received extensive investigation and attention in the last couple of decades [5]. A round turbulent jet can be produced by emanating the jet fluid through a circular orifice from the OP, SC or LP type nozzles into ambient fluid. However, as just discussed, the entire flow field is significantly influenced by different initial conditions associated with different types of nozzles.

Classical scientific research has been limited to jet flows through flat surfaces, where the direction of the jet mean flow was aligned with the flow origin. Thus far, much is known about the axisymmetric and self-similar nature of such jet configurations, emerging through round holes. Round jet behavior is described through self-similarity of statistical analysis of many physical experiments [26, 59, 39, 104, 85, 86, 82, 83, 56, 2, 25, 111, 20] and numerical simulations [10, 21, 112, 11, 17, 113], for a wide range of initial conditions and gas densities. It should be noted that most of the discussions described in previous sections belong to round turbulent jets.

Non-circular asymmetric nozzle

As just discussed, most studies on turbulent jets have focused on the axisymmetric round jet, and fewer investigations have been carried out on non-circular asymmetric (e.g. planar, rectangular, elliptical, et cetera) jets. However, owing to their wide range of application in different engineering industries (e.g. aerospace, chemical and mechanical), there are a considerable number of studies on non-circular jets [44, 91, 136, 75, 78, 115, 40, 30, 42, 22, 23]. These jets are well-known to entrain ambient fluid more effectively than their axisymmetric round jet counterparts, and as a result, more enhanced mixing occurs in these types of flows [43]. Among all non-circular geometries, only plane jet flows can be characterized as a two-dimensional flows, and the three-dimensionality in the coherent structure of flow becomes the main characteristic of other non-circular jet flows.

The three-dimensionality of a non-circular jet flow results either with the non-uniform curvature of the nozzle perimeter or with the instabilities that originate by the sharp perimeter of the nozzle. Consequently, the enhanced mixing is believed to be associated with a higher degree of three-dimensionality in the coherent structures of the non-circular jet flow, where the asymmetrical streamwise and azimuthal vorticity act as the key player in entraining the ambient fluid. As the jet spreads, deformation dynamics of asymmetric vortices yield a complex topology, which results in the interaction of streamwise and azimuthal vortices and the associated energy transfer between them. This "axis-switching" phenomena has been observed in the evolution of non-circular jets [43, 75], as jets cross-section can frequently develop into shapes similar to those of the origin nozzle but with axes sequentially rotated at angles characteristic of the nozzle geometry.

The non-circular jet flow can be adequately characterized by a new length-scale, namely, equivalent diameter (D_{eq}) [55]. Here, D_{eq}, refers to the diameter of an equivalent circle with the same area as the nozzle. In the near field, the mean velocity and turbulence intensity experience much higher decay rates compared to the axisymmetric jet. Those jets experiencing axis-switching phenomenon are believed to exhibit higher decay rate of centreline velocities. Like other jet flows, the overall flow development of non-circular jets is significantly influenced by the initial conditions. Despite the nozzle geometry, different initial conditions associated with the nozzle types attributes to a shorter potential core length has been observed in OP jets compared to SC jets [75, 90, 43]. It has been reported that enhanced mixing in the near-field can be achieved with increasing the nozzle Aspect Ratio (AR) [91]. Aspect ratio refers to the ratio of longer to shorter symmetry axes of the nozzle geometry. Also, the distance from the orifice, where axis-switching phenomenon occurs, increases as the AR of the nozzle becomes greater [55, 91].

1.3 Objectives

In order to quantify the dispersion and development of the jet flow, the first objective was to develop a state-of-art experimental quantitative imaging system. Particle imaging velocimetry (PIV) and acetone-seeded planar laser-induced fluorescence (PLIF) were simultaneously implemented to provide high-resolution instantaneous velocity and concentration fields, respectively. The details of these laser-based imaging techniques, PIV & PLIF, along with a detailed description of experimental system are provided in chapter 2.

The second objective of this dissertation is to quantify the effects of different parameters on resulting flow structures. For this reason, a range of initial conditions (Reynolds number and gas densities), nozzle geometries, and aspect ratios are examined. The fluids considered are air and helium along with two different orientations , vertical and horizontal, for the jet experiments. This allows the effects of buoyancy on evolution of the jet flow to be quantified.

It should be noted that all aforementioned studies on turbulent jets have been limited to the jet flow emerging through flat surfaces, aligned in the direction of the mean flow origin. However, in practical engineering applications (i.e. pipe lines or storage facilities), any accidental gas leakage would not be limited to flows through flat surfaces, and leaks through openings or cracks in the side walls of circular pipes or storage tanks should also receive attention. To address this, the third objective of this dissertation is to experimentally simulate gas dispersion through possible crack geometries in realistic pipeline geometries. The investigation thus considered flow through a curved surface, from a source whose original velocity components are nearly perpendicular to the direction of the ensuing jets. More details regarding the orifice and pipeline geometries used in this study are provided in chapter 2.

The last but not least objective is to demonstrate that conventional round and non-circular jet assumptions are, to some extent, inadequate to predict the correct gas dispersion from realistic geometries. For this reason, the experimental results of these realistic jets are compared with those of axisymmetry and asymmetry jet studies found in the literature, and presented in chapters 3 through 5.

1.4 Main Contributions

This dissertation contributes to the area of fluid dynamics and turbulent mixing for gaseous phases. Specifically, it addresses industry problems related to accidental hydrogen leakage and its associated safety concerns in high pressure vessels or pipelines for both gas transportation lines and storage facilities. Despite the advances made in the area of gas dynamics, there are still a number of issues that require further investigation. The main contributions of this dissertation is the analysis and quantification of the fluid mechanics and associated mass transfer of multi-component jets issuing from nozzle geometries representative of practical pipeline configurations. These results further the understanding of unintended gas dispersion physics and will assist in developing modernized safety standards for hydrogen as a carbon-free energy carrier.

The major contributions of this work are summarized as follows:

1. **Quantify the effects of initial conditions and asymmetry for vertical round realistic jets**: It was found that the realistic pipeline geometry caused the jet to deflect about the streamwise axis of the jet, where heavier gases were found to deflect more than the lighter gases due to the buoyancy effects. This realistic configuration also contributed to the asymmetric flow structures observed within the jet flow, where more jet spreading were observed on the back side of the jets (opposite to the flow direction within the tube) in the near field compared to axisymmetric jets. Upon comparison of these realistic jets with their axisymmetric jet counterparts, a significantly higher mixing rate was observed which is contributed to a reduction in the potential-core length and an increase in the velocity decay rate. Further discussions can be found in chapter 3.

2. **Quantify the effects of initial conditions, buoyancy and asymmetry for horizontal round realistic jets**: Once again, it was observed that the practical configuration selected in this study caused the asymmetric pattern in the evolutions of horizontal realistic jets. It also contributed to the deflection of the jet from its horizontal axis. The buoyant jet deflection in the far field was influenced by the buoyancy force and reproduced well by a power law expression with the exponent ~ 1.3. The experimental results revealed that the buoyancy effects dominated much closer to the orifice than expected in horizontal axisymmetric round jets. Further details can be found in chapter 4.

3. **Identify the axis-switching phenomenon for both vertical and horizontal round realistic jets**: Despite the fact that the orifice geometry is round, axis-switching phenomenon were observed in both horizontal and vertical realistic jet measurements. Like non-circular jet flows, this phenomenon is the main fundamental mechanism for enhanced entrainment properties of realistic jets. Further discussions can be found in chapters 3 through 5.

4. **Quantify the initial conditions and buoyancy effects for both vertical and horizontal high-aspect-ratio realistic jets**: Once again, measurement results revealed significant deflection of the jets from their streamwise axes, where this deflection in the horizontal buoyant jet was found to be reproduced

well by a nearly linear relation (i.e. power law exponent ~ 1) in the far field. Upon comparison of these horizontal high-aspect-ratio jets to their round realistic jet counterparts in the far field, the reduction in the deflection's angle might be solely affected by increasing the aspect ratio. Further discussions can be found in chapter 5.

Contributions of this dissertation are presented in three journal articles (one is already published [107] and the other two are submitted for publication ([108, 109])), three conference papers [105, 72, 106], and two conference oral presentations.

1.5 Thesis Overview

In chapter 2, the methodology used in this dissertation is outlined as a platform to provide the reader with a good understanding of how the research is conducted. The details regarding to the flow and optical facilities, followed by the flow parameters and orifice geometries are provided in the experimental system section (2.1). Later in chapter 2, the fundamentals of quantitative laser imaging techniques (PIV & PLIF) along with their essential parameters used in the current experiments are presented in section 2.2. In the same section, the accuracy of the equipment used and the uncertainties associated with the results presented in this dissertation are discussed.

In chapter 3, the experimental investigation of turbulent jets issuing from realistic pipe geometry is presented. The effect of jet densities and Reynolds numbers on vertical jets are investigated, as they emerged from the side wall of a circular tube, through a round orifice. A large-eddy-simulation strategy was also developed to provide further insight into the experimentally observed trends and the evolution of the flow patterns of these realistic jets [1]. The fluids considered are air and helium for the experiments, and the simulations provided further insight into the behaviour of hydrogen. The purpose is to identify and characterize departures from standard round axisymmetric jet conditions, and to highlight the asymmetric nature of the realistic jets, which ensued from a practical geometry arrangement. To further compare these realistic jets with axisymmetric jets, measurements were also carried out for the same physical jet conditions, and hole diameter, through a sharp-edged orifice plate (OP) type flat surface jet.

[1] The LES complementing the experimental work presented in this thesis was a contribution made independently by a collaborating group member, Dr. Brian Maxwell.

Chapter 4 presents the results of measurements in horizontal turbulent multi-component jets. The fluids considered in this experimental study are air and helium. The objective of this investigation is to quantify the effect of buoyancy and asymmetry on these realistic jets. Therefore, the results are compared to previous studies of vertical jets (presented in chapter 3), issuing from the same pipeline geometry and orifice size. Comparison is also made with horizontal round axisymmetric jets, issuing through flat plates, and other relevant experimental studies in constant and variable density turbulent axisymmetric jets.

To quantify the orifice aspect ratio effect on the evolution of the realistic jets, chapter 5 presents measurements carried out on the turbulent high aspect ratio jets issuing from the same realistic pipeline geometry. These high aspect ratio jets are investigated experimentally in both vertical and horizontal orientations to study the buoyancy and asymmetry effects as well. The results are compared to previous studies on round realistic jets, presented in chapters 3 and 4, as well as relevant experimental studies on non-circular jets issuing from flat surfaces.

Finally, in chapter 6, a summary of conclusions from all dissertation contributions along with recommendations for future research is provided.

Chapter 2

METHODOLOGY

In this chapter, experimental systems and different orifice geometries for all turbulent jets are described in greater details. The fundamental of laser imaging techniques, PIV & PLIF, are also presented along with the definitions of their essential parameters in the current measurements.

2.1 Experimental System

2.1.1 Orifice Geometry

As previously discussed, jets issuing through round holes from flat surfaces have received the most attention in previous investigations due to the well-known axisymmetric and self-similar nature of flow. As a result, all aforementioned studies, and any other related investigations on round jets, are limited to dispersion through flat surfaces, where the direction of the mean outflow was aligned with the flow origin. These studies have generated information of prime importance, assisting in the determination of the dispersive nature of gases, for fuel-safety purposes and also for gas leaks of various hole geometries and inflow conditions. In reality, however, accidental fuel leaks would not be limited to flows through flat surfaces. From a practical point of view, dispersion of gas originating from openings in side walls of circular pipes and their corresponding flow structures should also receive attention.

In the current study, novel configurations were considered to investigate the evolution of jets issuing from realistic pipeline geometries. Here, different orifice geometries were machined in the side of a round seamless brass tube, to create different and more leak-realistic conditions. The tube was closed at one end, and has a characteristic

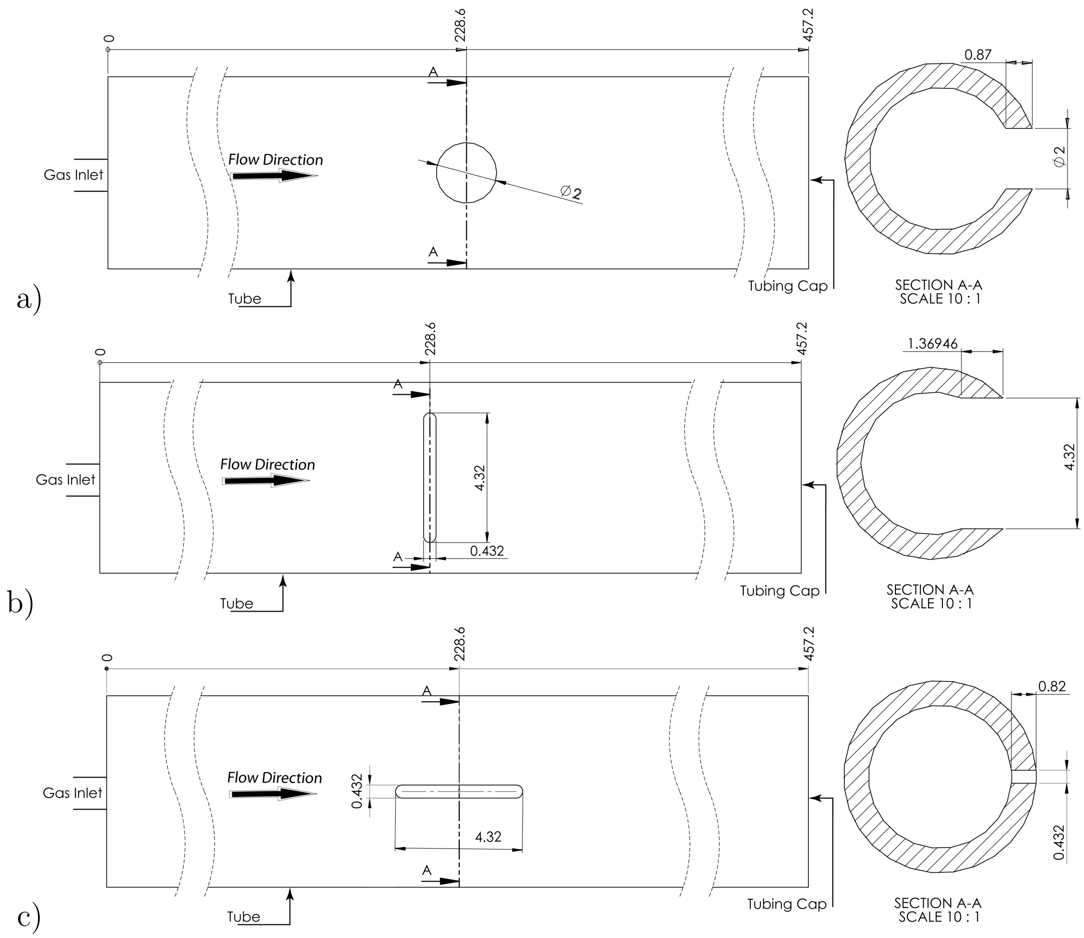

Figure 2.1: Schematics of 3D jets and orifice geometries, a) Round 2mm orifice (Slot 1), b) perpendicular slot (Slot 2), and c) parallel slot (Slot 3) with the flow direction within the tube . All dimensions are in mm.

outer diameter of 6.36 mm and 0.82 mm wall thickness. The resulting jet flow was thus issued through a curved surface from a source for which the original velocity components were nearly perpendicular to the direction of the ensuing jets. From now on, this jet configuration will refer as a 3D jet. The 3D jet orientation permits practical flow velocity and concentration field measurements for realistic leak scenarios in a pipeline, gas storage facility and other infrastructure. Figure 2.1 shows the three different orifice geometries considered in this study which emulate possible realistic crack geometries. These orifice geometries are, round 2mm diameter hole, and transversal & longitudinal oblongs in respect to the longitudinal axes of the tube. For ease of identification, these will be labeled, slot 1, 2 and 3 and are referred to as the round orifice, the slot perpendicular to, and the slot parallel with the direction of flow inside the tube, respectively.

The orifice, through which the gas is dispersed, was located sufficiently downstream to ensure fully developed flow conditions within the tube at the orifice location. Depending on the flow and geometric conditions under which the gas leaks occurs, the resulting jets can undergo several flow regimes from supersonic to subsonic. In this study we considered subsonic flow conditions with a fully developed turbulent flow inside the tube. The flow rates considered were sufficient to provide the required amount of tracer particles for both the PIV and PLIF measurements so that a wide range of Reynolds numbers could be studied.

To further compare 3D jets with axisymmetric jets, measurements were also taken for the same physical jet conditions, and 2 mm hole diameter, through a sharp-edged orifice plate (OP) type flat surface jet. Figure 2.2 shows the jet apparatus, which consists of a honeycomb settling chamber and a 45° angle sharp-edged orifice plate with a 2 mm round hole exit diameter. From now on, we will refer to this jet as, OP jet.

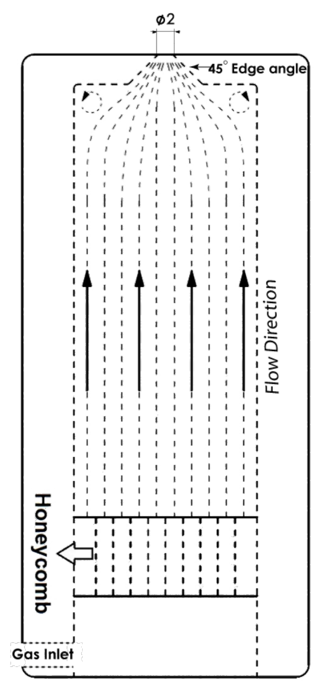

Figure 2.2: Schematic of the sharp-edged orifice jet apparatus, known as the OP jet (dimensions shown in mm).

Table 2.1: Flow properties of the 3D and OP jet experiments

Slot/ Orifice	Jet	Orien- tation	AR	D_{eq} [m]	Q [L/min]	$\langle \boldsymbol{u}_j \rangle_c$ [m/s]	ρ_j [Kg/m^3]	ν_j [m^2/s]	M [N/m]	Fr	Re_δ
1	Air	H	1	2×10^{-3}	15	147.5	1.17	1.54×10^{-5}	50.9	-	19,000
1	Air	V	1	2×10^{-3}	15	147.5	1.17	1.54×10^{-5}	50.9	-	19,000
2	Air	H	10	1.6×10^{-3}	15	169.7	1.17	1.54×10^{-5}	51.7	-	20,300
2	Air	V	10	1.6×10^{-3}	15	170.2	1.17	1.54×10^{-5}	51.8	-	20,300
3	Air	H	10	1.53×10^{-3}	15	209.2	1.17	1.54×10^{-5}	53.3	-	21,000
3	Air	V	10	1.53×10^{-3}	15	208.6	1.17	1.54×10^{-5}	53.2	-	21,000
OP	Air	V	1	2×10^{-3}	15	127.6	1.17	1.54×10^{-5}	38.1	-	16,500
1	He	H	1	2×10^{-3}	35	399.5	0.165	1.21×10^{-4}	51.3	1.34×10^{6}	51,500
1	He	V	1	2×10^{-3}	35	399.7	0.165	1.21×10^{-4}	51.4	1.34×10^{6}	51,500
2	He	H	10	1.6×10^{-3}	35	468.8	0.165	1.21×10^{-4}	52.2	2.4×10^{6}	50,800
2	He	V	10	1.6×10^{-3}	35	469.1	0.165	1.21×10^{-4}	52.3	2.4×10^{6}	50,800
3	He	H	10	1.53×10^{-3}	35	511.4	0.165	1.21×10^{-4}	52.9	2.8×10^{6}	51,600
3	He	V	10	1.53×10^{-3}	35	510.7	0.165	1.21×10^{-4}	52.7	2.8×10^{6}	51,600
OP	He	V	1	1.53×10^{-3}	35	341.9	0.165	1.21×10^{-4}	38.3	9.6×10^{5}	44,200

2.1.2 Flow Conditions

In order to compare the behaviour of both gases in these experiments, the averaged momentum flux (M) at the jet exit was estimated and matched for all 3D slot 1 cases in each setup. This matching was achieved, iteratively, by varying the volumetric flow rate (Q) in the system, after which time, the same Q was considered for both 3D slot 2 and 3 experiments. Here, M was calculated by first obtaining the time-averaged jet exit velocity from the two-dimensional PIV measurements. The two-dimensional momentum flux, in units of [N/m], was then calculated from

$$M = \int_{-D_{eq}/2}^{D_{eq}/2} \rho_j \langle \boldsymbol{u}(r) \rangle^2 \, \mathrm{d}r \tag{2.1}$$

where the subscript 'j' refers to the conditions at the nozzle, the angle brackets '$\langle\ \rangle$' refers to the time-averaged quantity, and ρ and r refer to density and radius, respectively. Table 2.1 shows the flow properties used in this study, for both the horizontal and vertical 3D jet configurations (slot 1, 2 & 3), as well as the vertical round OP jet measurements which have been used for comparison. Here, the subscript 'c' refers to the conditions at the jet centreline, Fr is the Froude number, and H & V refer to horizontal and vertical orientations, respectively. In all cases, the jets were characterized by the outer-scale Reynolds number, $Re_\delta = \langle \boldsymbol{u}_j \rangle \delta / \nu_\infty$. Where, ν_∞ is the ambient fluid kinematic viscosity and δ is the width of the mean axial velocity profile, evaluated from limits of 5% of the centreline velocity at jet exit.

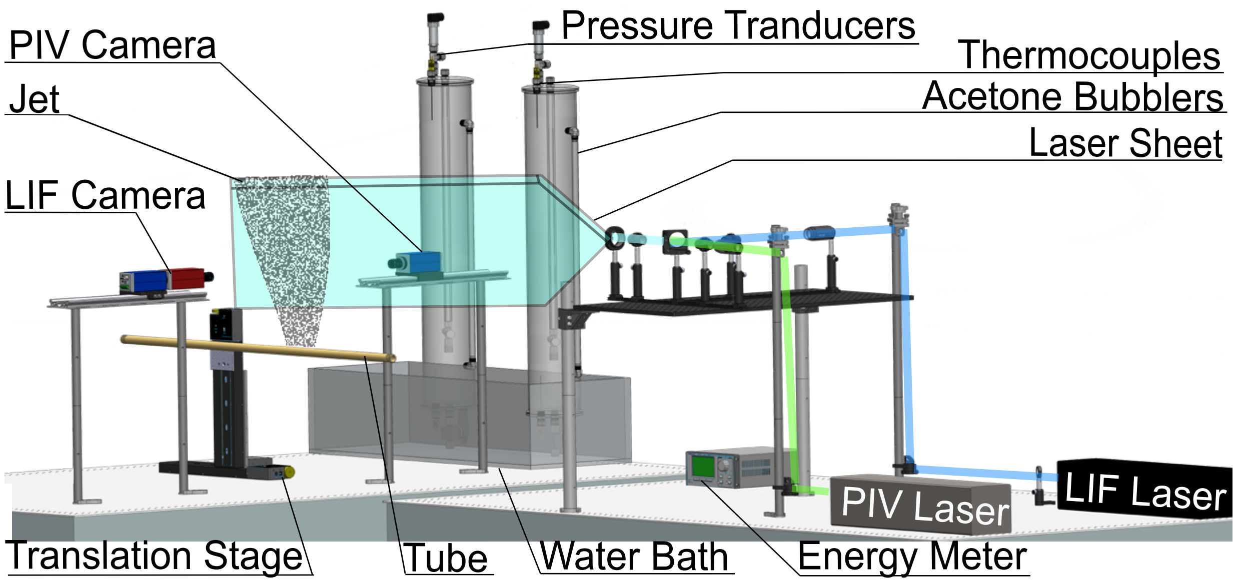

Figure 2.3: Schematic of the experimental layout.

2.1.3 Flow Facility

Figure 2.3, provides a schematic overview of the experimental setup used for this study. The experiments were conducted in a controlled stagnant environment, at room temperature and pressure ($T_o \sim 22^{\circ\mathrm{C}}$, $p_o \sim 100$ kPa). Dry filtered air was supplied by a central flow facility, while pure scientific grade helium was supplied through compressed T-cylinders. Flow controllers (Bronkhorst, EL-FLOW series) were used to control mass flow rates to the system, with a high accuracy (standard $\pm 0.5\%$ of reading plus $\pm 0.1\%$ full scale) and precision (within 0.2% of the reading). For each experiment, the test gas was passed through the PIV seeder (LaVision Aerosol Generator) at a constant pressure to ensure that a consistent amount of tracer particles were present in all tests. Di-Ethyl-Hexyl-Sebacate (DEHS) tracer particles were used, with a typical diameter of less than 1 µm. The test gas was also passed through two 'bubbler'-type seeders. These seeders contained liquid acetone, which was used as a fluorescent tracer for the PLIF. A water bath was used to control the acetone temperature and allow acetone vapours to mix with the test gas isothermally and achieve a saturated state. In all experiments, the test gas was consistently mixed with $\sim 1\%$ acetone vapour by mass fraction. All mixing procedures were controlled by mass flow controllers. The mixing was monitored by pressure transducers and thermocouples at several different locations within the system. Isothermal and isobaric conditions were thus ensured in all experiments. After the test gas was mixed and seeded with the PIV and PLIF tracers, the flow entered the test section of the tube.

2.1.4 Optical facility

As it is shown in Figure 2.3, there were two dual head Nd: YAG pulsed lasers (class IV lasers) used to illuminate the flow field. A New Wave solo PIV compact unit (SOLO III 15 HZ) was used to provide a highly stable green light source with a wavelength of 532 nm for PIV measurements, while a Spectra Physics laser unit (INDI-40-10) provided the ultraviolet light source with a 266 nm wavelength for the PLIF measurements. Each laser beam passed through two different sets of optical lenses, which designed specially based on the laser beam characteristic, creating a light sheet with an approximate thickness of 1 mm and 350 µm for PIV and PLIF measurements, respectively. Then, both laser beams were combined at a dichroic mirror/beam splitter, where 532 nm light was allowed to pass through and ultraviolet light (266 nm) reflected to the measurement plane. Also, 10% of the 266 nm light beam was reflected to the energy meters sensor to register the laser energy per pulse. At the end, both laser beams passed through the last set of cylindrical lenses to create light sheets with an approximate height of 5 cm. Two high resolution CCD cameras, Lavision camera (Imager intense) were used to capture the scattered light from the illuminated flow field. Both CCD cameras have a total resolution of 1376 $\times$ 1040 pixels, 10 Hz frame rate and a minimum time interval of 500 ns between shots. An intensifier unit, a Video Scope image intensifier unit (VS4-1845), was added in front of the PLIF CCD camera to increase the fluorescent signal gain and to control the gating time. Also, a 532 nm bandpass filter with the full width at half maximum (FWHM) of 10 nm was attached to the PIV camera lens to suppress background light, whereas a 378-nm UV bandpass filter with FWHM of 140 nm was attached to the PLIF camera.

2.2 Measurement techniques

2.2.1 Velocity measurements

Particle image velocimetry (PIV) was implemented to acquire instantaneous and time-averaged structures of flow velocity in the current study. The development of PIV, a laser diagnostic technique, capable of capturing velocity information from the whole flow field, originated in the early 1980s. In recent years, PIV has developed to the point where it is now becoming a fairly standard velocity measurement technique, widely employed in a variety of distinct industrial and research applications. This non-intrusive measurement technique ia capable of delivering data with a high temporal and spatial resolution from relatively large 2D- or 3D-flow field sections compared to single-point measurements techniques, e.g. hot-wire anemometry and laser Doppler velocimetry. In this section, only a brief description of PIV fundamentals along with specific parameters are described, as only essential information to properly understand the velocity measurement techniques used in the current study are provided. A detailed description of principle theories and the history of PIV development can be found in [92, 58]

PIV Fundamentals

The major components of a planar PIV system consists of a laser beam formed into a thin light sheet using optical lenses, seeding the flow with tracer particles, which are selected carefully in size and seeding density to ensure that they faithfully follow the flow; the pair of images are recorded using a high resolution CCD camera. Figure 2.4 demonstrates the schematic of the experimental system and includes a flow chart of PIV processing. In general, during a typical planar PIV measurement, a two-dimensional thin light sheet is created by a pulsed laser and illuminates a two-dimensional cross-section of the seeded flow, within a relatively short time interval (Δt). Scattered light from the seeded particles is recorded by a CCD camera at two different times, then the particle displacement field (ideally 5-10 pixels) is measured;

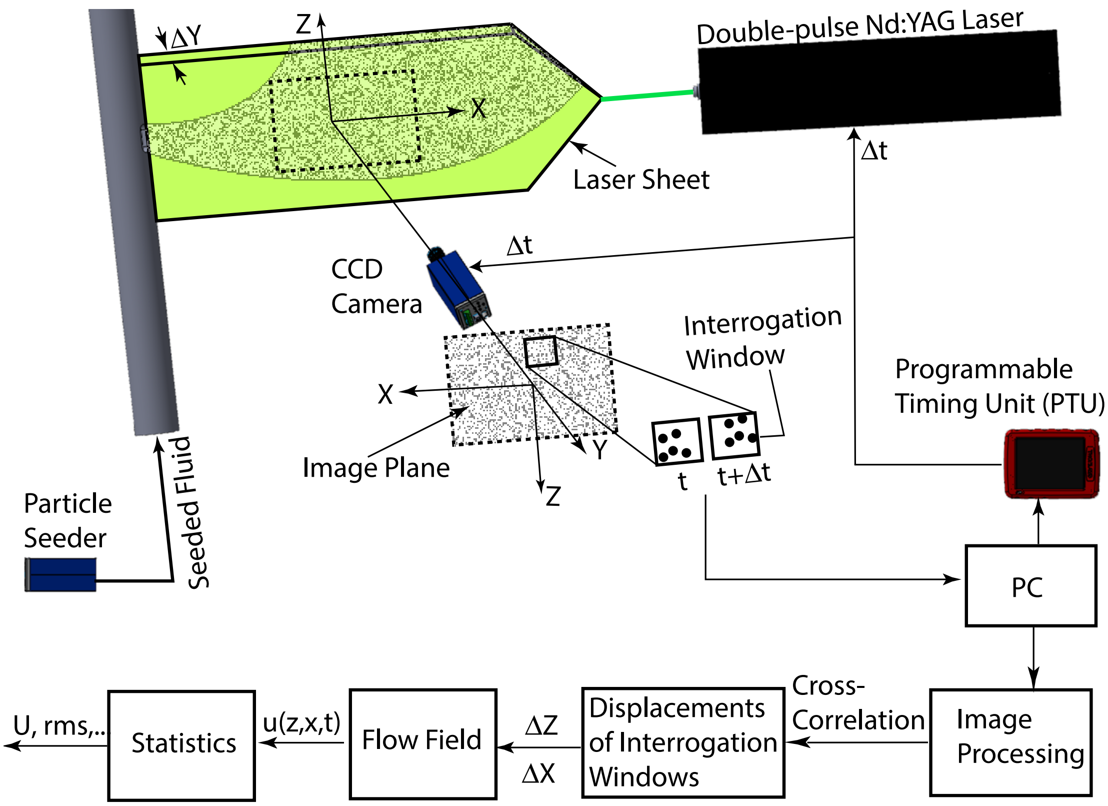

Figure 2.4: Schematic of the experimental system for a planar PIV, and flow chart of PIV processing.

consequently, the local velocity is obtained by particle displacement divided by the time interval Δt.

Tracer particles need to be selected carefully in size and seeding density to ensure that particles are homogeneously distributed within the flow field and also provide an efficient light scattering to obtain sufficient contrast in the recorded images, and most importantly, that they faithfully follow the flow with negligible interference. The Stokes number (Stk), which is a non-dimensional parameter [49], provides a quantitative measure of the flow tracer fidelity and defines how well the tracer particles follow the fluid streamline. Stk is defined as the ratio of the particle's characteristic time (particle relaxation time) to the velocity field's characteristic time, given by:

$$Stk = \frac{\tau \boldsymbol{u}}{L} = \frac{\rho_p d_p^2 C_c}{18\mu} \frac{\boldsymbol{u}}{L} \tag{2.2}$$

where τ is the particle relaxation time, which can be defined as $\frac{\rho_p d_p^2 C}{18\mu}$, the subscript '$p$' refers to the tracer particle, ρ and d are the density and diameter of the tracer particle respectively, C is the slip correction factor, μ is the dynamic viscosity of the fluid, and $\boldsymbol{u}$ & L are the characteristic velocity and length of the flow respectively. Particles with $Stk >> 1$ do not follow the flow at all, whereas particles having $Stk << 1$ faithfully follow the fluid streamline [92]. Among the many potential tracer particle types of gaseous flows, Di-Ethyl-Hexyl-Sebacate (DEHS) particles were used in the current PIV measurements, with a typical diameter of less than 1 µm. The corresponding Stoke number of DEHS particles was calculated using Eq.2.2, and was in the range of 1.8 - 4.3 $\times 10^{-2}$ for the different flow properties considered in this study (Table 2.1). It should also be noted that the averaged size of the particles in the current imaging system were at least 3-5 pixels to reduce the bias error associated with peak locking in the current PIV measurement.

In order to obtain the straight-line displacement of the tracer particles after recording a pair of two images within a short time interval (Δt), each single image can be divided into smaller interrogation windows (IW), and the local movement of each group of particles for each IW can be statistically determined. In the current study, the discrete cross-correlation method [129], which is implemented in the Lavision DaVis 8.4 software, is used to calculate the particles displacements. In this method, the direct cross-correlation function $\phi'(m,n)$, for two sample regions $f(m,n)$ and $g(m,n)$ in an interrogation window, is given by [129]

$$\phi'(m,n) = \frac{\sum\limits_{m=-\infty}^{\infty} \sum\limits_{n=-\infty}^{\infty} f(m,n) g(m+x, n+y)}{\sum\limits_{m=-\infty}^{\infty} \sum\limits_{n=-\infty}^{\infty} f(m,n) \sum\limits_{m=-\infty}^{\infty} \sum\limits_{n=-\infty}^{\infty} g(m,n)} \tag{2.3}$$

where within an interrogation window with coordinates of m and n, f and g represent the image intensity distribution of the first and second image respectively, and x and y are pixel offsets between the two images. The cross-correlation value approaches to unity if particles in the second image match up with their corresponding shifted particles in the first image. Consequently, the highest correlation peaks in the cross-correlation plane indicates the most probable displacement of the particles in each interrogation window.

Figure 2.5 shows the process of the two frame cross-correlation method, embedded within the commercial software of Lavision DaVis 8.4, used in the current PIV

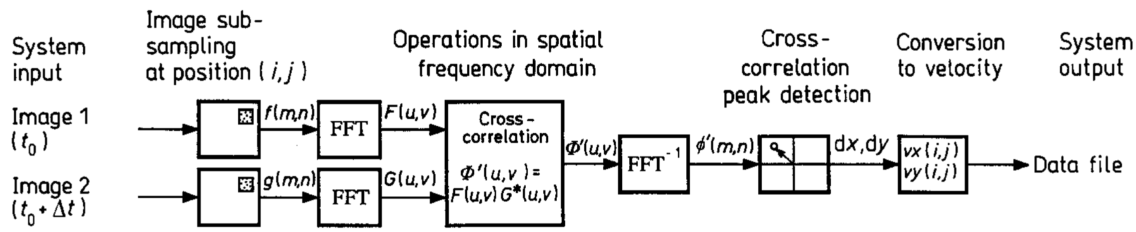

Figure 2.5: Flow-chart of the cross-correlation algorithm based on FFT, obtained from [129]

measurements to obtain the velocity field. In order to simplify and significantly speed up the whole cross-correlation process, Willert and Gharib [129] originally introduced the cross-correlation algorithm based on the Fast Fourier Transform (FFT). In general, this approach reduces the number of cross-correlation operations from $O(N^2)$ to $O(N \log_2 N)$ [129, 92].

It should be noted that implementation of the FFT method comes with some drawbacks, even though it offers a significantly faster computation compared to more direct methods. The first shortcoming of the FFT method is related to its' limitation of the Nyquist criterion, which is associated with the Fourier transform; the maximum displacement magnitude that can be correctly calculated has to be $N/2$, where N is the size of the interrogation window in pixels. However, a more conservative limit of $N/4$ has been widely adopted and is considered as achieving sufficient accuracy in displacement calculations [60, 92]. Second, a proper weighting function needs to be considered for FFT implementation to overcome the biased correlation estimations in the FFT method due to the periodicity of data. All of these issues are properly addressed and implemented in the Lavision DaVis 8.4 software, hence the ability to obtain reliable and highly accurate results in the cross-correlation algorithm used in current study.

Two advanced techniques were used in the present PIV post-processing of the data, an interrogation window overlap and adaptive multi-pass processing, which enhanced the correlation algorithm signal to noise ratio and improved the spatial resolution of calculated vector field. This correlation based correction (CBC) technique, originally introduced by Hart [48], in conjunction with 50% of the neighboring interrogation windows, were used to decrease the effect of false correlation peaks. In this technique, the overlapped regions are multiplied to amplify the common correlation peaks that exist in both the overlapped region and to dampen any erroneous peaks. This results in a decreased number of spurious vectors and enhanced the spatial resolution in calculated velocity fields.

Additionally, the adaptive multi-pass processing technique, which was first introduced by Westerweel [126], was used to rectify the velocity bias. In the region of flow with high velocity gradients, tracer particles within a specific interrogation window in the first image may exit the IW in the second image of the image pair, and as a result, there is a bias in the calculated vector field. To address this, the adaptive multi-pass technique offset the IW according to the mean displacement vector. This iterative process is carried out until the desired resolution is achieved, generally with an incremental decrease of the interrogation window size (e.g. from 32 $\times$ 32 to 16 $\times$ 16 pixels). Upon completion of each pass, using the multi-pass method, a regional median filter was applied to detect and remove any spurious vectors. Finally, in the last pass of the multi-pass processing method, the variable interrogation window size and shape algorithm [127] (A.K.A. as Adaptive PIV, embedded within Lavision DaVis 8.4 software [63]) was implemented to achieve the highest possible accuracy and spatial resolution for the calculated velocity fields.

The PIV post-processing algorithm was kept the same for almost all experiments in this study. Once the velocity field was calculated for each experiment, the Reynold decomposition method was employed to statistically analyse and present velocity results. All pairs of PIV images were acquired at a frequency of 5 Hz, which provides statistically uncorrelated data and proper time spacing for calculating the turbulent statistics in each jet flow [17]. A set of at least 750 images was acquired and based on the convergence of time-averaged quantities, the total number of 500 images was found to be sufficient and was therefore used to calculate statistical quantities. By considering $N = 500$ as the total number of images, time-averaged velocity vectors $\langle u, v\rangle$, and root-mean-square (r.m.s) of the velocity component fluctuations and Reynolds stresses calculated by Eqs.2.4, 2.5, 2.6, and 2.7 respectively.
Time-averaged Velocity:

$$\langle u, v\rangle = \frac{1}{N}\sum_{i=1}^{N}[u_i(x,y), v_i(x,y)] \tag{2.4}$$

r.m.s of u-velocity fluctuation:

$$u_{rms} = \{\frac{1}{N-1}\sum_{i=1}^{N}[u_i(x,y) - \langle u(x,y)\rangle]^2\}^{1/2} \tag{2.5}$$

r.m.s of v-velocity fluctuation:

$$v_{rms} = \{\frac{1}{N-1}\sum_{i=1}^{N}[v_i(x,y) - \langle v(x,y)\rangle]^2\}^{1/2} \tag{2.6}$$

Averaged value of Reynolds stress correlation:

$$\langle u'v'\rangle = \frac{1}{N-1}\sum_{i=1}^{N}[u_i(x,y) - \langle u(x,y)\rangle][v_i(x,y) - \langle v(x,y)\rangle] \tag{2.7}$$

Here, it should be noted that the prime ($'$) represents the instantaneous fluctuating quantity. For example, $u' = u - \langle u\rangle$.

2.2.2 Concentration measurements

Planar Laser Induced Fluorescence (PLIF) is a non-intrusive, spatially resolved laser diagnostic technique that has evolved into a valuable tool for the investigation of scalar flow fields. PLIF is well developed and more frequently used for the measurement of gas species concentrations, however since it utilizes fluorescence sensitivity, it can be employed for measuring temperature, pressure or even velocity in combustion systems. High characteristic signal levels make PLIF an appropriate choice among other alternatives for quantitative single-shot imaging and it can provide temporal resolution of instantaneous flow phenomena. Alternative techniques such as Schlieren, Shadowgraphy, Raman and Rayleigh scattering can also be used for quantitative measurements. However PLIF provides instantaneous information without the line-of-sight averaging that is inherent in Schlieren and Shadowgraph techniques for the entire plane of the flow field. Its' detected signals intensity are higher than those obtained by Raman and Rayleigh scattering, while generally the fact that the use of atomic or molecular fluorescent species always ensures that the tracer tracks the flow. Since the initial development of PLIF was investigated in the late 1970s and early 1980s, the potential of PLIF has been demonstrated in a wide variety of environments. In the following section, a short summary of PLIF fundamentals is detailed, as it is essential complementary information required to adequately understand the scalar measurement techniques used in this study. Further descriptions of theoretical basis and the practical implementation of this technique can be found in [47, 101, 120, 69]

PLIF Fundamentals

The brief principle of PLIF is that the pulsed laser beam is formed into a thin light sheet that illuminates the area of interest in the flow field. The wavelength of the laser light is tuned to excite the particular molecule (or atom) that is artificially seeded (e.g. acetone, biacetyl, I_2) or exists naturally (e.g. O_2, CH, OH, NO in flames) within the flow field as a tracer. Most often, ultraviolet wavelength is used to produce electronic excitation. A fraction of these excited molecules will emit a photon while simultaneously returning to the equilibrium state. This results in measurable fluorescence signals from the tracer and is captured by a CCD camera. An intensifier unit can be added on the front of CCD camera that is sensitive to the ultraviolet light, increasing the fluorescence signal gain and gating capability.

There are several simple fluorescent tracer molecules that have been used to measure concentrations in gaseous flows, e.g. I2, NO, NO2. These molecules have well-characterized spectral properties and can provide good fluorescence signals. However, all of these substances are highly toxic, and I2, in particular is highly corrosive. Other alternative tracers are a number of organic polyatomic molecules, including Biacetyl (CH3-(CO)2-CH3), Acetaldehyde (CH3-CHO), Hexafluoroacetone (CF3-CO-CF3) and Acetone (CH3-CO-CH3). In this study, acetone was used as the tracer for many advantages over other gaseous fluorescing alternatives. Some advantages are: high vapor pressure at room temperature, absorb over a wide band of wavelengths (225-320 nm) and emits fluorescence on even wider broadband of wavelengths (350-550 nm), have a short fluorescence lifetime ($\sim$ 2 ns), negligible oxygen quenching on fluorescence signal, and most importantly, it's fluorescence signal in isothermal, isobaric flows is known to be linear with laser power and concentration[69].

In general, for a weak excitation (not saturated), the fluorescence signal from PLIF can be presented by

$$S_{\mathrm{f}} = n_{\mathrm{tracer}}(T,p)\,\mathrm{d}V_c[\frac{E}{hc/\lambda}]\sigma(\lambda,T)\phi(\lambda,T,p,n_{\mathrm{i}})\eta_{\mathrm{optic}} \tag{2.8}$$

where n_{tracer} is the number density of the tracer, which can be defined as $\frac{pX_{tracer}}{kT}$, X_{tracer} is the tracer (acetone) mole fraction, k is Boltzmann's constant, $\mathrm{d}V_c$ is the collection volume, E is the laser energy fluence, hc/λ is the energy per photon of the laser at wavelength λ, σ is the absorption cross-section of tracer molecule, ϕ is the fluorescence yield, η_{optic} is the collection optics efficiency, and T, p are total temperature and pressure of the tracer, respectively.

In order to obtain a linear fluorescence regime, where Eq.2.8 is applicable, optical lenses were used to create a light sheet with an approximate height of 5 cm and a thickness of 350 µm. This ensured that saturation of the fluorescence signal did not occur until the laser energy per pulse reached $\sim$ 10.4 J, which was well above the maximum laser energy output (55 mJ) used in this study. Also, σ (in Eq. 2.8) is a function of λ and T, and can be defined as a constant since isothermal and isobaric conditions along with the same excitation wavelength ($\lambda = 266$ nm) are considered in all current measurements. The measured value of the acetone absorption cross-section (σ), at room temperature and $\lambda = 266$ nm, is reported to be equal to 4.4 $\times 10^{-20}$ cm^2 [69, 68].

Upon capturing the raw PLIF images, several sets of data are required to convert the raw data to acetone concentration. The only non-constant parameters, in Eq. 2.8, are n_{tracer} (or X_{tracer}), η_{optic}, ϕ and E. To account for the variable laser fluence E, both temporal ($E(t)$) and spatial ($E(x, y)$) laser fluence variations must be corrected through a normalization method in the raw data. Also, one can eliminate the errors associated with variations in the collection optics efficiency (η_{optic}) by correcting the background noise level (dark and background noises) along with optical system distortions (i.e. perspective and vignetting effects). Since all necessary corrections were completed in Eq. 2.8, the local concentration (X_{tracer}) can be defined directly proportional to the fluorescent signal intensity in post-processed PLIF images through following equation:

$$S_{\mathrm{f}} = C X_{tracer} \tag{2.9}$$

where C is the constant factor which is unique to each experiment. In the following section, a brief description of the data correction and image processing algorithms, used in current PLIF measurement, are provided.

Image processing and correction

In this study, commercial Lavision DaVis 8.4 software (Gaseous LIF package [64]) was employed to process the raw PLIF images and convert them to quantitative measurements of scalar concentrations. Figure 2.6 demonstrates the working flow for a single-colour PLIF concentration measurement and an associated image processing algorithm, embedded within the Lavision DaVis 8.4 software, used in current experi-

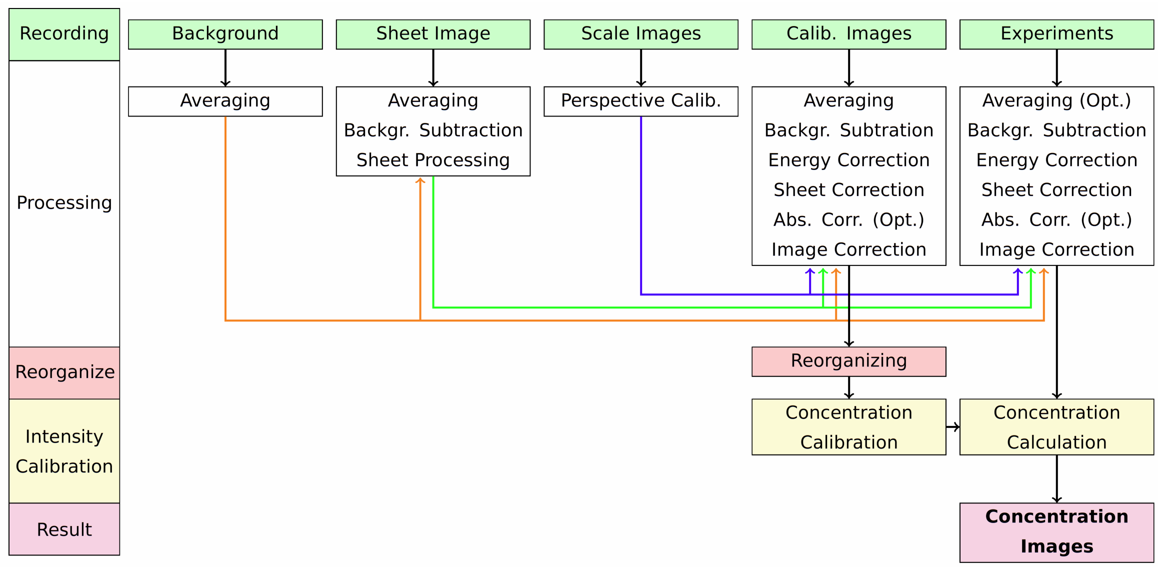

Figure 2.6: Workflow for 1-colour PLIF concentration measurement and image processing algorithm embedded within the Lavision DaVis 8.4 software, obtained from [64]

ments. It should be noted that the order of image processing was kept the same for all measurements and it was completed in the order shown in Fig.2.6.

In order to correct background noise in the raw images, two sets of background images were acquired at the beginning and at the end of each experimental run. These images include the dark background noise level associated with the PLIF CCD camera, the scattered light from laser and associated luminescence caused by object reflections, as well as the environmental light generated by other sources in the experiment's room (e.g. monitor light). In practice, the average of the two background image sets was used for correction, and subtracted from each of the raw images. This correction process corresponds to 'Backgr. Subtraction' in Fig. 2.6.

As just discussed, to quantify the variations of laser fluence (E), both temporal ($E(t)$) and spatial ($E(x, y)$) fluctuations should be considered and correction must be applied to the raw images accordingly. Since the laser energy varies per shot, each PLIF image ($E_{image}(t)$) is registered with an energy meter during the experiments, and all raw images can be corrected for the laser energy's temporal fluctuations ($E(t)$). This intensity correction on each pixel of raw image can be applied with the following expression:

$$I_{corr-energy}(x,y) = I_{image}(x,y)\frac{E_{ref}}{E_{image}(t)} \tag{2.10}$$

where I is denoted as the pixel intensity, E is the measured laser energy per shot, x and y are the coordinates of pixel, and the subscript 'ref' refers to a reference laser energy in the set of measured laser energies $E_{image}(t)$, to be considered for normalization of energy values. This process refers as 'Energy Correction' in Fig. 2.6.

The spatial fluctuation of the laser profile ($E(x,y)$), A.K.A. laser sheet profile, can be quantified by taking measurements in a homogeneously seeded gas mixture with a low and constant concentration of acetone which reveals sufficient signal strength with negligible absorption. Practically, this can be done by taking images from the flow region where the measured signal is uniform and known to correspond to a constant mole fraction X_{tracer}, such as the potential core of a laminar jet. It should be noted that all the experimental settings (i.e. camera arrangement, laser power and optical system settings), in capturing the laser sheet profile should be kept the same as those used for the main measurements. For this purpose, a laminar jet of air seeded homogeneously with a low concentration of acetone vapour with an average of 10 images of the potential core region are taken prior to and at the end of every data acquisition session. The laser sheet correction theory is relied on for keeping the overall intensity of image constant while the PLIF image is normalized by the laser sheet image. In general, the average of both set of laser sheet images ($I_{laser-sheet}(x,y)$) is considered for the local laser sheet correction inhomogeneities. Consequently, all pixel intensities in the PLIF image were corrected for the laser sheet profile variation using following expression:

$$I_{corr-sheet}(x,y) = \frac{I_{image}(x,y)}{I_{laser-sheet}(x,y)}\left[\frac{1}{N_{valid}}\sum_{i=1}^{N_{valid}} I_{laser-sheet}(x_i,y_i)\right] \tag{2.11}$$

where N_{valid} is denoted as the number of valid pixels in the laser sheet image, which is defined based on the relative acceptable intensity threshold and the size of a Guassian smoothing filter used to process the laser sheet image. Therefore, the laser sheet correction is only applied to those pixels in the PLIF images which are the valid pixels in the laser sheet image.

In order to correct for any image distortion caused by camera configuration and the optical system, an image correction based on spatial calibration needs to be applied. For this purpose, a metal grid plate with equidistant dots (1 mm) was located in the imaging plane, and consequently all images were spatially corrected and scaled to physical distances. On the other hand, due to the small amount of acetone concentration used in this study and also the narrow nature of the flow, no significant absorption along the line of laser light was observed. This observation was also assured through checking the fluorescence signal profiles that were aligned with the line of laser sheet, more specifically in potential core regions where the concentration must be constant. Therefore, the flow field was assumed to be optically thin and no absorption correction was applied in this study.

After all image corrections were completed, another set of the calibration images needed to be acquired prior to the conversion of pixel intensity of the processed image to physical molar fraction. It should be noted that these calibration images, called 'Calib. Images' in Fig. 2.6, must be recorded from a mixture with known concentration. Also, all necessary image corrections should be applied to the calibration images, and all experimental conditions must be kept the same as the main measurements. To gain higher precision, it is recommended that the average of 10 images for several different mixture concentrations is considered, where the concentration of tracer is increased slowly and tracer distributed homogeneously in the mixture. This was done by varying the concentration of acetone from zero up to saturation ($\sim 1\%$ mass fraction). Upon mapping the pixel intensities to the known concentrations, the linear model in Eq. 2.9 is employed to determine the constant factor of C. After the constant factor of C in the linear relation of processed fluorescence signal and corresponded molar concentration (Eq. 2.9) was defined, this calibrated data can be applied to all processed PLIF images to convert the fluorescence signal intensities to a concentration image with physical units.

The PLIF image processing algorithm was kept the same for all measurements in this study. All PLIF images were acquired at a frequency of 5 Hz, and timing was adjusted as each PLIF image was taken exactly between a pair of PIV image counterparts. This provided an opportunity to capture instantaneous velocity and scalar images simultaneously. Upon obtaining the instantaneous scalar concentration field for each experiment, Reynold decomposition methods were employed to analyse and present statistical quantities. A set of at least 750 images was acquired and based on the convergence of time-averaged quantities, and also by matching the

PIV data, a total number of 500 images was found to be sufficient and was used to calculate the statistical quantities. By considering $N = 500$ as the total number of images, time-averaged molar concentration $\langle X \rangle$, root-mean-square (r.m.s) of the molar concentration fluctuations and variances calculated by Eqs.2.12, 2.13 and 2.14, respectively.
Time-averaged molar concentration:

$$\langle X \rangle = \frac{1}{N} \sum_{i=1}^{N} [X_i(x, y)] \tag{2.12}$$

r.m.s of molar concentration fluctuation:

$$X_{rms} = \{\frac{1}{N-1} \sum_{i=1}^{N} [X_i(x, y) - \langle X(x, y) \rangle]^2\}^{1/2} \tag{2.13}$$

Molar concentration variance:

$$\langle X'^2 \rangle = \frac{1}{N-1} \sum_{i=1}^{N} [Xi(x, y) - \langle X(x, y) \rangle]^2 \tag{2.14}$$

2.2.3 Measurement uncertainties

There are two main types of errors associated within a measurement system, which are systematic (bias or accuracy) and random (precision) errors. The bias error is harder to quantify and it is an expected error in the measurement of absolute value of quantity. This systematic error can vary across the data field, but would be constant over time in all data sets. In effort to eliminate any known systematic errors, it is recommended to optimize the experimental system in the first place, by enhancing the accuracy of the experimental system components and keeping the level of remaining bias errors insignificant compared to other error sources[18, 92]. In PIV, the bias error is generally attributed to the implementation of a cross-correlation method, peak-finding algorithm and optical system calibration [92, 1]. Whereas the main source of systematic errors in PLIF is due to inaccurate image corrections associated with the collection optics efficiencies and local laser fluence variations.

On the other hand, random (precision) errors are due to unknown changes in the experimental conditions (instruments or environments), and scatter measured data is a most common sign of this type of error. Generally in PIV measurements, the random error is affiliated to the noise in the correlation plane, whereas in PLIF, any noise source associated with an image acquisition (e.g. background, dark and CCD camera readout noises) is attributed to a random error. However, it is not always possible to absolutely distinguish between random and bias errors, and the sum of both errors are usually defined as a total error or as an uncertainty in the measurement data.

If all known systematic errors are assumed to be corrected by an appropriate correction, the remaining errors can be estimated through a-posteriori uncertainty quantification method. In recent years, several uncertainty quantification methods have been developed, more specifically for PIV measurements, and their performances for different flow and experimental conditions are assessed [100]. Among them, a method based on the correlation statics [128], embedded within the Lavision DaVis 8.4 software [63]), was implemented to estimate the error associated with every calculated instantaneous local velocity vector in the flow field. Generally in this method, the standard deviation of intensity variations of each pixel, in a pair of PIV images, to the shape of the correlation function is statistically determined. The calculated standard deviation is then related to the uncertainty of the local displacement field, and consequently to the error for every calculated velocity vector. More details regarding the theory and implementation of PIV uncertainty quantifications using correlation statistics can be found in [128, 63]. For PLIF, upon appropriate corrections implemented on the raw images, the remaining error in the instantaneous scalar field can be correlated to the signal to noise ratio (S/N) variations. The error associated with every instantaneous scalar concentration was estimated from the standard deviation of this ratio in a uniform low signal region of the flow field, where constant signal levels are expected.

Following the estimation of error for every instantaneous velocity and scalar quantity, the uncertainty propagation method is used to propagate the errors into derived statistical quantities [99]. This method is based on the linear error propagation theory [8, 9], and the uncertainty (U) of statistical quantities can be defined through following expressions.
Uncertainty of mean:

$$U_{\langle x \rangle} = \frac{\sigma_{x,total}}{N} \approx \frac{\sqrt{\sigma_x^2 + \langle U_x^2 \rangle}}{N} \tag{2.15}$$

Uncertainty of standard deviation:

$$U_{\sigma_x} = \frac{\sigma_x}{\sqrt{2(N-1)}} \tag{2.16}$$

Uncertainty of variance:

$$U_{\langle x'^2 \rangle} = [\frac{1}{N-1}\sum_{i=1}^{N}(x_i - \langle x \rangle)^2]\sqrt{\frac{2}{N}} \tag{2.17}$$

Uncertainty of Reynolds shear stress:

$$U_{\langle u'v' \rangle} = \sigma_u \sigma_v \sqrt{\frac{1+\rho_{uv}^2}{N-1}} \tag{2.18}$$

where N denotes the number of samples, x is the quantity of interest, ρ_{uv} refers to the cross-correlation coefficient between the u and v components of velocity, $\langle U_x^2 \rangle$ is the mean-square of the uncertainty of the instantaneous quantity (U_x), and σ is standard deviation of the quantity, which can be defined as

$$\sigma_x = \sqrt{\frac{1}{N-1}\sum_{i=1}^{N}[x_i - \langle x \rangle]^2} \tag{2.19}$$

Based on the described methods in this section, the uncertainty is estimated in the presented time-averaged velocity, Reynold shear stresses, time-averaged concentration and variances of concentration field to conservative values of 3%, 6%, 4% and 7%, respectively.

Chapter 3

Experimental and Numerical Investigation of Turbulent Jets Issuing Through a Realistic Pipeline Geometry: Asymmetry Effects for Air, Helium, and Hydrogen [1]

[1] The body of this chapter was published in Majid Soleimani nia, Brian Maxwell, Peter Oshkai and Ned Djilali, International Journal of Hydrogen Energy 43 (19), 9379-9398, 2018, and is reproduced with the permission of Elsevier. MS designed the study and experimental system, conducted the measurements, performed the analysis, drafted the initial manuscript, and finalized the published version. BM developed and implemented the LES simulation, provided the numerical data, and contributed to writing the initial draft and also to the refinement of further manuscript drafts. PO and ND contributed to design of initial study as well as refinement of further manuscript drafts.

3.1 Preamble

Experiments and numerical simulations were conducted to investigate the dispersion of turbulent jets issuing from realistic pipe geometries. The effect of jet densities and Reynolds numbers on vertical buoyant jets were investigated, as they emerged from the side wall of a circular pipe, through a round orifice. Particle image velocimetry (PIV) and planar laser-induced fluorescence (PLIF) techniques were employed simultaneously to provide time-averaged flow velocity and concentrations fields. Large eddy simulation (LES) was applied to provide further detail with regards to the three-dimensionality of air, helium, and hydrogen jets. These realistic jets were always asymmetric and found to deflect about the vertical axis. This deflection was influenced by buoyancy, where heavier gases deflected more than lighter gases. Significant turbulent mixing was also observed in the near field. The realistic jets, therefore, experienced faster velocity decay, and asymmetric jet spreading compared to round jets. These findings indicate that conventional round jet assumptions are, to some extent, inadequate to predict gas concentration, entrainment rates and, consequently, the extent of the flammability envelope of realistic gas leaks.

3.2 Introduction

Worldwide efforts continue to improve renewable energy technologies, as alternatives for traditional power supply in the energy grid and transportation applications. Hydrogen, as one renewable energy vector, can burn or react with almost no pollution. Commonly, it is used in electrochemical fuel cells to power vehicle and electrical devices. It can also be burned directly in engines. However, modern safety standards for hydrogen infrastructure must be assured before widespread public use can become possible. As a result, there has been much focus on advancing research to understand dispersion and ignition behaviour of hydrogen leaks in order to assess associated safety hazards. To date, a number of experiments have shown that hydrogen jets are easily ignitable [123], and have a wide range of ignition limits (between 4% to 75% by volume) [66]. It is therefore of paramount interest to understand the dispersive nature of hydrogen, which is a highly compressible gas, in order to adequately develop codes and standards. The current study addressed, through experimental measurements and numerical simulation, the effect of jet exit conditions on the dispersion of fuel leaks from a realistic pipeline geometry. The piping arrangement considered here was novel, as we examined the dispersion of vertical jets which emerged through a circular hole located in the side wall of a round pipe, perpendicular to the mean flow within the pipe. The aim was to provide insight into the flow structures associated with hydrogen outflow from a realistic fuel leak scenario.

Traditionally, scientific research has been limited to compressible fuel leaks through flat surfaces, aligned in the direction of the mean flow origin. To date, much is known about the axisymmetric and self-similar nature of such jet configurations, emerging through round holes, for a wide range of Reynolds numbers and gas densities. A recent review on round turbulent jets [5] presented experimental and numerical advances for a period of 86 years, starting with the work of Tollmien (1926) [118]. Of these, significant advances in round jet theory have been made possible from statistical analysis of many physical experiments [26, 59, 39, 104, 85, 86, 82, 83, 56, 2, 25, 111, 20]. Where round jet behavior described through self-similarity of statistical analysis, along with those measurements in hydrogen round jets[46, 62] , owing the axisymmetic and self-similar nature of round jets. Advances in computational resources have also allowed numerical simulation, through large eddy simulation (LES), to prove useful for determining entire flow fields of such round jets [21, 112, 11, 17, 113]. In most experiments, data has been collected for air, helium, and CO_2 jets, due to the reactive nature of hydrogen. However, numerical simulation have also proved useful for determining ignition limits associated with hydrogen [17] ; quantifying the effect of initial conditions on the turbulent mixing properties of hydrogen round jets[12] ; and highlighting the need to consider the impact of transient flow structures and associated incursions of high flammability concentrations[16]. In general, one can categorize a round jet nozzle type through a flat surface as a sharp-edged orifice plate (OP), smooth contraction (SC), or a long pipe (LP). Among these three different nozzles, the most detailed research was performed on SC nozzles [131, 83]. It has been shown that SC jets have a nearly laminar flow profile at the jet exit with a uniform ‘top-hat’ velocity profile. LP nozzles [85, 86, 77], on the other hand, produce a nearly Gaussian velocity profile due to fully developed turbulent conditions at the pipe exit. These jets also have thicker initial shear layers compared to the SC jets. Sharp-edged OP jets have received more recent attention, in the last decade, where detailed measurements [74, 89] have revealed that this configuration has the highest mixing rates downstream from the release nozzle.

In addition to round jets, several investigations [75, 88, 40, 135] have examined jet releases through different shaped orifices of varying aspect ratios, also through flat plates. Results from these investigations have shown that asymmetric behaviours emerge, such as the *axis-switching* phenomenon. Such behaviour, and other related mechanisms, lead to increased mixing, turbulence intensity, and entrainment rates compared to round jets. In other investigations, buoyancy effects on vertical jets [111] have been investigated, while others [94, 13] have extended the survey of all available experimental data for both turbulent buoyant/pure jets and plumes to provide a quantitative study into the buoyancy effects. According to theory [35], jets and plumes both have different states of partial or local self-similarity. However, the global evolution of jets and plumes have a tendency to evolve towards complete self-similarity through a universal route, in the far-field, even with presence of buoyancy. It has also been concluded that large-scale structures of turbulence drives the evolution of the self-similarity profile, and buoyancy has an effect in exciting these coherent structures [13].

The influence of initial conditions on turbulent mixing and combustion performance in reactive jets, has also been of active interest in the scientific community [41, 81, 98]. In last two decades, due to rapid growth in the use of hydrogen powered fuel cell vehicle, several experimental and numerical studies [29, 54, 53, 45] have also addressed different accidental hydrogen dispersion scenarios in enclosed and open spaces, while others [17, 52, 96, 97, 132] investigated laboratory small-scale unintended hydrogen round jet release in ambient air. It is noteworthy that all aforementioned studies, as well as related previous investigations on jets or plumes, have been limited to leaks through flat surfaces, where the direction of the jet mean flow was aligned with the flow origin. All of this work has been of prime importance to determine the dispersive nature of gases, for fuel-safety purposes, for gas leaks of various hole geometries and inflow conditions. In reality, however, accidental fuel leaks would not be limited to flows through flat surfaces. From a practical point of view, flow patterns and dispersion of gas originating from holes in the side walls of circular pipes should also receive attention. To date, and to the our knowledge, no such investigation has been formally published.

In the current investigation, jets issuing from such realistic geometry were considered experimentally and numerically. Turbulent vertical jets, flowing through a 2mm diameter round hole in the side of a 6.36mm diameter round tube, were studied. The investigation thus considered flow through a curved surface from a source whose original velocity components were nearly perpendicular to the direction of the ensuing jets. From now on, we refer to this jet configuration as a 3D jet. This orientation permitted practical flow velocity and concentration field measurements for a realistic scenario, which were compared to axisymmetric leaks through flat surfaces accordingly. Particle imaging velocimetry (PIV) and acetone-seeded planar laser-induced fluorescence (PLIF) were used to measure high-resolution instantaneous velocity and concentration fields, respectively, through experiment. To compliment the experiments, large eddy simulation (LES) was also employed to model the gas dispersion. An efficient Godunov solver was used, and coupled with adaptive mesh refinement (AMR) to provide high-resolution solutions only in areas of interest. The fluids considered experimentally and numerically were air and helium. Hydrogen was also considered for the numerical investigation. The different fluid densities, ratio of specific heats, and buoyancy were considered accordingly. The outer-scale flow Reynolds numbers, based on the orifice diameter, and Mach numbers of the jets ranged from 18,000 to 56,000 and 0.4 to 1. The purpose was to identify and characterize departures from standard axisymmetric jet conditions, and to highlight the asymmetric nature of the 3D jets, which ensued from a practical geometry arrangement. To further compare the 3D jets with axisymmetric jets, measurements were also carried out for the same physical jet conditions, and hole diameter, through a sharp-edged orifice plate (OP) type flat surface jet. The results obtained suggest that discrepancies exist, when applying conventional assumptions for round jets issuing through flat surfaces, to determine statistical properties associated with gas leaks from pipelines.

3.3 Methodology

3.3.1 Experimental system and techniques

Flow facility

Figure 3.1a, provides a schematic overview of the experimental setup used for this study. The experiments were conducted within a controlled stagnant environment, at room temperature and pressure ($\hat{T}_o \sim 22°$, $\hat{p}_o \sim 100$ kPa) , where the hat, '$\hat{}$', refers to a dimensional quantity. Dry filtered air was supplied by a central flow facility, while pure scientific grade helium was supplied through compressed T-cylinders. Flow controllers (Bronkhorst, EL-FLOW series) were used to control mass flow rates to the system, with a high accuracy (standard $\pm 0.5\%$ of reading plus $\pm 0.1\%$ full scale) and precision (within 0.2% of the reading). For each experiment the test gas was passed through the PIV seeder (LaVision Aerosol Generator) at a constant pressure

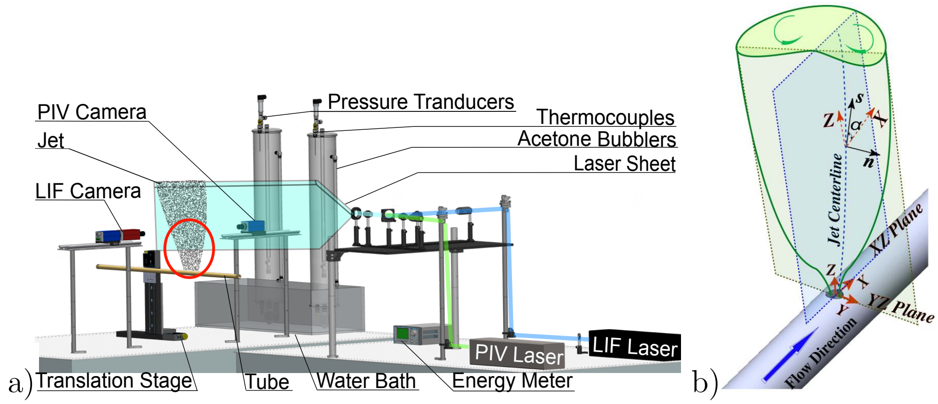

Figure 3.1: a) Schematic of the experimental layout. b) Illustration of 3D jet flow measurement area (red inset in part a).

to ensure a consistent amount of tracer particles in all tests. Di-Ethyl-Hexyl-Sebacate (DEHS) tracer particles were used, with a typical diameter of less than 1 μm. The test gas was also passed through two ‘bubbler’-type seeders. These seeders contained liquid acetone to be used as fluorescent tracers for the PLIF. A water bath was used to control the acetone temperature to allow acetone vapours to mix with the test gas isothermally to a saturated state. In all experiments, the test gas was consistently mixed with $\sim$ 1% acetone vapour by mass fraction. All mixing procedures were also controlled by mass flow controllers. The mixing was monitored by pressure transducers and thermocouples at several locations within the system. Isothermal and isobaric conditions were thus ensured in all experiments. After the test gas was mixed and seeded with the PIV and PLIF tracers, the flow entered the test section of the tube. The test-section tube used in this study had an outer diameter of 6.36mm, with a wall thickness of 0.82mm and length of 460mm. This size piping was appropriately selected owing to its representative size and arrangement of what might be found in compact hydrogen fuel cell applications. The orifice, through which the gas dispersed, had a diameter of $\hat{D} = 2$mm and was located sufficiently downstream to ensure fully developed flow within the pipe at the orifice location. Depending on the flow and geometric conditions under which gas leaks occur, the resulting jets can undergo several flow regimes from supersonic to subsonic[87]. In this study we considered subsonic flow conditions with fully developed turbulent flow inside the tube. The flow rates considered were sufficient to provide required amount of tracer particles for both PIV and PLIF measurements to study wide range of Reynolds numbers.

Figure 3.1b illustrates the jet flow evolution from the tube orifice. To capture the three-dimensionality of the jet, measurements were obtained on two different planes (denoted x-z and y-z) for each experiment, as indicated. Also shown in the figure is the jet centreline, which acts as a reference from which measurements are later obtained in the x-z plane. Owing to potential deviation of the jet from the orifice axis (z-axis), the jet centreline tangent and normal lines are shown as s and n coordinates in the figure, respectively.

In order to compare the evolution of the different test gases, the averaged momentum flux, $\hat{M}$, at the jet exit was measured and matched for all test cases, as suggested in previous studies [15, 83]. This matching was achieved, iteratively, by varying the volumetric flow rate ($\hat{Q}$) in the system. Here, $\hat{M}$ was calculated by first obtaining the time-averaged jet exit velocity from two-dimensional PIV measurements, which was measured at the closest vertical distance, $z \simeq 0$, to the orifice. The two-dimensional momentum flux, in units of [N/m], was then calculated from

$$\hat{M} = \int_{-\hat{D}/2}^{\hat{D}/2} \hat{\rho}_j \langle \hat{u}(\hat{r}) \rangle^2 d\hat{r} \tag{3.1}$$

where the subscript 'j' refers to the conditions at the nozzle, the angle brackets '$\langle\ \rangle$' refers to a time-averaged quantity, and the hat '$\hat{}$' refers to a dimensional quantity. Here $\hat{D} = 2$ mm was the diameter of the orifice. ρ and r refer to density and radius, respectively. Table 3.1 shows the flow properties used in this study, for both the 3D and OP jet configurations. The flows were characterized by the outer-scale Reynolds number, $Re_\delta = \langle \hat{u}_j \rangle \delta / \hat{\nu}_\infty$. Here, $\hat{\nu}_\infty$ is the ambient fluid kinematic viscosity and δ is the width of the mean axial velocity profile, evaluated from limits of 5% of the centreline velocity at $z \simeq 0$.

Table 3.1: Flow properties

Jet	$\hat{Q}$ [L/min]	$\langle \hat{u}_j \rangle$ [m/s]	$\hat{\rho}_j$ [Kg/m^3]	$\hat{\nu}_j$ [m^2/s]	$\hat{M}$ [N/m]	Fr	Re_δ
3D Air	15	147.5	1.17	1.54×10^{-5}	50.9	-	19,000
OP Air	15	127.6	1.17	1.54×10^{-5}	38.1	-	16,500
3D He	35	399.7	0.165	1.21×10^{-4}	51.4	1144	51,500
OP He	35	341.9	0.165	1.21×10^{-4}	38.3	978	44,200

Velocity measurements

For the PIV measurements, a dual-head Nd: YAG pulsed laser (New Wave's SOLO III 15 HZ) was used to provide a light source at a wavelength of 532 nm to illuminate a two-dimensional cross-section of the flow. The optical system was designed to create a light sheet with an approximate height of 5 cm and thickness of 1 mm. The PIV CCD camera was equipped with a Nikon Micro-NIKKOR 60 mm lens, and the lens aperture was kept at (f4). To suppress background light, a 532 nm bandpass filter with the full width at half maximum (FWHM) of 10 nm was attached to the camera lens. The field of view of the camera was a 40×30 mm^2 window with an approximate pixel size of 6.5 μm in physical space. Following the procedure of Su [110], we estimate this resolution to be comparable to the finest scales of the flow, with respect to the Nyquist criterion. To retain spatial resolution, the full measurement region is covered by three individual imaging windows with at least 20% overlap between each window. The time interval dt between the laser pulses in each pair of image was interactively adjusted in order to optimize the accuracy of the calculated particle displacement. The instantaneous particle location images were obtained at a frequency of 10 Hz and each pair of images was processed using LaVision DaVis 8.4 software to calculate the instantaneous velocity fields. The corresponding velocity fields were thus compiled at a temporal frequency of 5 Hz. This process was followed by applying a multi-pass spatial resolution improvement algorithm. With each pass, the interrogation window size, corresponding to a single calculated velocity vector field, was decreased from 32×32 to 16×16 pixels, with a 75% overlap between the windows in the horizontal and vertical directions. As a result, each instantaneous velocity field contains approximately 288100 vectors. For each experiment case, a total of N = 500 velocity field images were acquired for statistical averaging. Following the PIV uncertainty propagation method[99], we estimated conservative uncertainty values of 3% and 6% in the time-averaged velocity and Reynolds shear stress profiles, respectively.

Concentration measurements

To measure the concentration of the jet gas in the flow field, we applied PLIF. In this study, acetone was chosen as the tracer. A Pulsed Nd: YAG laser (Spectra-Physics INDI-40-10-HG) was used to provide a stable 266 nm wavelength ultraviolet light in order to excite the acetone molecules. In order to obtain a linear fluorescence regime, optical lenses were used to create a light sheet with an approximate height of 5 cm and a thickness of 350 μm. This ensured that saturation of the fluorescence signal did not occur until laser energy per pulse reached $\sim$ 10.4 J, which was well above the maximum laser energy output (55 mJ) used in this study.

The PLIF CCD camera was equipped with an intensifier unit, which was sensitive to the ultraviolet spectrum, in order to increase gain and gating capability. The camera was also equipped with a Nikon Micro-NIKKOR 105 mm lens. The aperture was kept open at (f2.8), and a 378-nm UV bandpass filter with FWHM of 140 nm was used. The camera field of view for all cases corresponded to a 38$\times$28 mm^2 window with an approximate pixel size of 6.5 μm. To retain the spatial resolution of the scalar field, the full measurement region is covered by three individual imaging windows with at least a 20% overlap between each window. Before and after each experiment, sets of background and laser sheet images were taken to determine the averaged background and cross-sectional laser beam intensity distributions. These time-averaged images were later subtracted from each raw PLIF image in order to isolate the fluorescence signal. In order to account for the laser beam energy fluctuations, all images were normalized by the amount of the laser energy per pulse, which was measured using a laser energy meter. The images were taken at a frequency of 5 Hz and then processed using LaVision DaVis 8.4 software. With correcting the errors associated with background noises, fluctuations in cross-sectional laser beam intensity, and laser energy per pulse deviations, one can assume the remaining non-uniformity of the scalar field is due to signal to noise ratio (S/N). The error in the S/N can be estimated from the standard deviation of this ratio in an uniform low signal region of the flow field. Based on these data, and uncertainty propagation method, we estimated the uncertainty in the time-averaged and variances of concentration field to be conservative values of 4% and 7%, respectively. . For each experimental case, a total of $N = 500$ images were acquired to determine the time-averaged molar concentration, $\langle C \rangle$, fields. Figure 3.2 shows examples of the instantaneous velocity and concentration fields, for the helium 3D jet in the x-z plane. It should be noted that the flow fields were constructed from three different experiments, where individual imaging windows have been stitched together.

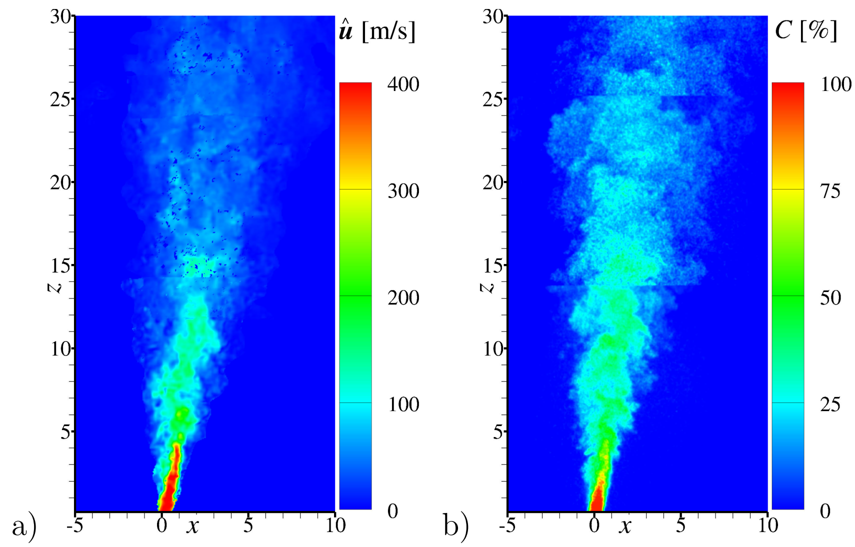

Figure 3.2: Instantaneous a) velocity and b) concentration fields obtained from Helium
3D jet in x-z plane from three individual imaging windows and stitched together.

3.3.2 Numerical techniques

Governing equations

For flows which are turbulent and compressible, the gas dynamic evolution is governed by the compressible Navier-Stokes equations. In order to account for the full spectrum of turbulent scales, resulting from large flow velocities with high Reynolds numbers (Re), the unresolved scales of the governing equations are filtered and modelled through the large eddy simulation (LES) approach [80]. The LES-filtered conservation equations for mass, momentum, and energy (sensible + kinetic) of a calorically perfect fluid system are given below in Eqs. (3.2)-(3.4), respectively. Also, a transport equation (3.5) is included to describe the evolution of mass fraction (Y) associated with the jet gas. The governing equations are supplemented by a one-equation localized kinetic energy model [14], given by Eq. (3.6), which describes the transport, production, and dissipation of the subgrid kinetic energy (k^{sgs}) associated with subgrid velocity fluctuations. Finally, the equations of state are given by (3.7). The equations presented here are given in non-dimensional form, where the various properties are normalized by the reference quiescent state. Favre-average filtering is achieved by letting $\tilde{f} = \overline{\rho f}/\bar{\rho}$, where f represents one of the state variables and ρ, p, e, T, and $\boldsymbol{u}$ refer to the density, pressure, specific sensible + kinetic energy, temperature, and velocity vector, respectively. Here, the over-line ($^{-}$) refers to a spatially-averaged (filtered) quantity, and the tilde (˜) refers to a mass-averaged (Favre-averaged) quantity. Other relevant properties are the ratio of specific heats, γ, the kinematic viscosity, ν, the resolved shear stress tensor, $\bar{\bar{\boldsymbol{\tau}}}$, the Prandtl number, Pr, and the Schmidt number, Sc. Also, subgrid contributions due to buoyancy have been accounted for, where $\boldsymbol{g}$ is the gravitational acceleration.

$$\frac{\partial\bar{\rho}}{\partial t} + \boldsymbol{\nabla}\cdot(\bar{\rho}\tilde{\boldsymbol{u}}) = 0 \tag{3.2}$$

$$\frac{\partial(\bar{\rho}\tilde{\boldsymbol{u}})}{\partial t} + \boldsymbol{\nabla}\cdot(\bar{\rho}\tilde{\boldsymbol{u}}\tilde{\boldsymbol{u}}) + \nabla\bar{p} - \boldsymbol{\nabla}\cdot\bar{\rho}(\nu+\nu_t)\left(\nabla\tilde{\boldsymbol{u}} + (\nabla\tilde{\boldsymbol{u}})^T - \frac{2}{3}(\boldsymbol{\nabla}\cdot\tilde{\boldsymbol{u}})\boldsymbol{I}\right) = \bar{\rho}\boldsymbol{g} \tag{3.3}$$

$$\frac{\partial(\bar{\rho}\tilde{e})}{\partial t} + \boldsymbol{\nabla}\cdot\left((\bar{\rho}\tilde{e}+\bar{p})\tilde{\boldsymbol{u}} - \tilde{\boldsymbol{u}}\cdot\bar{\bar{\boldsymbol{\tau}}}\right) - \boldsymbol{\nabla}\cdot\left(\bar{\rho}\left(\frac{\gamma}{\gamma-1}\right)\left(\frac{\nu}{Pr}+\frac{\nu_t}{Pr_t}\right)\nabla\tilde{T}\right) = \bar{\rho}\tilde{\boldsymbol{u}}\cdot\boldsymbol{g} \tag{3.4}$$

$$\frac{(\partial\bar{\rho}\tilde{Y})}{\partial t} + \boldsymbol{\nabla}\cdot(\bar{\rho}\tilde{\boldsymbol{u}}\tilde{Y}) - \boldsymbol{\nabla}\cdot\left(\bar{\rho}\left(\frac{\nu}{Sc}+\frac{\nu_t}{Sc_t}\right)\nabla\tilde{Y}\right) = 0 \tag{3.5}$$

$$\frac{\partial(\bar{\rho}k^{sgs})}{\partial t} + \boldsymbol{\nabla}\cdot(\bar{\rho}\tilde{\boldsymbol{u}}k^{sgs}) - \boldsymbol{\nabla}\cdot\left(\frac{\bar{\rho}\nu_t}{Pr_t}\nabla k^{sgs}\right) = -\frac{\nu_t}{Pr_t}\nabla\bar{\rho}\cdot\boldsymbol{g} + \dot{P} - \bar{\rho}\epsilon \tag{3.6}$$

$$\tilde{e} = \frac{\bar{p}/\bar{\rho}}{(\gamma-1)} + \frac{1}{2}\tilde{\boldsymbol{u}}\cdot\tilde{\boldsymbol{u}} + k^{sgs} \qquad \text{and} \qquad \frac{\bar{p}}{\bar{\rho}} = R\tilde{T} \tag{3.7}$$

The various state variables have been normalized such that

$$\rho = \frac{\hat{\rho}}{\hat{\rho}_o},\ \boldsymbol{u} = \frac{\hat{\boldsymbol{u}}}{\hat{\boldsymbol{c}}_o},\ p = \frac{\hat{p}}{\hat{\rho}_o\hat{\boldsymbol{c}}_o{}^2} = \frac{\hat{p}}{\gamma\hat{p}_o},\ T = \frac{\hat{T}}{\gamma\hat{T}_o},\ x = \frac{\hat{x}}{\hat{D}},\ t = \frac{\hat{t}}{\hat{D}/\hat{\boldsymbol{c}}_o},\ R = \frac{\hat{R}}{\hat{R}_o} = \frac{1/\hat{\overline{W}}}{1/\hat{W}_o}, \tag{3.8}$$

where the subscript 'o' refers to the reference state, the hat ('ˆ') refers to a dimensional quantity, $\boldsymbol{I}$ is the identity matrix, $\boldsymbol{c}$ is the speed of sound, W is the molecular weight, and D is the reference diameter of the orifice through which the gas exits the pipe.

The rates of production and dissipation of k^{sgs} are given by

$$\dot{P} = \bar{\rho}\nu_t\left(\nabla\tilde{\boldsymbol{u}} + (\nabla\tilde{\boldsymbol{u}})^T - \frac{2}{3}(\boldsymbol{\nabla}\cdot\tilde{\boldsymbol{u}})\boldsymbol{I}\right)\cdot(\nabla\tilde{\boldsymbol{u}}) \quad \text{and} \quad \epsilon = \pi\left(\frac{2k^{sgs}}{3C_\kappa}\right)^{3/2}/\bar{\Delta}. \tag{3.9}$$

Next, a Smagorinsky-type model is applied to describe ν_t in terms of k^{sgs} through

$$\nu_t = \frac{1}{\pi}\left(\frac{2}{3C_\kappa}\right)^{3/2}\sqrt{k^{sgs}}\bar{\Delta}. \tag{3.10}$$

Here, C_κ is the *Kolmogorov constant*, whose value is set to a typical value of $C_\kappa = 1.5$. For simplicity, the LES filter size, $\bar{\Delta}$, is assumed to be equal to the (local) minimum grid spacing. It is noted, however, that this assumption may introduce some errors at fine-coarse cell interfaces when using adaptive mesh refinement (AMR) [122]. Finally, for the helium case, owing to differences in γ, Eq. (3.5) is replaced with

$$\frac{(\partial\bar{\rho}\tilde{G})}{\partial t} + \boldsymbol{\nabla}\cdot(\bar{\rho}\tilde{\boldsymbol{u}}\tilde{G}) - \boldsymbol{\nabla}\cdot\left(\bar{\rho}\left(\frac{\nu}{Sc} + \frac{\nu_t}{Sc_t}\right)\nabla\tilde{G}\right) = 0 \tag{3.11}$$

where

$$\tilde{Y} = \frac{\tilde{G} - G_{\text{air}}}{G_{\text{He}} - G_{\text{air}}} \quad \text{and} \quad G = \left(\frac{1}{\gamma - 1}\right). \tag{3.12}$$

Although the conservative form used in this method is known to introduce pressure oscillations, which originate from material interfaces [103], it is necessary to ensure the correct mathematical representation of the diffusion process. While non-conservative approaches do not exhibit such pressure oscillations [103], they can also converge to physically incorrect solutions with respect to diffusion [51]. For practical purposes, γ is evaluated from $\tilde{G}$ directly, as no suitable alternative exists in the LES framework.

Domain and model parameters

The numerical domain containing the pipe and jet configuration is shown in Fig. 3.3. The pipe had an outer diameter of $3.18D$ (6.36mm) with a wall thickness of $0.41D$ (0.82mm). The hole, through which gas escaped, had a diameter of $\hat{D} = 2$mm. The domain itself spanned $32D$ in each direction. The inlet boundary condition (BC) was imposed on one side of the pipe, which used a digital filtering generation method [61] to generate the appropriate second order turbulence characteristics according to welldocumented experimental measurements of turbulence in pipe flow [28]. A wall BC was imposed on the other side of the pipe, which causes the flow to stagnate within the pipe. This was consistent with the experiments. The top BC of the domain was a pressure outlet type. The remaining 5 BCs were symmetry type slip walls, and were sufficiently far away from the jet to prevent interference. The simulations were initialized with air at ambient conditions ($\hat{T}_o = 300$K and $\hat{p}_o = 101.3$kPa) throughout the domain.

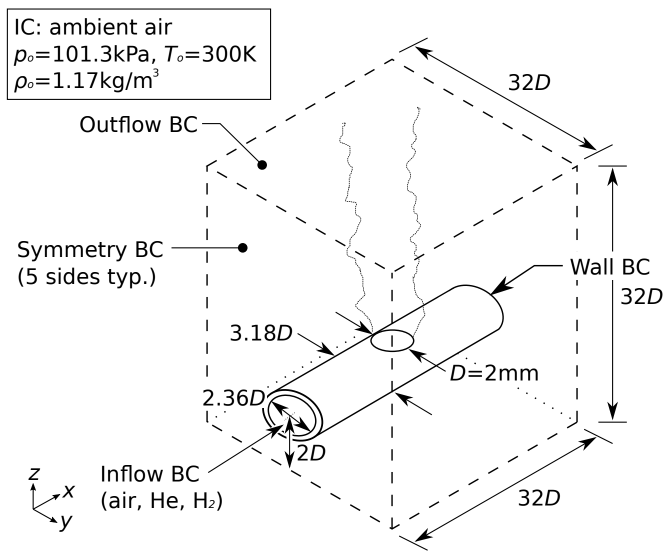

Figure 3.3: Computational domain with initial and boundary conditions (not to scale).

To be consistent with the experiments, the average momentum flux, $\langle\bar{\rho}\tilde{\boldsymbol{u}}\rangle_{\text{flux}}$, was matched for all simulations. To achieve this, the inlet pressure was varied, through trial and error, to obtain the desired $\langle\bar{\rho}\tilde{\boldsymbol{u}}\rangle_{\text{flux}}$ and average flow velocity, $\langle\tilde{\boldsymbol{u}}_j\rangle$. Since three-dimensional information was available, the instantaneous $(\rho u)_{\text{flux}}$ was monitored directly on the x-y plane corresponding to the hole location on the outer edge of the pipe, at $z = 0$. In this case,

$$M = (\rho u)_{\text{flux}} = \int_{z=0} \rho u_z u_z dA. \tag{3.13}$$

The resulting time-averaged $\langle\bar{\rho}\tilde{\boldsymbol{u}}\rangle_{\text{flux}}$, jet velocity, $\langle\tilde{\boldsymbol{u}}_j\rangle$, and other relevant fluid properties are given in Table 3.2. The transport properties have been evaluated at equimolar conditions of ambient air and the jet gas, and were assumed constant for simplicity.

For the turbulent transport properties of all three jets, $Sc_t = 0.7$ and $Pr_t = 0.8$ were also assumed constant. Finally, for each jet, a total of $N = 500$ (for air) or $N = 1500$ (for H_e/H_2) time steps were processed for statistical averaging, once a quasi-steady jet was established. This corresponded to sampling over eddy turnover times of $\tau = 450$, 1800, and 2040 for air, helium, and hydrogen, respectively.

Table 3.2: Model Parameters.

Jet	$\bar{\bar{\rho}}_j$ [kg/m^3]	$\langle\tilde{\hat{\boldsymbol{u}}}_j\rangle$ [m/s]	Ma	Re	$\langle\bar{\hat{\rho}}\tilde{\hat{\boldsymbol{u}}}\rangle_{\text{flux}}$ [N]	γ	$\hat{\nu}$ [m^2/s]	Pr	Sc
air	1.17	141.7	0.4	17,824	0.0335	1.4	1.59×10^{-5}	0.714	0.707
He	0.164	368.1	1.1	38,545	0.0317	1.67	1.91×10^{-5}	0.607	0.626
H_2	0.082	528.4	1.5	55,915	0.0328	1.4	1.89×10^{-5}	0.556	0.609

Numerical implementation

In order to solve the system of equations (3.2) through (3.6), a numerical framework (MG) developed by Mantis Numerics Ltd. [31, 32, 33] was employed. All of the terms in the equation set were handled individually using an operator splitting technique [65]. Each term in the equation set was solved explicitly, in time, using a second order accurate finite-volume discretization scheme. In this method, solutions of the system

$$\frac{\partial \boldsymbol{U}}{\partial t} + \frac{\partial \boldsymbol{F}}{\partial x_i} + \frac{\partial \boldsymbol{G}}{\partial x_i} + \boldsymbol{S} = 0 \tag{3.14}$$

are sought, where $\boldsymbol{U} = [\bar{\rho}, \bar{\rho}\tilde{\boldsymbol{u}}, \bar{\rho}\tilde{e}, \bar{\rho}\tilde{Y}(\text{or } \bar{\rho}\tilde{G}), \bar{\rho}k^{sgs}]$ is the solution vector and Einstein notation was adopted for the directional components. $\boldsymbol{F}$ and $\boldsymbol{G}$ are the advective and diffusive fluxes, respectively, and $\boldsymbol{S}$ represents the source terms. First, solution contributions of the advection terms are discretized using the MacCormack predictor-corrector method [65], where

$$\boldsymbol{U}_i^* = \boldsymbol{U}_i^n - \frac{\Delta t}{\Delta x_i}\left[\boldsymbol{F}_{i+1/2}^n - \boldsymbol{F}_{i-1/2}^n\right] \tag{3.15}$$

and

$$\boldsymbol{U}_i^{n+1} = \boldsymbol{U}_i^n - \frac{1}{2}\frac{\Delta t}{\Delta x_i}\left[\boldsymbol{F}_{i+1/2}^n - \boldsymbol{F}_{i-1/2}^n + \boldsymbol{F}_{i+1/2}^* - \boldsymbol{F}_{i-1/2}^*\right]. \tag{3.16}$$

Here, the flux terms $\boldsymbol{F}_{i\pm1/2}^*$ are evaluated using the predicted state, $\boldsymbol{U}_i^*$, in order to obtain the solution for $\boldsymbol{U}_i^{n+1}$. The time step for each simulation below is chosen according to the CFL stability criterion of 0.5 [65]. To obtain the advective flux components at each cell interface ($\boldsymbol{F}_{i\pm1/2}$), an *exact* Godunov solver [37] was applied, which featured a symmetric monotonized central flux limiter [121]. In this scheme, exact solutions to the Reimann problem [65] at each cell interface provide the fluxes necessary for the finite-volume solution, where differences in γ potentially exist on each side of the cell interfaces. Likewise, diffusive flux contributions are also added to the solution using the MacCormack predictor-corrector method. However, the flux components of $\boldsymbol{G}$ are further discretized using central finite-differences [116]. Finally, source term contributions of $\boldsymbol{S}$ are added to the solutions directly.

Structured Cartesian grids were applied in order to take advantage of AMR [32] for increased efficiency. The grid was refined, on a per cell-basis, in regions close to the physical pipe, and also where the jet gas mass ($\bar{\rho}\tilde{Y}$) changed by more than 0.01% locally between existing grid levels. Furthermore, when a cell is flagged as 'bad', or needing refinement, this badness is diffused by approximately 5-10 cells in each direction on the current grid level. The jet was refined to a minimum grid size of $D/16$ up to $10D$ downstream from the orifice in order to capture fine scale turbulent motions in the near field. Beyond $10D$ downstream, the jet was only refined to a minimum grid size of $D/8$. Finally, once a cell was refined, it remained refined for the duration of the simulation. This approach avoided complications which could arise due to cell-derefinement and re-refinement [79]. Figure 3.4 shows a typical grid topology that develops as a jet evolves in time. The figure also indicates the locations of each grid level (G) in a portion the flow field.

Resolution study

A resolution study was performed for air jet simulations at three different spatial resolutions. The minimum grid sizes were varied from $\bar{\Delta} = D/4$ to $\bar{\Delta} = D/16$. Corresponding instantaneous evolutions of the jet gas mass fraction ($\tilde{Y}$) are presented in Fig. 3.5a for each resolution. It was found that the lowest resolution, $\bar{\Delta} = D/4$, was not able to resolve any turbulent motions downstream from the orifice, and hence there was minimal jet spreading observed. As the resolution was increased to $\bar{\Delta} = D/8$, turbulent motions were captured in the far field, which lead to significantly more jet spreading, and unsteadiness, as expected. When the minimum grid size was set to $\bar{\Delta} = D/16$, small-scale turbulent motions were captured closer to the orifice,

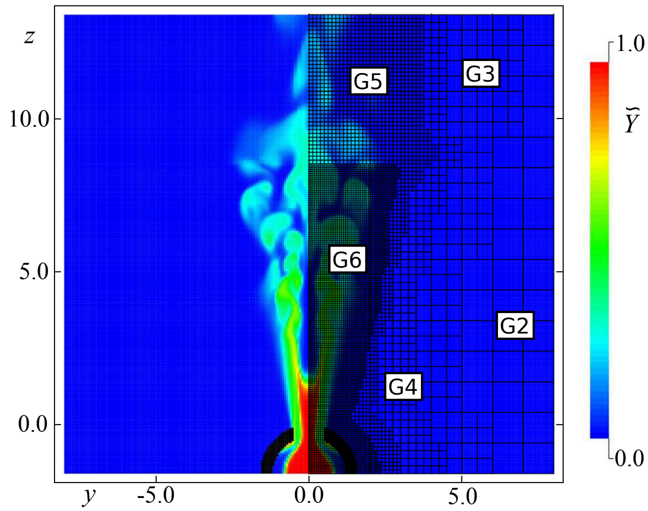

Figure 3.4: Instantaneous air jet showing the mass fraction $\tilde{Y}$ on the left and resulting grid topology, showing the locations of various grid levels (G2-G6), on the right. Note: The base grid G1 is always refined to at least grid level G2, everywhere.

which caused a shortening of the potential jet core region owing to increased turbulent mixing.

Figures 3.5b and c show the jet trajectories and velocity decay rates for all three cases. It should be noted that the subscript 'c' refers to the conditions at the jet centreline. In order to measure the trajectory of each jet, whose deflection from the vertical (z) axis was observed previously in Fig.3.2 , the (x, y) locations of the maximum velocity ($\langle \tilde{\boldsymbol{u}} \rangle_{\max}(z)$) magnitude were determined at discrete heights along the z-axis. Also shown are the computed centre of mass locations (C.M.) for each simulation. The C.M., as a function of height (z), was determined by extracting x-y slices at each discrete heights along the z-axis, and evaluating the centroid associated with the average mass flux of the jet through each slice. For a given z location,

$$x_{\text{C.M.}} = \frac{\int \overline{(\rho u_z Y)} x dx dy}{\int \overline{(\rho u_z Y)} dx dy} \quad \text{and} \quad y_{\text{C.M.}} = \frac{\int \overline{(\rho u_z Y)} y dx dy}{\int \overline{(\rho u_z Y)} dx dy} \tag{3.17}$$

The velocity decay rates, along the jet centre-lines, have been determined from $\langle \tilde{\boldsymbol{u}} \rangle_{\max}(z)$. In general, increasing the resolution lead to increased deflection about the z-axis, in both $\langle \tilde{\boldsymbol{u}} \rangle_{\max}(z)$ and the C.M., as observed in Fig, 3.5b. It should also be noted that the discrete jumps in the $\langle \tilde{\boldsymbol{u}} \rangle_{\max}(z)$ locations were equal to the grid spacing associated with the corresponding resolution. Such discreteness was not observed for the C.M. locations since the averaging process was performed across entire $x - y$

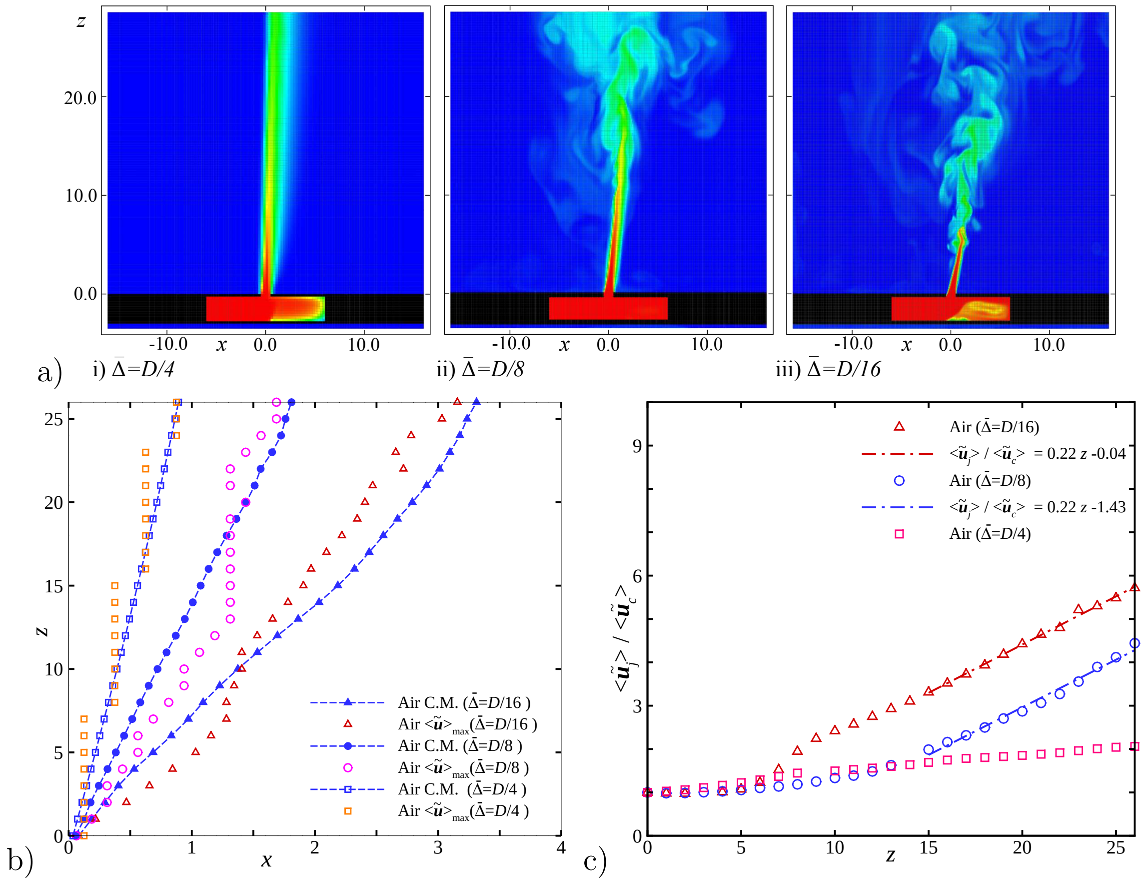

Figure 3.5: a) Instantaneous mass fraction field ($\tilde{Y}$) for air at different resolutions. b) Jet centre-lines taken along the location of maximum velocity ($\langle \tilde{\boldsymbol{u}} \rangle_{\max}(z)$), and also the centre of mass (C.M.) locations, obtained for air at different resolutions. c) Jet velocity decay rates for air simulations at different resolutions. It should be noted that the subscript 'c' and 'j' refers to the conditions at the jet centreline and the nozzle, respectively.

planes. This resulted in smoother trajectories for the computed C.M. locations. In Fig. 3.5c, increasing the resolution lead to an earlier decay in centreline velocity. This behaviour in the jet velocity decay resulted from higher resolution of fine scale turbulent motions near the orifice, which influenced earlier breakup of the potential core, thus slowing the motion of the jet. It should be noted, however, that the actual rate of velocity decay, in the far field, was found to be the same for both the $\bar{\Delta} = D/8$ and $\bar{\Delta} = D/16$ resolutions. These far field velocity decay rates were determined by the slopes of lines of best fit beyond $z > 15D$, obtained from linear regression, as shown in Fig. 3.5c.

For the high resolution cases ($\bar{\Delta} = D/16$), solutions were obtained on approximately 10 to 20 million computational cells and each took three to four weeks to compute on 64 processors. In addition, each simulation took several weeks to post-process owing to large volumes of data and available computational resources. Higher resolution simulations were unattainable beyond $\bar{\Delta} = D/16$, owing to a significant increase in the required computational resources, simulation time, and processing time, by roughly an order of magnitude.

3.4 Results

3.4.1 Time-averaged flow fields

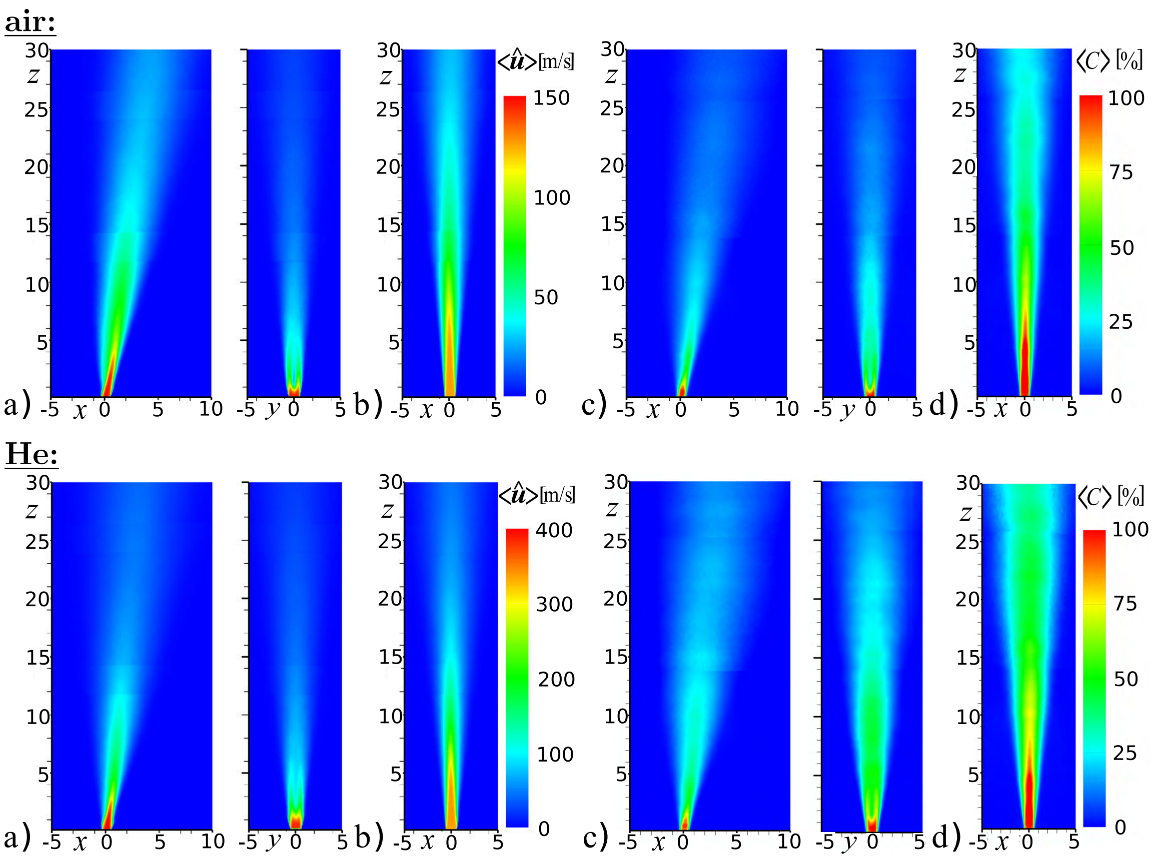

Figure 3.6: Time-averaged velocity (a - b) and concentration (c - d) contours in x-z and y-z planes for 1) air and 2) helium, obtained from: a & c) Round jet on side of tube (3D jet), and (b & d) Round orifice plate (OP) jet.

The time-averaged velocity contours, obtained for all of the experiments, are shown in Fig. 3.6. These contours are shown in both the x-z and y-z planes for the 3D jet experiments, and only in the x-z plane for the OP jets. Clearly, for the 3D jets in the x-z planes, there was a slight deviation from the vertical z-axis in the direction of the initial flow inside the pipe for both gases. In this plane, significant jet spreading was observed as soon as the jets flowed through the orifice. This behaviour was much more pronounced in the case of the 3D jet compared to the OP jet. Also, for the 3D jets, near the potential-core region, there was more jet spreading on the upstream of the jet (left side) compared to the downstream side. There was also a shorter potential-core length observed for helium compared to air. These potential core lengths, in the x-z planes, were approximately $4D$ and $5D$ for helium and air, respectively. The potential-core lengths of both 3D jet gases were also shorter compared to the axisymmetric OP jets. The respective core lengths of the OP jets for helium and air were $7D$ and $9D$. In the x-z planes, for the 3D jet, the jet spreading appeared to be greater, in the far field, compared to the y-z plane. There were also two high-velocity peaks observed in y-z plane, for both gases, at $y \pm 0.5D$, on each side of the z-axis, with a low-velocity region located on the axis at approximately $z = 2D$. These features were not observed in the OP jet. Also, the potential-core lengths in this plane were much shorter compared to the x-z plane. In the y-z plane, the potential-core length for both gases was approximately $1D$. In general, it was observed that the helium and air jets had qualitatively similar flow patterns, for each case. However, the helium jet, in both experiments, appeared to break up faster compared to the air jet.

Figure 3.6 also shows the time-averaged concentration fields obtained for all experiments. In general, the concentration profiles were qualitatively similar to the velocity profiles presented in Fig. 3.6, with two exceptions. First, much higher concentration levels, with higher spreading rates, were observed for helium in the far field compared to air, for all cases. Also, for the 3D jets, the potential core lengths in the x-z plane, for both gases, were comparable to the potential core lengths in the y-z plane.

Although not shown here, numerically computed flow fields were also obtained for each gas. It is noted that the fundamental asymmetry was also observed for each numerical experiment.

3.4.2 The jet centreline trajectory

Figure 3.7 shows the experimental and numerical jet trajectories for the 3D jets. For the experiments, the trajectories were determined by the maximum velocity magni-

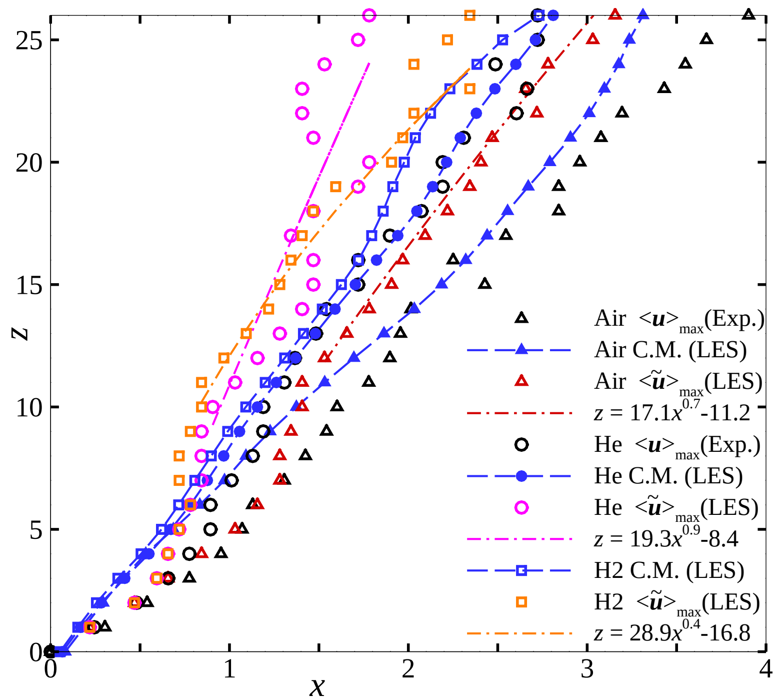

Figure 3.7: Jet centre-lines taken along the location of maximum velocity magnitudes ($\langle \boldsymbol{u} \rangle_{\max}(z)$ and $\langle \tilde{\boldsymbol{u}} \rangle_{\max}(z)$) from experiments and simulations, respectively, and also the centre of mass (C.M.) locations obtained from the simulations.

tude locations ($\langle \boldsymbol{u} \rangle_{\max}(z)$), in the x-z plane. The numerical simulations present both the trajectories determined from ($\langle \tilde{\boldsymbol{u}} \rangle_{\max}(z)$) and the centre of mass (C.M.).

In general, the centrelines obtained from the experiments followed a nearly linear trajectory from the orifice up to $z \sim 4D$ for helium, and $z \sim 5D$ for air. From these point, the centrelines deviated upwards, slightly. Around $z \sim 9D$ for helium, and $z \sim 10D$ for air, a sudden change in the jet trajectory was observed. These locations coincided with the extents of the potential-core regions as shown in Fig. 3.6. Also, helium was found to deviate from the z-axis less than air, owing to increased buoyancy forces, in the z-direction, which arise due to the lower jet gas density. From the simulations, it was clear that the jet centres, determined from $\langle \tilde{\boldsymbol{u}} \rangle_{\max}(z)$, matched well the experimental observations in the near field. However, in the far field, the simulated locations do not match those obtained from the experiments for helium and air beyond $z > 5D$ and $z > 7D$, respectively. Despite this, however, it was found that the C.M. locations matched very well the jet centre-lines obtained from the experiments in the far field, beyond these locations, for both helium and air. Clearly, the simulations exhibited a departure of the $\langle \tilde{\boldsymbol{u}} \rangle_{\max}(z)$ location from the actual jet centroid through the entire jet height for all three gases. Also, the $\langle\tilde{\boldsymbol{u}}\rangle_{\max}(z)$ locations for the helium simulation were found to contain significant scatter in the far field beyond $z > 15D$. The air and hydrogen simulations, on the other hand, were found to have a fairly continuous trajectory determined from the $\langle\tilde{\boldsymbol{u}}\rangle_{\max}(z)$ locations. As a reference, lines of best-fit, using linear regression to power-law expressions, were obtained for the far field (beyond $z > 10D$) for the centrelines determined from $\langle\tilde{\boldsymbol{u}}\rangle_{\max}(z)$. Even though helium deflected more than hydrogen, in terms of the C.M. locations, the opposite trend was observed when considering the $\langle\tilde{\boldsymbol{u}}\rangle_{\max}(z)$ locations.

3.4.3 Velocity decay and jet spreading rates

In Fig. 3.8a, the velocity decay along the jet centrelines, determined from $\langle\boldsymbol{u}\rangle_{\max}(z)$ and $\langle\tilde{\boldsymbol{u}}\rangle_{\max}(z)$, are presented for all experimental and numerical cases, respectively. Also shown, for comparison, are velocity decay correlations [130], which have been determined from prior compressible subsonic and supersonic axisymmetric round jet experiments, for the range jet conditions that encompass the current investigation. Upon comparison to the Witze correlations [130], the air and helium OP jet experiments were found to reproduce well the expected velocity decay rate, with helium decaying faster than the air jet. In general, the decay rates observed in the experimental 3D jets were much faster compared to the axisymmetric jets. Upon comparison of the experimental 3D jet velocity decays to simulation, it was found that the simulated air jet velocity decay rate matched closely that obtained from experiment. For the helium jet, however, the simulation had a much faster decay rate compared to experiment. Despite this, both exhibit the same trend, where helium was found to decay faster than air. It was also observed that the experiments had a shorter potential-core region compared to simulation. In general, the simulated onsets of velocity decay, downstream from the orifice, were found to occur approximately $2D$ beyond those observed from the experiments. Finally, from simulation, hydrogen jet was found to decay the quickest, owing to its low density and high flow velocity.

Figure 3.8b shows the jet widths ($2L_{1/2}$) that have been obtained by determining the locations where $\langle\boldsymbol{u}\rangle = 0.5\langle\boldsymbol{u}\rangle_{\max}(z)$ and $\langle\tilde{\boldsymbol{u}}\rangle = 0.5\langle\tilde{\boldsymbol{u}}\rangle_{\max}(z)$ along lines which were orthogonal to the jet-centrelines, from experiments and simulations, respectively. These orthogonal lines have been indicated previously as coordinate n in Fig. 3.1b. In the y-z planes, the orthogonal lines to the jet-centres are collinear with the y-direction owing to symmetry of the jet. Also, jet widths along the y-direction from

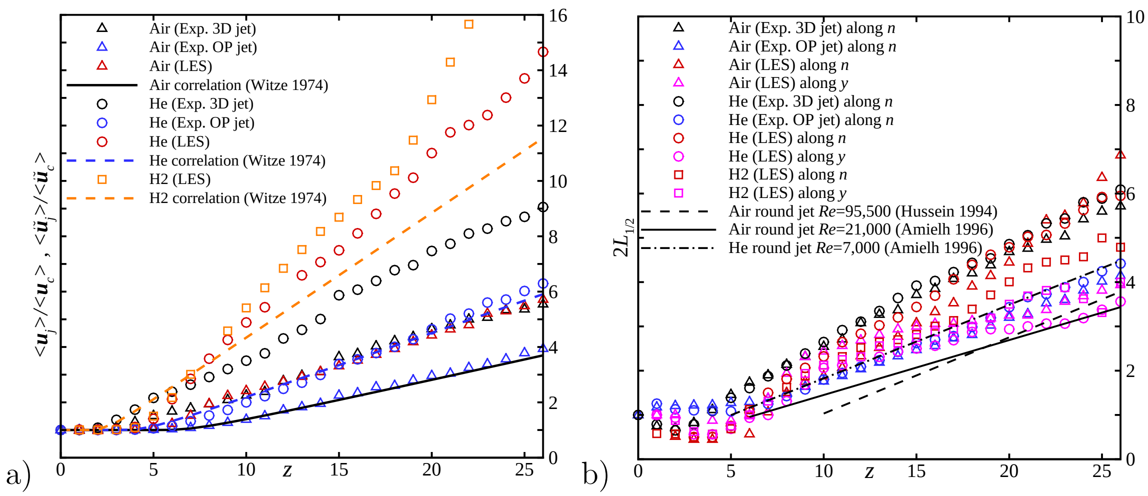

Figure 3.8: a) Jet velocity decay and b) jet widths ($2L_{1/2}$) obtained along the $\langle \boldsymbol{u} \rangle_{\max}(z)$ and $\langle \tilde{\boldsymbol{u}} \rangle_{\max}(z)$ centrelines, from experiments and simulations, respectively. Note, the n-coordinate refers to lines which are normal to the centreline, coplanar with the x-z plane (see the coordinate system in Fig.3.1 b). Also, velocity decays and jet widths have been compared to axisymmetric round jet correlations [130] and experiments [56, 2], respectively.

the jet centreline were only available from simulation owing to the three-dimensional deflection of the jet centre in the x-direction. In general, the OP jets were found to have nearly constant jet widths in the potential core region, up until $z \sim 5D$. From this point on, the jet width was found to increase linearly, consistent with the jet spreading rates of previous axisymmetric round jet experiments (for a wide range of Re) [56, 2]. For the 3D jets, in all cases, a slight contraction in the jet widths has been observed from $1D < z < 4D$ experimentally, and from $1D < z < 7D$ numerically. Beyond this point, the jet spreading rates in the x-z plane, along n, were observed to be much greater compared to the axisymmetic jets for all cases. Moreover, the air and helium jet spreading, from the 3D experiments and also the simulations, was found to be comparable for both gases. In the near field, however, significant jet spreading did not occur until about $z \sim 7D$ to 8 for the simulations, while spreading was found to occur at $z \sim 5D$ for the 3D experiments. These values coincide with the potential-core extents of the jets. In the y-z plane, along y, the jet spreading obtained from the simulations deviated from those obtained in the x-z plane for $z > 12D$. In fact, it was found that the jet spreading of air and helium in the y-direction, found numerically, compared well to the jet spreading of axisymmetric round jets, in terms of order of magnitude, while more jet spreading was found in the x-z plane. Finally, unlike air and helium, the simulated hydrogen 3D jet was found to spread almost equally in both directions. There was only slightly higher amount of jet spreading in the n-direction compared to the y-direction.

3.4.4 Jet centreline statistics

In the x-z plane, the time-averaged velocity profiles for all experimental and numerical investigations are shown in Fig. 3.9 along the n-direction for several downstream locations along the jet centreline (s-curve Fig. 3.1b). Likewise, the velocity profiles are also shown along the y-direction. It is noted, however, that information along y, normal to s, was only available from the numerical simulation. Also shown, for comparison, are the velocity statistics obtained for the OP jet experiments. In particular, only the s-component velocities have been presented, which were normalized by the local centreline velocity magnitudes ($\langle \boldsymbol{u} \rangle_{\max}(z)$ and $\langle \tilde{\boldsymbol{u}} \rangle_{\max}(z)$) for all experiments and simulations, respectively. Also, the n- and y-coordinates, which were both normal to the centreline s-curve, were normalized by the jet half widths ($L_{1/2}$) determined from Fig.3.8b. In all cases, the experimental and numerical 3D jets emerged from the orifice with a top-hat profile, shown at $z = 1D$. This was different compared to the OP jet, which had an initial semi saddle-back profile (not shown here), typical for axisymmetric sharp-edged OP jets [74]. In general, all cases of the experimental and numerical 3D jets developed into a self-similar Gaussian-like distribution within the range $|n/L_{1/2}| < 1$ for $z \leq 5D$ (and $|y/L_{1/2}| < 1$ for $z \leq 5$). In fact, the distribution observed for the 3D jets, in this range, matched well the self-similar Gaussian distribution obtained from the OP jets. However, notable deviations from the self-similar solution were observed near the tail ends of the curves in the x-z plane, beyond this range . The experiments were found to exhibit more velocity spreading to the left of the jet centre (in the $-n$-direction). On the other hand, the simulations were found to exhibit more velocity spreading to the right of the jet centre (in the $+n$-direction). Beyond $z > 5D$, in the far field, the experimental 3D jets developed into, and matched, the self-similar Gaussian distribution obtained from the OP jets for the full range of n (and y). The numerical simulations, however, continued to exhibit velocity spreading to the right of the jet centre (in the $+n$-direction). Finally, the curves obtained for all three gases were found to be in agreement with each other.

Higher order statistics were also collected for the experiments and simulations conducted here. The time-averaged Reynolds stress profiles obtained from experi-

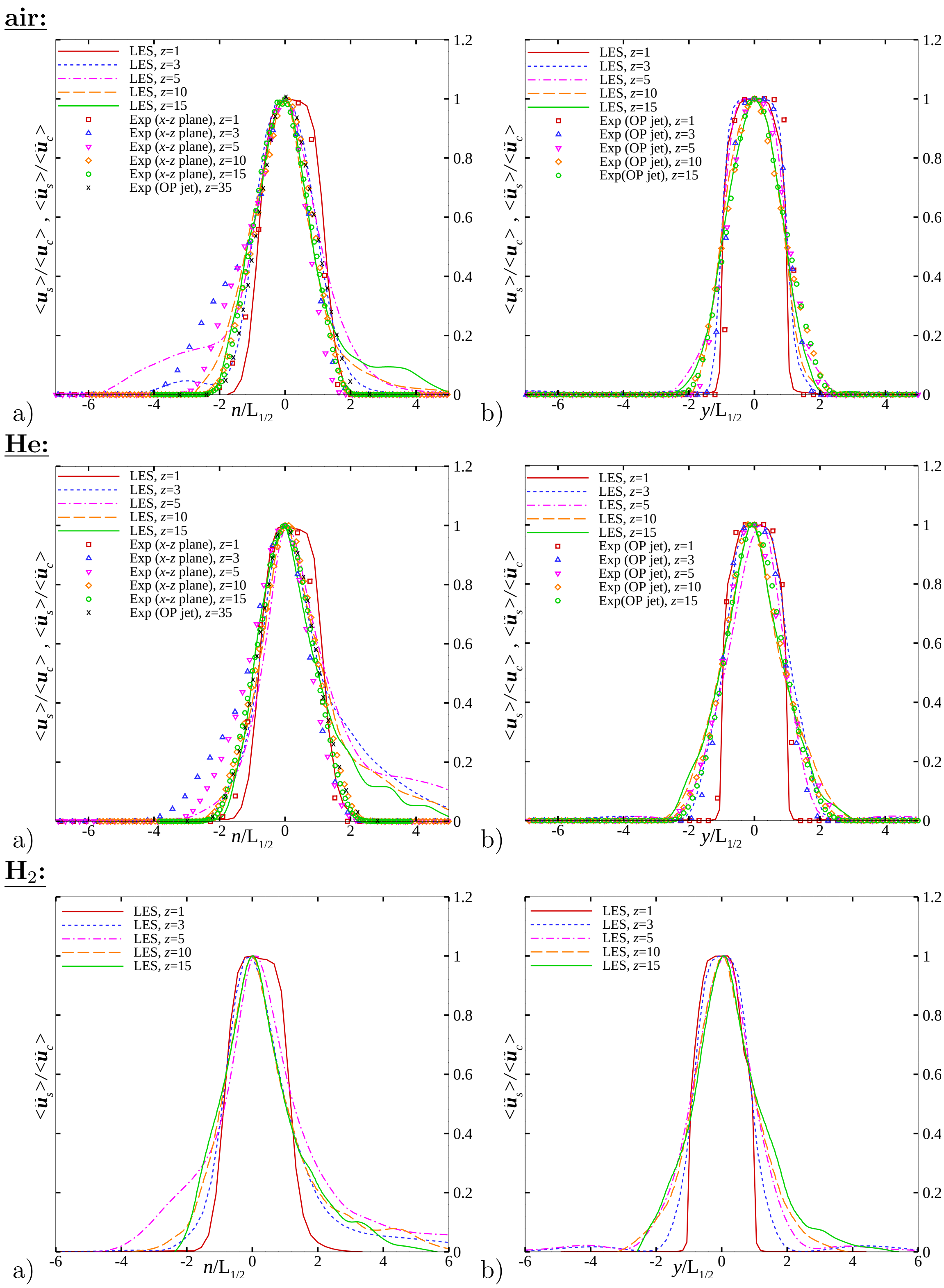

Figure 3.9: Normalized time-averaged velocity profiles along jet centrelines ($\langle \boldsymbol{u}_s \rangle / \langle \boldsymbol{u}_c \rangle$ and $\langle \tilde{\boldsymbol{u}}_s \rangle / \langle \tilde{\boldsymbol{u}}_c \rangle$) for experiments and simulations, respectively. Here, the profiles are taken at various heights for air, helium, and hydrogen, and obtained from a) LES, OP & 3D jet in x-z plane and b) LES & OP jet in y-z planes.

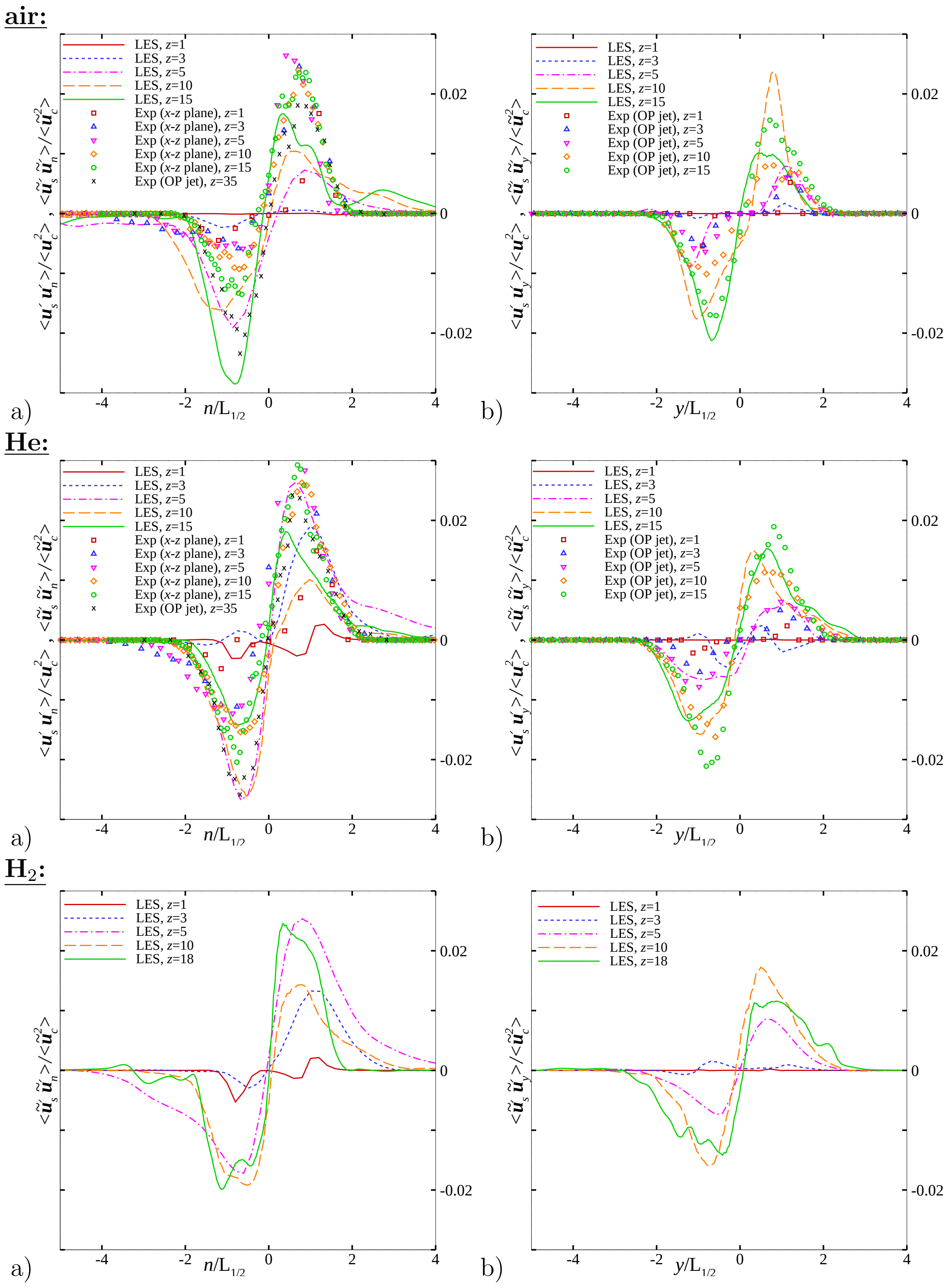

Figure 3.10: Normalized time-averaged Reynolds shear stress profiles along jet centrelines ($\langle \boldsymbol{u}_s' \boldsymbol{u}_n' \rangle / \langle \boldsymbol{u}_c^2 \rangle$, $\langle \boldsymbol{u}_s' \boldsymbol{u}_y' \rangle / \langle \boldsymbol{u}_c^2 \rangle$) and ($\langle \tilde{\boldsymbol{u}}_s' \tilde{\boldsymbol{u}}_n' \rangle / \langle \tilde{\boldsymbol{u}}_c^2 \rangle$, $\langle \tilde{\boldsymbol{u}}_s' \tilde{\boldsymbol{u}}_y' \rangle / \langle \tilde{\boldsymbol{u}}_c^2 \rangle$) for experiments and simulations, respectively. Here, the profiles are taken at various heights for air, helium, and hydrogen, and obtained from a) LES, OP & 3D jet in x-z plane and b) LES & OP jet in y-z planes.

ments and simulation, ($\langle \boldsymbol{u}'_s \boldsymbol{u}'_n \rangle$, $\langle \boldsymbol{u}'_s \boldsymbol{u}'_y \rangle$) and ($\langle \tilde{\boldsymbol{u}}'_s \tilde{\boldsymbol{u}}'_n \rangle$, $\langle \tilde{\boldsymbol{u}}'_s \tilde{\boldsymbol{u}}'_y \rangle$), are presented in Fig. 3.10. In this case, the experimental and numerical Reynolds stress quantities have been normalized by ($\langle \boldsymbol{u}_c^2 \rangle(z)$) and ($\langle \tilde{\boldsymbol{u}}_c^2 \rangle(z)$), respectively. Also, it should be noted that the prime ($'$) represents the instantaneous fluctuating quantity. For example, $\boldsymbol{u}' = \boldsymbol{u} - \langle \boldsymbol{u} \rangle$ or $\tilde{\boldsymbol{u}}' = \tilde{\boldsymbol{u}} - \langle \tilde{\boldsymbol{u}} \rangle$. In the x-z plane, the air and helium experiments captured well the far field self-similar profile to the right of the jet centre (in the $+n$-direction). However, to the left (in the $-n$-direction), the 3D jet experiments were found to have a lower magnitude of the Reynolds stress compared to the OP jets, even in the far field. Also, within for $z \leq 5D$, a higher Reynolds stress was observed beyond $|n/L_{1/2}| < 1$. In the y-z plane, the 3D jet experiments matched well the Reynolds stress profiles obtained from the OP jets. In general, the simulations for air and helium captured the correct shapes of the Reynolds stress profiles, but did not capture the peak values observed experimentally, in both planes. This effect can be attributed to the fact that the Reynolds stress was determined from $\langle \tilde{\boldsymbol{u}}'_s \tilde{\boldsymbol{u}}'_n \rangle$ and $\langle \tilde{\boldsymbol{u}}'_s \tilde{\boldsymbol{u}}'_y \rangle$, which did not account for the subgrid contribution from k_{sgs}. For 3D jet experiments, it should also be noted that there is an offset of the zero crossing of Reynolds stress profiles form jet centreline ($n/L_{1/2} = 0$). This brings into question the suitability of conventional eddy-viscosity models for this type of turbulent flow, as this class of turbulence models assumes Reynolds stresses are directly related to the mean strain.

The time-averaged concentration profiles for all experimental and numerical cases are shown in Fig. 3.11. Here, time-averaged molar concentrations from experiments and simulations ($\langle C \rangle$ and $\langle \tilde{C} \rangle$), have been normalized by the local centreline concentrations $\langle C_c \rangle(z)$ and $\langle \tilde{C}_c \rangle(z)$, respectively. The n- and y-coordinates were normalized by the jet half widths ($L_{c,1/2}$) determined from the locations where $\langle C \rangle / \langle C_c \rangle = 0.5$ and $\langle \tilde{C} \rangle / \langle \tilde{C}_c \rangle = 0.5$ for all experimental and numerical cases, respectively. In general, they were found to be qualitatively similar to the velocity profiles in all cases. In the near field ($z \leq 5D$), the range $|n/L_{c,1/2}| < 1$ for $z \leq 5D$ (and $|y/L_{c,1/2}| < 1$ for $z \leq 5D$) was found to develop quickly into the self-similar solution as observed from the OP jet experiments. Notable deviations from the self-similar solution were once again observed near the tail ends of the curves in the x-z plane, beyond this range. In the x-$z$plane, the experiments were found to exhibit more concentration spreading to the left of the jet centre (in the $-n$-direction), while the simulations were found to exhibit more concentration spreading to the right (in the $+n$-direction). In the far field, beyond $z > 5D$, the self-similar Gaussian distribution, as observed for the OP

air:

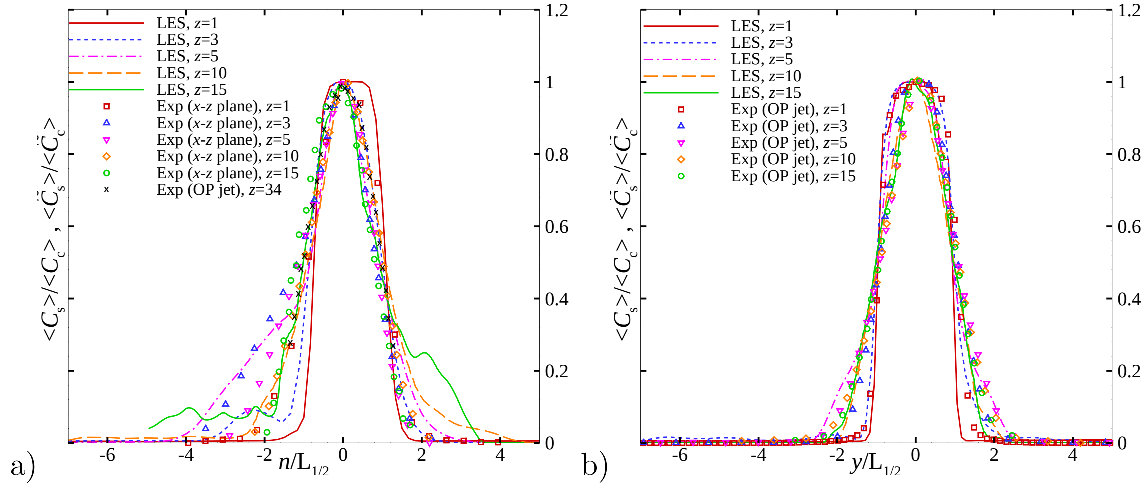

He:

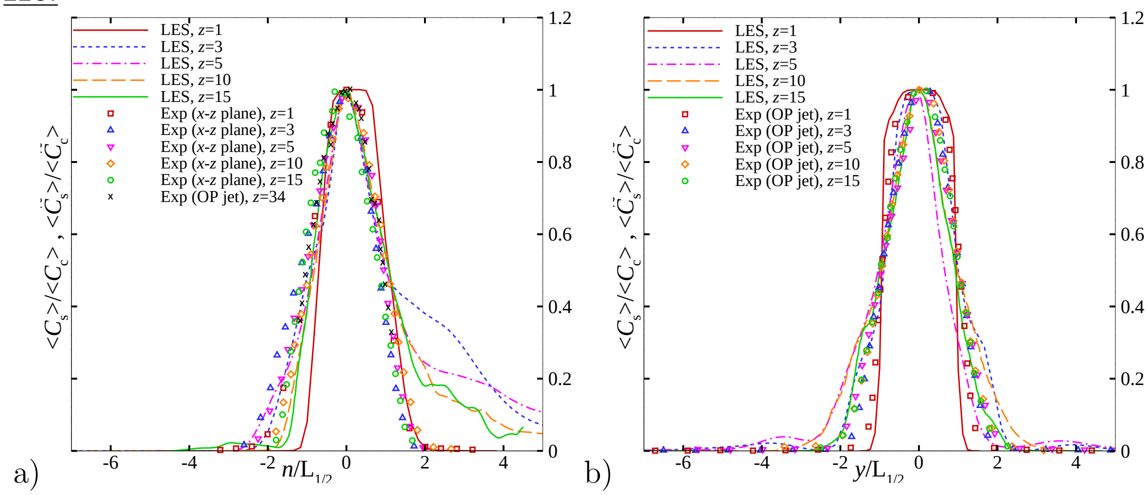

H_2:

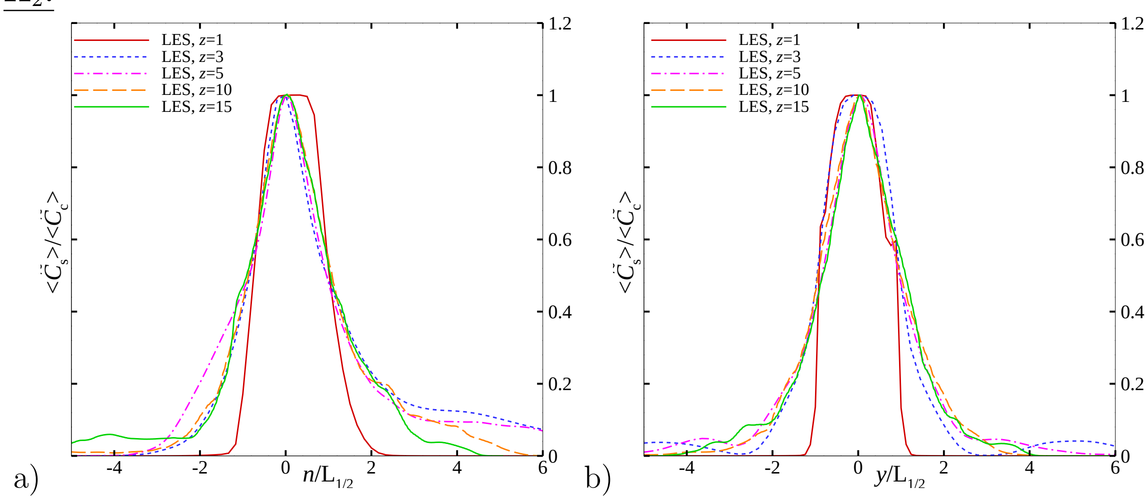

Figure 3.11: Normalized time-averaged concentration profiles along jet centrelines ($\langle C_s\rangle/\langle C_c\rangle$ and $\langle\tilde{C}_s\rangle/\langle\tilde{C}_c\rangle$) for experiments and simulations, respectively. Here, the profiles are taken at various heights for air, helium, and hydrogen, and obtained from a) LES, OP & 3D jet in x-z plane and b) LES & OP jet in y-z planes.

jet experiments, was recovered for both the 3D jet experiments. As observed in the velocity profiles, the simulations continued to exhibit concentration spreading in the $+n$-direction of the far field.

Finally, the normalized concentration variance profiles ($\langle C_s'^2 \rangle / \langle C_c^2 \rangle(z)$ and $\langle \tilde{C}_s'^2 \rangle / \langle \tilde{C}_c^2 \rangle(z)$), obtained from both the 3D and OP jet experiments and the simulations for all three gases, respectively, are presented in Fig. 3.12. In the x-z plane, the initial development of the 3D jets had a higher variance of concentration to the right of the jet centre (in the $+n$-direction) within the ranges of $z \leq 10D$ and $z \leq 5D$, for the air and helium, respectively. Beyond these jet heights, in the far field, the location of maximum concentration variance moved to the left of the jet centre (in the $-n$-direction) for both air and helium 3D jet experiments. Also, much like the OP jet evolutions, the 3D jet experiments were found to contain a minimum variance near the centre of the jet. In general, the magnitudes of concentration variance were comparable between the 3D jet and OP experiments for both gases. In the y-z plane, the OP jet experiments exhibit symmetrical profile for the concentration variances as expected from axisymmetric round jets. In general, the simulations captured the correct shapes of the second-order concentration fluctuation profiles, but did not capture the peak values observed experimentally in the far field, in both planes. In fact, the simulations were found to have an error of 50% in the variance compared to experiments at $z = 15D$. We note, however, that only filtered quantities of jet mass fraction ($\tilde{Y}$) are available numerically. Also, it is likely that much longer sampling times are required in the far field owing to the presence of much larger and slower eddies.

3.5 Discussion

3.5.1 Asymmetry of the jet

For the 3D jets, asymmetric flow structure was always observed. It was found that the perpendicular nature of the orifice, relative to the direction of flow within the pipe, caused a deflection of the jet away from the vertical z-axis. It is not yet clear how the deflection angles scale for each gas. However, air was found to deflect more than helium (and hydrogen), despite having equal initial momentum flux (force) ejecting through the orifice. Initially, from Fig. 3.7, all three gases have very close deflection angles. After only $z > 2D$, was the experimental air jet found to deflect more than helium. Upon considering the simulated trajectories, obtained from the C.M. loca-

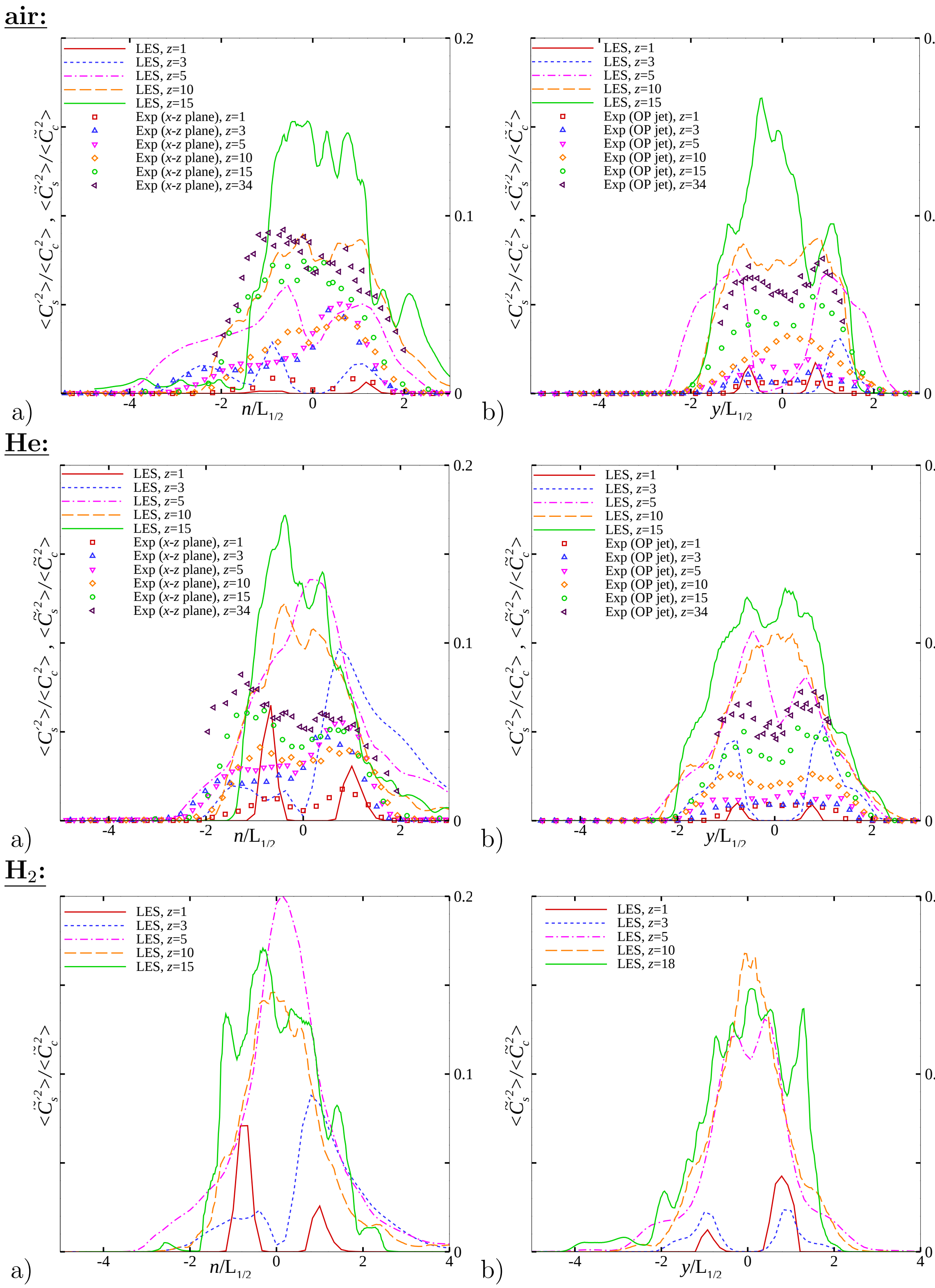

Figure 3.12: Normalized concentration variance profiles along jet centrelines ($\langle C_s'^2\rangle/\langle C_c^2\rangle$ and $\langle \tilde{C}_s'^2\rangle/\langle \tilde{C}_c^2\rangle$) for experiments and simulations, respectively. Here, the profiles are taken at various heights for air, helium, and hydrogen, and obtained from a) LES, OP & 3D jet in x-z plane and b) LES & OP jet in y-z planes.

tions, it was found that the heavier gases deflected more about the z-axis compared to lighter gases, with hydrogen having the least amount of deflection. Although other factors might contribute, the higher deflection of the air jet compared to the less dense helium and hydrogen jets is consistent with the relative strength of the corresponding vertical buoyancy forces.

From the numerical simulations, in Fig. 3.7, one notable 'event' was always observed to occur for each gas, in the near field, between $z = 5D$ to $10D$. Not only does this location correspond to the extent of the potential-core, in each case, but the $\langle \tilde{\boldsymbol{u}} \rangle_{\max}$ location was found to switch sides relative to the C.M. Up until $z \sim 9D$ for air, and $z \sim 6D$ for helium and hydrogen, the $\langle \tilde{\boldsymbol{u}} \rangle_{\max}(z)$ were located to the right of the C.M. At this point, however, the locations of $|\overline{\boldsymbol{u}}|_{\max}$ remained almost constant in x until $z \sim 11D$ for all three gases. Downstream, the trajectories of $\langle \tilde{\boldsymbol{u}} \rangle_{\max}$ deflected to the right again, but remained misaligned to the left of the C.M.

In order to gain insight into the reasons for shifts of the location of $\langle \tilde{\boldsymbol{u}} \rangle_{\max}(z)$ with respect to the C.M., average velocity contours were extracted from the simulations on x-y planes at various heights, along z, for all three gases. Figure 3.13 shows these velocity contours for the hydrogen simulation, although it is noted that the other gases were qualitatively similar through their evolution. At the very start of the jet evolution, shown at $z = 0$, the initial jet was not circular. In fact, a velocity deficit existed near the left-most portion of the orifice, and also in two regions on the right side, near $x = 0.25D$ and $y \pm 0.3D$. The velocity deficit on the upstream of the jet likely resulted from flow separation of the moving gas originating from inside the pipe, akin to flow over a backward step [124] or cavity [36]. This phenomena was also observed in the 3D jet experiments and visualized in Fig. 3.13 with instantaneous velocity streamlines obtained from the helium experiment. It is also likely that this flow separation encouraged entrainment of air on the back side of the jet (in the $+x$-direction) which lead to the enhanced mixing observed in this region. For the other two flow deficit regions, near near $x = 0.25D$ and $y \pm 0.3D$, these were likely caused by the curvature of the pipe diameter relative to the hole size; further investigation is required to ascertain this.

Owing to the flow separation at the entrance to the orifice, and resulting velocity deficit near the edge of the orifice, a nearly stagnant region was formed downstream at $z = 3D$ in Fig. 3.13 and centred at $x = y = 0$. Also, there existed regions of significant flow velocity magnitudes on both sides of the stagnant region in the $\pm y$ directions. This explains why the C.M. of the jet was initially misaligned with the $\langle \tilde{\boldsymbol{u}} \rangle_{\max}(z)$

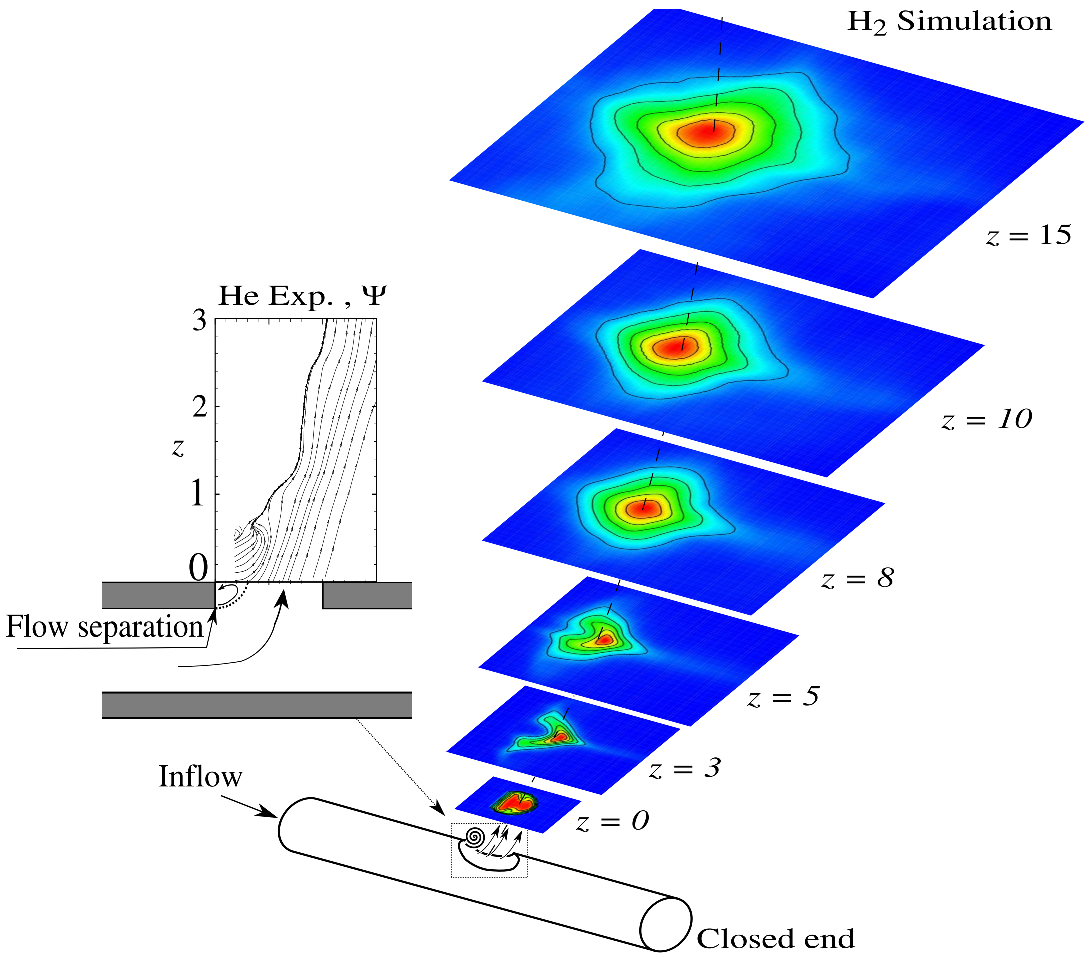

Figure 3.13: Time-averaged velocity contours in x-y planes for the simulated H_2 jet. Also shown are instantaneous velocity streamlines (Ψ) obtained for the helium 3D jet, near the orifice.

location. This flow pattern also explains the saddle-back feature observed in the velocity profiles of the experimental 3D jets, in the y-z planes of Fig.3.6. The well-known Vena Contracta effect, generated immediately downstream from the orifice, may have also contributed to this saddle-back profile due to inward radial velocities at the edge of the jet[76]. Eventually, at $z = 5D$, the stagnant region became entrained by the jet as mixing occurred , leading to its disappearance downstream.

By $z = 8D$, although significant mixing and jet spreading had occurred by this point, a portion of the simulated jets remained asymmetric. In fact, the overall shape of the simulated jets were stretched in the $+x$ direction, relative to the jet centre. From $x > 3D$, there appeared to exist minor secondary jetting along the $+x$ direction, which was not observed in any other directions. This secondary jetting was believed to contribute to the far field misalignment of the $\langle \tilde{\boldsymbol{u}} \rangle_{\max}(z)$ location with the C.M. However, this secondary jetting was not observed in the experiments, likely due to fine-scale mixing near the orifice, which was not captured in the simulations. Thus, it is very likely that the true C.M. of the jet is infact aligned with the $\langle \tilde{\boldsymbol{u}} \rangle_{\max}(z)$ location in the far field.

At $z = 15D$, the shapes of the simulated helium and air jets had become elliptical (not shown). Significant jet spreading was observed in the $+x$ direction compared to all other directions, which is consistent with the increased jet spreading along the n direction relative to the y direction, as observed in Fig. 3.8b. The hydrogen simulation, on the other hand, was found to develop into a fairly round jet by $z = 15D$, as shown. Although the location of $\langle \tilde{\boldsymbol{u}} \rangle_{\max}(z)$ was still slightly misaligned with the C.M., the spreading rates in all directions were nearly equal. Whether the air and helium jets eventually become axisymmetric, in the far field, remains to be investigated. The degree of asymmetric jet spreading observed for heavier gases, in the n and y directions, is consistent with buoyancy effects. It is very likely that increased horizontal deflection associated with lower buoyancy forces leads to more interaction of the jet with the pipe boundary, thus contributing to the observed asymmetry. It is also possible that the early symmetric development for hydrogen, compared to air and helium, may arise due to enhanced mixing associated with the supersonic nature of the jet in the former case.

3.5.2 Implications of jet asymmetry on ignition limits

In the experimental concentration fields presented in Fig.3.6, helium was found to have much higher concentration levels in the far field compared to air, at $z > 3D$. This observation can be attributed to a low Schmidt number ($Sc < 1$), in which case mass diffusion rates are faster than momentum diffusion rates. On the other hand, axisymmetric OP jets exhibited even higher concentration levels, compared to 3D jets, in both near and far fields for both gases. This result is further supports the fact that significantly higher turbulent mixing and entertainment rates occur in the 3D jets compared to axisymmetry OP jets, thus shortening the extents of where the ignition limits might lie along the jet centreline in the far field, in the ($+s$-direction). This effect is also evident in the faster velocity decay rates, and shortened potential core regions, as observed previously in Fig. 3.8. While the 3D jets ultimately developed into self-similar concentration profiles, as observed in Fig. 3.11, such self-similarity cannot be used to predict the ignition limits in the near field. This implication is especially true for the back side of the jets (in the $-x$-direction), for $z < 5D$, where this enhanced mixing gave rise to higher concentration levels beyond $(n/L_{c,1/2}) < -1$. The turbulent mixing enhancement, and the fact that self-similarity solutions are unable to predict the ignition limits in the near field, are also evident in lower concentration variance magnitudes observed in Fig. 3.12 for the $z \leq 5D$ on the back side of the 3D jets, compared to the front side (in the $+x$-direction). Moreover, due to this unsteady nature of the jet, as observed from instantaneous concentration fields of Fig.3.2 and significant variance in concentration fluctuations of Fig.3.12, there exists the possibility of increased local gas concentration, above the flammability-limit, in regions beyond those predicted by the self-similar profiles of Fig. 3.11. A similar trend was previously shown to be the case for axisymmetric jets [17], where the probability of hydrogen ignition outside of conventional self-similar time-averaged limits was computed through simulation.

3.5.3 Departures of simulation from experiment

In this investigation, several discrepancies were observed between the simulations and experiments. First, the appearance of stagnant regions in the computed flow patterns at $z = 3D$ of Fig.3.13 were not so prevalent in the experiments. It was found that the experiments exhibited more substantial mixing, from the onset of release, compared to the simulations. This enhanced mixing had the effect of mitigating the numerically observed stagnant regions, and also shortened the potential core length compared to the simulations. It is well known that increases in turbulent mixing rates can reduce the potential core length of a jet [134]. Thus, it is probably the case that persisting laminar conditions exist in the potential core due to insufficient near field resolution in the simulations. Despite this short-coming, the simulations were found to capture the correct trends observed experimentally and have provided some insight, physically, in terms of the asymmetric nature of the jet, which emerged radially from the pipe.

In terms of the velocity decay, the simulation captured well the experimental measurements for air. However, a significant deviation from the experimental measurements was observed in the case of the helium simulation. It is unclear why this departure between experiment and simulation existed. It is possible that errors associated with mixing in the two-γ model generated a faster velocity decay for helium compared to the experimental case.

Finally, it has been observed that the location of $\langle \boldsymbol{u} \rangle_{\max}(z)$ was inconsistent between the simulations and the experiments. From the experiments, it was found that this location was relatively centred in the jet in the far field. In the simulations, however, the location of $\langle \tilde{\boldsymbol{u}} \rangle_{\max}(z)$ had a tendency to shift toward the left side of the jet C.M. location (in the $-x$ direction). Despite this, the numerical prediction of the C.M. was found to agree well with the $\langle \boldsymbol{u} \rangle_{\max}(z)$ location obtained from the experiments. It is possible that longer sampling periods are required in order to accurately predict the position of $\langle \tilde{\boldsymbol{u}} \rangle_{\max}(z)$ numerically.

3.6 Conclusions

In this study, experiments were conducted in order to investigate compressible turbulent jets, of varying gas densities and Reynolds numbers, issuing from realistic pipe geometry, and to compare them to axisymmetric round jets. A large-eddy-simulation strategy was also developed to provide further insight into the experimentally observed trends and the evolution of the flow patterns of the realistic 3D jets. The fluids considered were air and helium for the experiments, and the simulations provided further insight into the behaviour of hydrogen.

It was found that the flow within a pipe, perpendicular to an upward facing hole, caused the resulting jet outside the pipe to form at a deflection angle relative to the vertical axis, in the direction of the flow within the pipe itself. This deflection was influenced by the buoyancy of the jet, where heavier gases were found to deflect more than the lighter gases. Furthermore, flow separation inside the pipe, at the orifice, and curvature of the pipe, relative to the size of the hole, have contributed to the asymmetric flow patterns observed. In general, both air and helium experienced significantly more jet spreading compared to the axisymmetric jet experiments. Also, more jet spreading was observed on the upstream side of the asymmetric 3D jets compared to the axisymmetric case, in the near field. This enhanced mixing in the asymmetric case caused a reduction in the potential-core length, and an increase in the velocity decay rate. Also, in the far field, air and helium simulations were found to have substantially more jet spreading along the direction of the pipe, compared to all other directions. Hydrogen, however, was found to spread in a quasi-axisymmetric manner in the far field. Despite this, air and helium experiments were found to have significantly different patterns in the second-order concentration fluctuations compared to the OP jets. Should the development of concentration variance for hydrogen behave the same, ignition of hydrogen may also be influenced by such changes in variance due to the geometry considered. For these reasons, caution is required when using round jet assumptions to describe the correct dispersion, velocity decay, and ignition limits of a jet emitted from realistic geometries. To investigate this further, larger domains should be simulated, and larger flow fields should be captured experimentally, to capture the far-field evolution and to determine at what point higher-order self-similarity becomes valid. Also, higher resolution simulations of the near-field should be conducted to fully resolve fine-scale turbulent motions near the orifice. These recommendations, however, add considerable computational expense, which would constitute a longer term investigation.

Chapter 4

Measurements of Flow Velocity and Scalar Concentration in Turbulent Multi-component Jets: Asymmetry and Buoyancy Effects [1]

[1]The body of this chapter was submitted for publication in Majid Soleimani nia, Brian Maxwell, Peter Oshkai and Ned Djilali, Journal of Fluid Mechanics. MS designed the study and experimental system, conducted the measurements, performed the analysis, drafted the initial manuscript, and finalized the submitted version. BM, PO and ND contributed to the refinement of further manuscript drafts.

4.1 Preamble

Buoyancy effects and nozzle geometry can have a significant impact on turbulent jet dispersion. This work was motivated by applications involving hydrogen. Using helium as an experimental proxy, buoyant horizontal jets issuing from a round orifice on the side wall of a circular tube were analysed experimentally using particle image velocimetry (PIV) and planar laser-induced fluorescence (PLIF) techniques simultaneously to provide instantaneous and time-averaged flow fields of velocity and concentration. Effects of buoyancy and asymmetry on the resulting flow structure were studied over a range of Reynolds numbers and gas densities. Significant differences were found between the centreline trajectory, spreading rate, and velocity decay of conventional horizontal round axisymmetric jets issuing through flat plates and the pipeline leak-representative jets considered in the present study. The realistic pipeline jets were always asymmetric and found to deflect about the jet axis in the near field. In the far field, it was found that the realistic pipeline leak geometry causes buoyancy effects to dominate much sooner than expected compared to horizontal round jets issuing through flat plates.

4.2 Introduction

Hydrogen, a carbon-free energy carrier, is currently viewed as a clean alternative to traditional hydrocarbon-based fuels for transportation and energy storage applications. It can burn or react with almost no pollution or green house gas emissions, and is commonly used in electrochemical fuel cells to power vehicle and electrical devices. It is also used in an increasing number of power-to-gas systems to blend in the natural gas pipeline network. Despite these benefits, previous studies have shown that hydrogen jets resulting from an accidental leak are easily ignitable[123], owing to a wide range of possible ignition limits (between 4%-75% by volume) [66]. Therefore, modern safety standards for hydrogen storage infrastructure must be assured before widespread public use of hydrogen can become possible. As a result, fundamental insight into the physics of hydrogen dispersion into ambient air from realistic flow geometries, such as small pipelines, is necessary to properly predict flow structures and flammability envelope associated with hydrogen outflow from accidental leaks. Also, owing to the low molecular weight of hydrogen, buoyancy can significantly influence the development of the jet dispersion during a release scenario. In the current investigation, we attempt to quantify the dispersion and release trajectories of horizontal buoyant jets experimentally, as they emerge from a realistic pipeline geometry, using state-of-the-art experimental imaging techniques.

In the last two decades, due to the rapid development of the hydrogen economy and use of hydrogen technologies, several experimental and numerical studies [17, 52, 96, 97, 132] have investigated small-scale unintended hydrogen round jet release in ambient air, while others [29, 54, 53, 45] studied different accidental hydrogen dispersion scenarios in enclosed and open spaces. There has also been extensive work done to describe the evolution of axisymmetric round turbulent jets in terms of self-similarity correlations, obtained from statistical analysis from both experiments [67, 5] and simulations [71]. In addition, some investigations [111] have quantified the buoyancy effects on vertical round jets, while others [94, 13] have provided a quantitative study into the buoyancy effects on both turbulent buoyant/pure jets and plumes with analyzing of all available experimental data. Even though jets and plumes both have different states of partial or local self-similarity [35], their global evolutions in the far field tends toward complete self-similarity through a universal route even in the presence of buoyancy. Large-scale structures of turbulence drive the evolution of the self-similarity profile, and buoyancy has an effect in exciting the coherent turbulent structures; this effect is more evident in the evolution of plumes into self-similarly much sooner owing to buoyancy driven turbulence in the near field [13]. Horizontal buoyant jets, however, have been much less studied. In general, increasing effects of buoyancy were found to correlate inversely to the Froude number in axisymmetry horizontal buoyant jets [4].

Previous measurements on axisymmetric round hydrogen jets [97, 96] revealed that, hydrogen jets show the same behavior to jets of helium[83], propane and other hydrocarbon fuels[93]. In particular, the intensity of centreline velocity fluctuations are similar between the jet and plume regions. In contrast, mass fraction fluctuation intensities increased from a constant asymptotic value of about 0.23 in the jet region to 0.33 0.37 in the plume region[83, 96]. It has also been well established that the mass fraction fluctuation intensities along the centerline and radial variations are also independent of initial density differences between ambient and jet fluids, and collapse onto the same curves, different curves in jet and plume regions, when plotted against the appropriate similarity variables [83, 96, 97, 85].

It is noteworthy that all aforementioned studies, as well as related previous investigations on jets or plumes, have been limited to leaks through flat surfaces, where the direction of the jet mean flow was aligned with the flow origin. In reality, however, flow patterns and dispersion of accidental gas leaks would not be limited to flows through flat surfaces, and leaks through cracks in the side walls of circular pipes should also receive attention. To address this, a recent study was investigated for vertical buoyant jet evolutions through round holes from curved surfaces, numerically and experimentally [107, 105, 72]. Through this recent work, significant discrepancies were found between the evolution of axisymmetric round sharp-edged Orifice Plate (OP) jets through flat surfaces and those originating from curved surfaces. Most notably, jet deflection from the vertical axis, and asymmetric dispersion patterns are always observed in realistic situations. To our knowledge, however, the horizontal jet dispersion from curved surfaces has not yet been investigated.

To investigate the effects of asymmetry and buoyancy on the evolution of horizontal jets issuing from realistic pipeline geometries, jet release experiments were conducted with air and helium, where flow patterns and dispersion of gas through a curved surface originating from a source whose original velocity components were nearly perpendicular to the direction of the ensuing jets. From now on, this jet configuration is referred as a 3D jet. A round hole as one of possible crack geometries, was considered in this study, although another possibility might include thin cracks around the tube or the faulty tube fittings [57], which is not considered here. The horizontal 3D jets were released through a 2 mm diameter round hole in the side of a round tube (closed at one end), with an outer diameter of 6.36 mm and 0.82 mm wall thickness. The outer-scale flow Reynolds numbers (Re_δ), based on the orifice diameter ranged from 19,000 to 51,500, respectively. However, it is noted that for hydrogen jets of equivalent momentum flux, Reynolds number would be 55,915. At these conditions, hydrogen is expected to behave very similar to the helium jets considered here [107]. These realistic jets were also compared to axisymmetric leaks through flat surfaces accordingly. Particle imaging velocimetry (PIV) and planar laser-induced fluorescence (PLIF) were used to measure high-resolution instantaneous velocity and concentration fields, respectively. The purpose of this investigation was to identify and characterize departures from standard axisymmetric jet conditions, and to highlight the buoyancy effect and asymmetric nature of the 3D jets, which ensued from a practical geometry arrangement. It should be noted that, the effect of pipe wall thickness of the crack geometry has not yet been investigated.

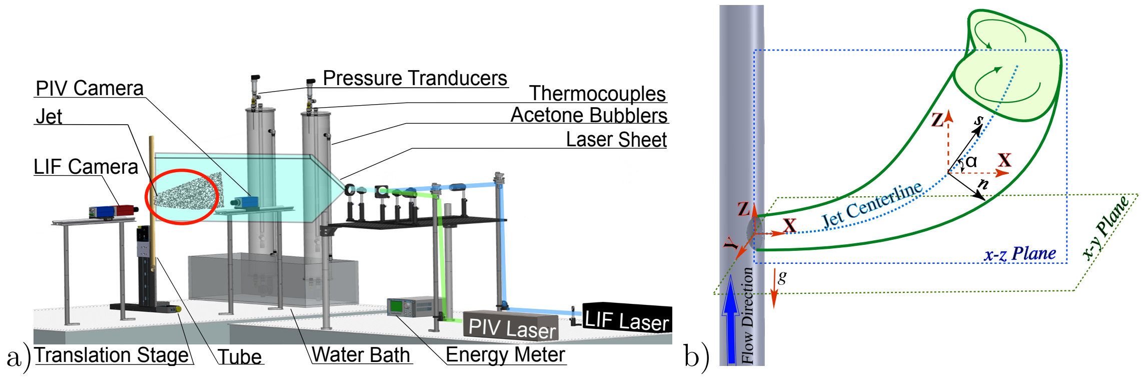

Figure 4.1: a) Schematic of the experimental layout. b) Illustration of horizontal 3D jet flow measurement area (red inset in part a).

4.3 Experimental system and techniques

4.3.1 Flow facility

Figure 4.1a, provides a schematic of the experimental setup used for this study. While, Figure 4.1b, illustrates the jet flow evolution from the tube orifice considered. To capture the three-dimensionality of the jet, measurements were obtained on two different two-dimensional planes (denoted x-z and x-y), as indicated, for both air and helium. Also shown in the figure is the jet centreline, which acts as a reference from which measurements are later obtained in the x-z plane. Owing to potential deviation of the jet from the orifice axis (x-axis), the jet centreline tangent and normal lines are shown as **s** and **n** coordinates in the figure, respectively.

The experiments were conducted within a controlled stagnant environment, at room temperature and pressure ($T_o \sim 22^{\circ C}$, $p_o \sim 100\,\text{kPa}$). Flow controllers (Bronkhorst, EL-FLOW series) were used to control mass flow rates of dry air and pure scientific grade helium to the system, with a high accuracy (standard $\pm 0.5\%$ of reading plus $\pm 0.1\%$ full scale) and precision (within 0.2% of the reading). Di-Ethyl-Hexyl-Sebacate (DEHS) tracer particles were used in PIV measurements, while acetone vapour used as fluorescent tracers for the PLIF experiments. After the test gas was mixed and seeded with the PIV and PLIF tracers, the flow entered the test section of the tube. Isothermal and isobaric conditions were ensured in all measurements. Further specific details can be found in [107]. The orifice, through which the gas dispersed, had a diameter of $D = 2$ mm and was located sufficiently downstream along the tube length to ensure fully developed flow within the tube at the orifice location. Within

Table 4.1: Flow properties

Jet	Orientation , Type	Q [L/min]	$\langle \boldsymbol{u}_j \rangle$ [m/s]	ρ_j [Kg/m^3]	ν_j [m^2/s]	M [N/m]	Fr	Re_δ
Air	H, 3D	15	147.5	1.17	1.54×10^{-5}	50.9	-	19,000
Air	V, 3D	15	147.5	1.17	1.54×10^{-5}	50.9	-	19,000
Air	V, OP	15	127.6	1.17	1.54×10^{-5}	38.1	-	16,500
He	H, 3D	35	399.5	0.165	1.21×10^{-4}	51.3	1.34×10^{6}	51,500
He	V, 3D	35	399.7	0.165	1.21×10^{-4}	51.4	1.34×10^{6}	51,500
He	V, OP	35	341.9	0.165	1.21×10^{-4}	38.3	9.8×10^{5}	44,200

the tube, flow controllers were used to ensure fully developed subsonic and turbulent flow inside the tube.

In order to compare the behaviour of both test gases, for each experimental setup, the averaged momentum flux (M) at the jet exit was estimated and matched for all test cases. This matching was achieved iteratively, by varying the volumetric flow rate (Q) in the system. Here, M was calculated by first obtaining the time-averaged jet exit velocity from two-dimensional PIV measurements. The two-dimensional momentum flux, in units of [N/m], was then calculated from

$$M = \int_{-D/2}^{D/2} \rho_j \langle \boldsymbol{u}(r) \rangle^2 \, \mathrm{d}r \tag{4.1}$$

where the subscript 'j' refers to the conditions at the nozzle, the angle brackets '$\langle\ \rangle$' refers to a time-averaged quantity, and also ρ and r refer to density and radius, respectively. Table 4.1 shows the flow properties used in this study, for the horizontal 3D jet configurations, as well as vertical 3D and OP jets used for comparison [107]; H and V refer to horizontal and vertical orientations, respectively. In all cases, the jets were characterized by the outer-scale Reynolds number, $Re_\delta = \langle \boldsymbol{u}_j \rangle \delta / \nu_\infty$, where, ν_∞ is the ambient fluid kinematic viscosity and δ is the width of the mean axial velocity profile, evaluated from limits of 5% of the centreline velocity at $x \simeq 0$.

4.3.2 Measurement techniques

Particle imaging velocimetry (PIV) was used to capture the two-dimensional velocity flow field information. A dual-head Nd: YAG pulsed laser (New Wave's SOLO III 15 HZ) was used to illuminate a two-dimensional cross-section of the flow, which was seeded with Di-Ethyl-Hexyl-Sebacate (DEHS), with a typical diameter of less than 1 μm, to act as a tracer particle. The light sheet had an approximate height of 5 cm and thickness of 1 mm. The field of view of the camera (PIV CCD) was a 40×30 mm^2 window with an approximate pixel size of 6.5 μm in physical space. Following the procedure of [110], we estimate this resolution to be comparable to the finest scales of the flow, with respect to the Nyquist criterion. Each pair of images were then processed using LaVision DaVis 8.4 software to calculate the global instantaneous flow velocity field. Following the PIV uncertainty propagation method[99], we estimated conservative uncertainty values of 3% and 6% in the time-averaged velocity and Reynolds shear stress profiles, respectively.

To measure the gas concentration, we applied planar laser-induced fluorescence (PLIF). To simultaneously apply PLIF, the flow was also seeded with acetone vapour at consistent rate of $\sim$ 1% by mass fraction. A Pulsed Nd: YAG laser (Spectra-Physics INDI-40-10-HG) was used in order to excite the acetone molecules in a light sheet with an approximate height of 5 cm and a thickness of 350μm, which was then recorded with a PLIF CCD camera. The camera field of view for all cases corresponded to a 38×28 mm^2 window with an approximate pixel size of 6.5 μm. The images were taken at a frequency of 5 Hz and then processed using LaVision DaVis 8.4 software. Following correcting for errors associated with background noise, fluctuations in cross-sectional laser beam intensity, and laser energy per pulse deviations, one can assume the remaining non-uniformity of the scalar field is due to signal to noise ratio (S/N). The error in the S/N can be estimated from the standard deviation of this ratio in an uniform low signal region of the flow field. Based on these data, and uncertainty propagation method, we estimated the uncertainty in the time-averaged and variances of concentration field to be conservative values of 4% and 7%, respectively. For each experimental case, a total of 500 images were acquired to determine the time-averaged molar concentration, $\langle X \rangle$, and variances, X'^2, fields. Further details of the experimental procedure can be found in [107].

Finally, to retain the spatial resolution of the flow field, the full measurement region is covered by two individual imaging windows with at least a 20% overlap between each window. Figure 4.2 shows examples of the instantaneous velocity and concentration fields, for the helium 3D jet in the x-z plane. It should be noted that the flow fields were constructed from two different experiments, where individual imaging windows have been stitched together.

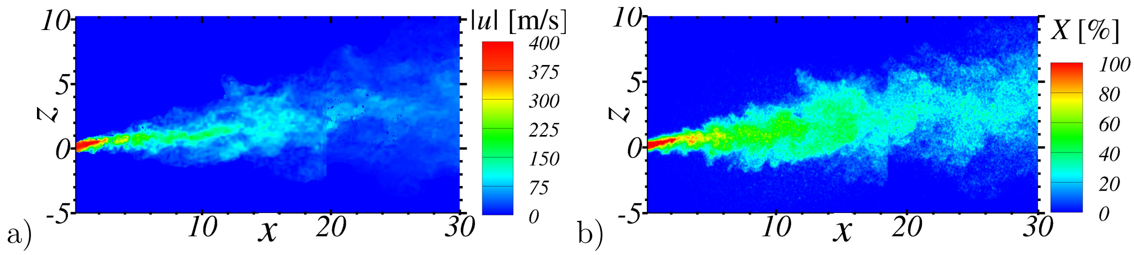

Figure 4.2: Instantaneous a) velocity and b) molar concentration fields obtained from Helium 3D jet in x-z plane from two individual imaging windows stitched together.

Distances reported here have been normalized such that

$$x = \frac{\mathbf{X}}{D}, \qquad y = \frac{\mathbf{Y}}{D}, \qquad z = \frac{\mathbf{Z}}{D}, \qquad s = \frac{\mathbf{s}}{D}, \qquad n = \frac{\mathbf{n}}{D} \tag{4.2}$$

where D, the diameter of the orifice, is taken as the reference length scale.

4.4 Results

4.4.1 Time-averaged flow fields

The time-averaged velocity and molar concentration contours, obtained in both the x-z and x-y planes for all of the 3D jet experiments conducted here, are shown in Fig. 4.3. For both experiments, significantly larger jet spreading was observed in the x-z planes compared to the x-y plane. Clearly, the flow structure was asymmetric in both experiments. The jets were also found to deviate significantly from the horizontal x-axis, for both gases in the x-z plane. In this plane, near the potential-core region, there was also more jet spreading on the lower side of the jet compared to the top side. In the x-y planes of both gases, there were two high-velocity peaks (saddle-back behaviour), at $y \pm 0.5D$, on each side of the x-axis, with a much shorter potential-core length ($\simeq 2D$) compared to the x-z plane. This saddle-back behaviour was previously found to originate from a velocity deficit region which forms inside the orifice due to flow separation as the gas inside the tube encountered the edge of the orifice [107]. Also, there was a shorter potential-core length observed for helium ($\simeq 3D$), compared to air ($\simeq 5D$), as observed in the velocity contours of the x-z planes.

In general, the concentration profiles were qualitatively similar to the velocity profiles presented in Fig. 4.3, with two exceptions. First, the concentration core lengths in both planes were found to be shorter than the velocity potential cores. The

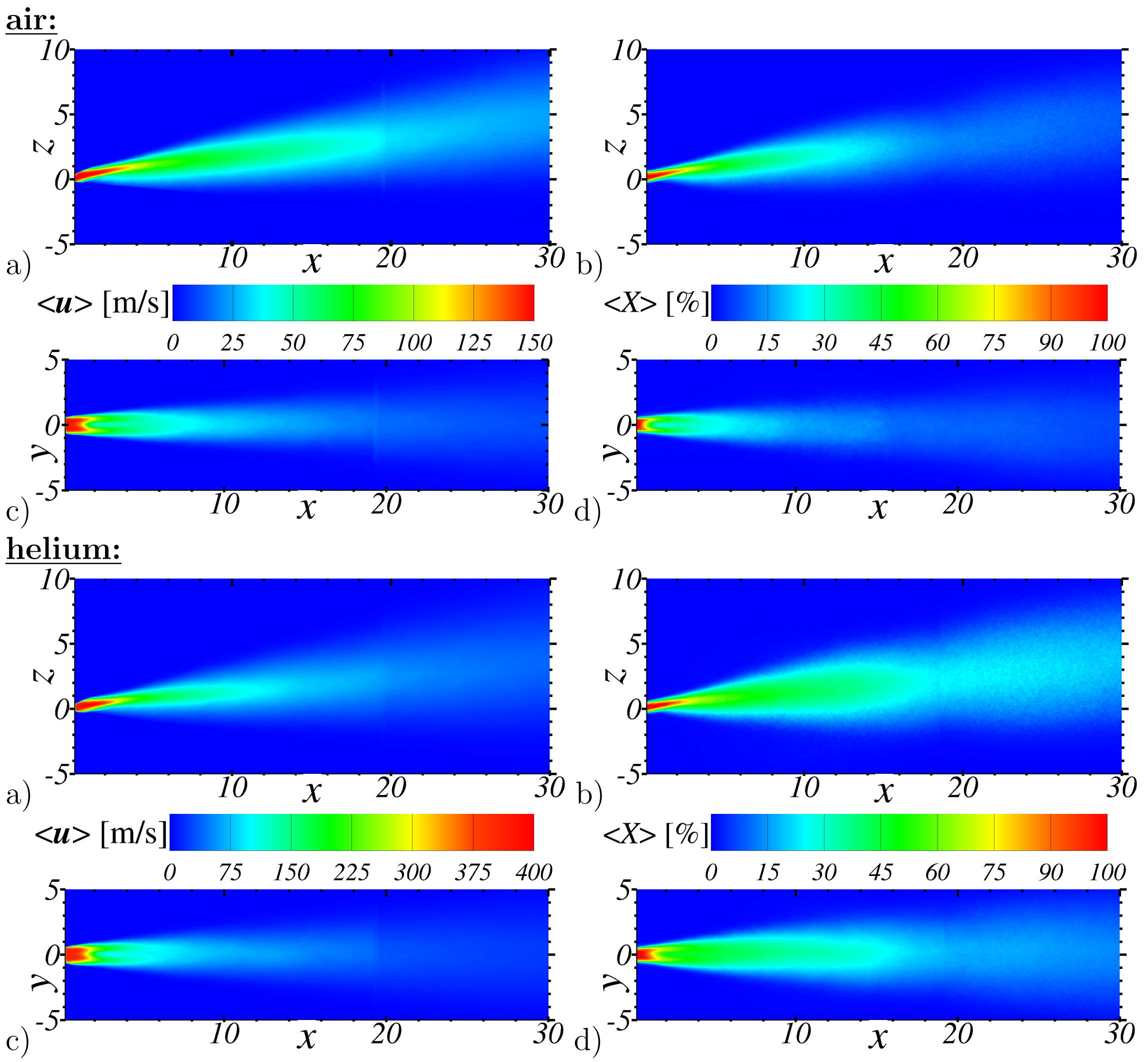

Figure 4.3: Time-averaged velocity and molar concentration contours from round jet on side of tube (3D jet) for air and helium, obtained from a) velocity contours in x-z plane, b) molar concentration contours in x-z plane, c) velocity contours in x-y plane and d) molar concentration contours in x-y plane.

concentration core lengths were approximately $\simeq 4D$ in the x-z plane for both gases, and $\simeq 2D$ and $\simeq 1D$, for air and helium, respectively in the x-y plane. Also, much higher concentration levels, with higher spreading rates, were observed for helium in the far field compared to air. This observation can be attributed to a low Schmidt number ($Sc < 1$), where mass diffusion rates are higher than momentum diffusion rates.

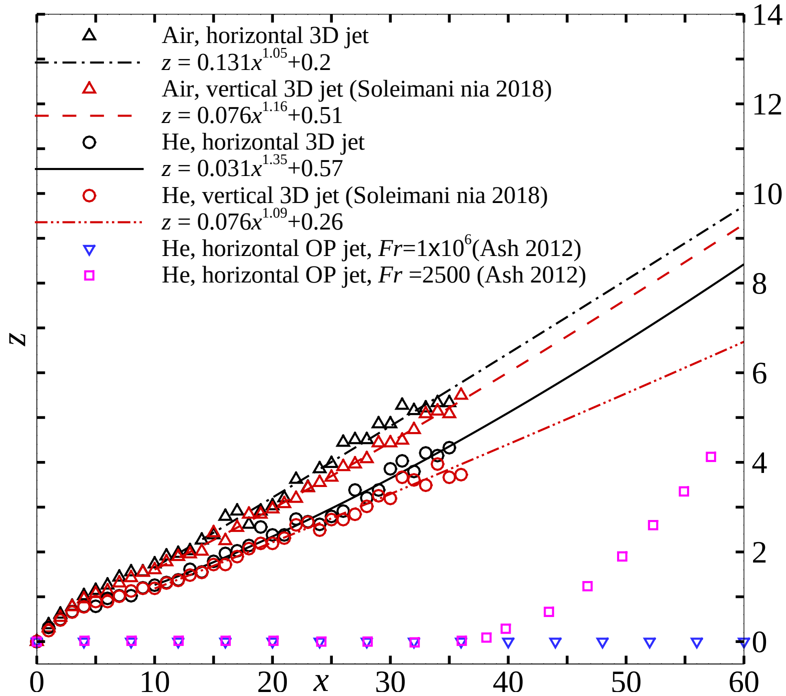

Figure 4.4: Jet centre-lines taken along the location of maximum velocity magnitudes ($|\langle \boldsymbol{u} \rangle|_{\max}(x)$) in x-z plane from measurements. Also shown for comparison are vertical 3D & OP jets [107] and horizontal round OP jets experiments [4].

4.4.2 The jet centreline trajectory

In Fig. 4.4, the jet centreline trajectories, determined in the x-z plane, are presented for all cases. Here, the trajectories were determined by the maximum velocity magnitude, $|\langle \boldsymbol{u} \rangle|_{\max}(x)$, locations. Also shown for comparison are the jet centreline trajectories obtained from previous vertical 3D jet experiments [107], and from horizontal sharp-edged orifice flat-plate (OP) helium jet measurements [4]. In order to determine the effect of buoyancy on the horizontal jets, lines of best fit, using linear regression to power law expressions, were obtained for the far field (beyond $x \geq 10D$), and are also shown in Fig. 4.4. In general, the jet trajectory for the vertical and horizontal air jets were found to be described by a nearly linear relation (i.e. power law exponent ~ 1). The horizontal helium jet, however, was found to have a power law exponent ~ 1.3. Upon extrapolating these relations to the far field, beyond the experimental data collected, it became clear that buoyancy of the helium jet caused significant deflection from the horizontal axis, despite the high Froude number ($Fr = 1.34 \times 10^6$). It should be noted that for horizontal flat-plate OP helium jets, with a comparable Froude number ($Fr = 1 \times 10^6$), such buoyancy effects were not observed [4].

4.4.3 Velocity decay and jet spreading rates

Fig. 4.5a shows the inverse time-averaged velocity decay ($\langle \boldsymbol{u}_j \rangle / \langle \boldsymbol{u}_c \rangle$) along the jet centrelines (s-coordinate illustrated in Fig. 4.1b) for all experiments. Here, the subscript 'c' refers to the conditions at the jet centreline, while the subscript 'j' refers to the jet exit condition. Also shown, for comparison, are velocity decay correlations [130] for compressible subsonic and supersonic axisymmetric round jets, along with velocity decay rates obtained from vertical 3D and OP jet experiments [107], and horizontal OP helium jet measurements [4]. Upon comparison to the Witze correlations [130], the air and helium OP jet experiments were found to reproduce well the expected velocity decay rate, with helium jet decaying faster than the air jet. On the other hand, the decay rates observed in the experimental 3D jets were much faster compared to the axisymmetric jets. In general, upon comparison between horizontal and vertical 3D jets, buoyancy was not found to significantly affect the velocity decay rates.

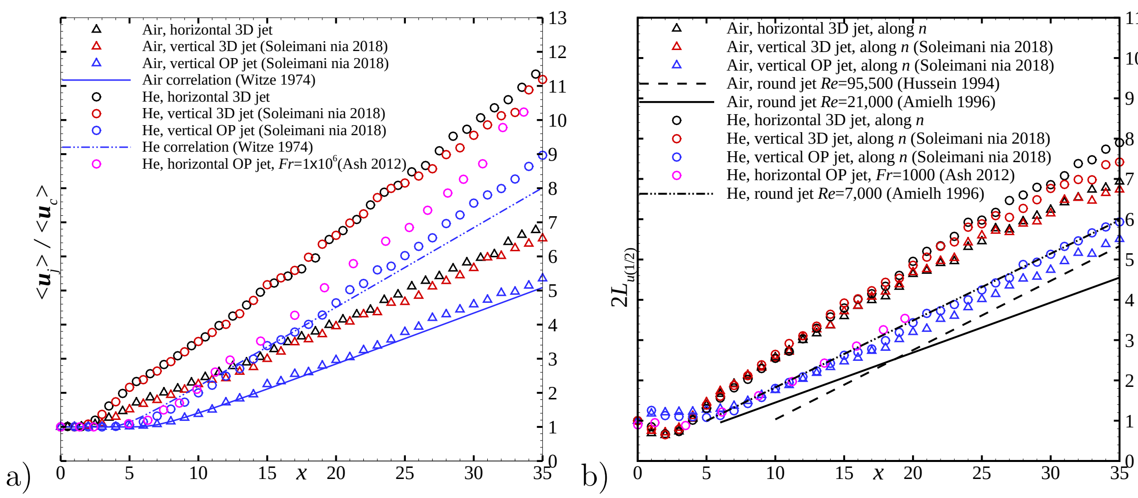

Figure 4.5: a) Inverse time-averaged velocity decay and b) jet velocity widths ($2L_{u(1/2)}$) obtained along the $|\langle \boldsymbol{u} \rangle|_{\max}(x)$ centrelines, in x-z plane from measurements. Note, n-coordinate refers to lines which are normal to the centreline, and coplanar with the x-z plane (see the coordinate system in Fig.4.1 b). Also shown, for comparison are axisymmetric round jet correlations [130], and vertical 3D & OP jets, horizontal round OP jets and round pipe jet experiments [107, 4, 56, 2].

In the x-z plane, Figure 4.5b presents the jet velocity widths ($2L_{u(1/2)}$), that have been obtained by determining the locations where $|\langle \boldsymbol{u} \rangle| = 0.5 |\langle \boldsymbol{u} \rangle|_{\max}(x)$ along lines which were orthogonal to the jet-centrelines. These orthogonal lines have been indicated previously as coordinate 'n' in Fig. 4.1b. For the 3D jets, in all cases, a slight contraction in the jet widths has been observed from $1D < x < 4D$. Beyond this point, the jet spreading rates, along n, were observed to be much greater compared to the axisymmetic jets for all cases. Moreover, the air and helium jet spreading, from the 3D experiments, was found to be comparable for both gases. However, In the far field (beyond $x \geq 13D$), the helium 3D jets exhibited higher spreading rates, compared to air. This trend was slightly more clear upon comparison to the horizontal 3D cases between helium and air. In general, the OP jets were found to have nearly constant jet widths in the potential core region, up until $x \sim 5D$. From this point on, the OP jet widths were found to be much smaller compared to 3D jets, with the expected linear increase in jet spreading rates of previous axisymmetric round jet experiments for a wide range of Reynolds numbers [56, 2].

4.4.4 Scalar concentration decay and jet spreading rates

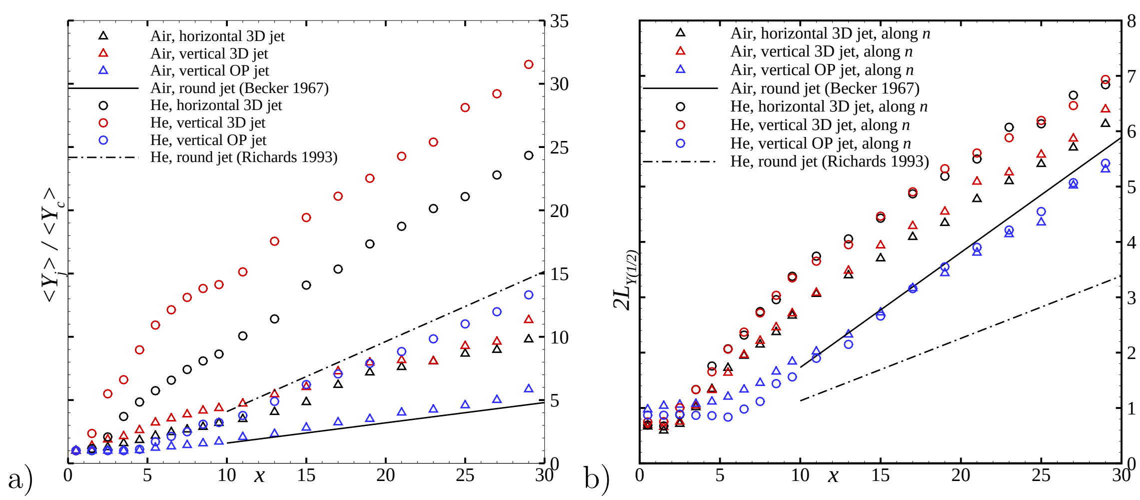

Figure 4.6: a) Inverse time-averaged jet gas mass fraction decay and b) mass fraction widths ($2L_{Y(1/2)}$) obtained along the $\langle Y \rangle_{\max}(x)$ centrelines, in x-z plane from measurements. Also shown, for comparison are vertical 3D & OP jets, and round pipe jet experiments [107, 6, 93].

Figure 4.6a shows centreline evolution of the inverse time-averaged jet gas mass fraction, $\langle Y_j \rangle / \langle Y_c \rangle$, for both air and helium measurements. Here, the jet gas mass fractions were determined from the measured mole fractions through

$$Y = \frac{X W_j}{\overline{W}} \tag{4.3}$$

where X and W_j refer to the mole fraction and molecular weight of the jet gas, respectively, and $\overline{W}$ refers to the mean molecular weight of the local jet gas-ambient air mixture given by

$$\overline{W} = XW_j + (1 - X)W_{\text{air}} \tag{4.4}$$

Also shown, for comparison, are the centreline mass fraction decay rates for axisymmetry round air [6] and helium jets [93], along with the mass fraction decay rates obtained from vertical 3D and OP jet experiments [107]. In general, the air and helium vertical OP jet experiment mass fraction decay rates compared well to previous axisymmetry round pipe jet experiments [6, 93], where helium jets were always observed to decay faster than air jets. It is noted, however, that the slight differences observed in decay rates for the axisymmetric helium jets (OP and pipe jets) are likely due to differences in the Reynolds numbers between experiments ($Re = 4,000$ for the round pipe jets compared to $Re = 44,200$ for the OP helium jet) [86]. Differences in the geometry of the jet outflow condition may have also been a factor. Also, the centreline mass fraction decay rates observed in the experimental 3D jets were much faster compared to the axisymmetric jets. Moreover, upon comparison of the 3D helium jets, the vertical orientation was found to have a faster mass fraction decay rate compared to the horizontal case. Such differences in behaviour was not observed for the 3D air jets, suggesting that buoyancy plays a significant role on the mass fraction decay rates. Also, upon comparison to the velocity decay rates in Fig. 4.5a, we note that the jet centerline mass fraction decays faster than the velocity for helium, owing to the low Schmidt number ($Sc < 1$).

As was done for the velocity field, the jet widths based on the jet gas mass fraction ($2L_{Y(1/2)}$) have been obtained for each experiment, and presented in Fig. 4.6b. This was achieved by determining the locations where $\langle Y \rangle = 0.5\langle Y \rangle_{\max}(x)$ along orthogonal lines to the jet centreline, in the x-z planes. For all 3D jet cases, a slight contraction in the jet mass fraction widths was observed from $x < 4D$, as was previously observed for the jet widths based on velocity. Beyond this point, the jet scalar growth rates, along n, were observed to be much greater compared to the axisymmetic jets for all cases. The helium jet also exhibited a faster spreading rate compared to air, in both horizontal and vertical cases. The air and helium OP jets were found to have nearly constant mass fraction widths in the potential core region, up until $x \sim 5D$. After the potential core region, the jet scalar width was found to be much smaller compared to 3D jets, and increase linearly, consistent with the jet mass fraction spreading rates of previous axisymmetric round jet experiments [6, 93].

4.4.5 Jet centreline statistics

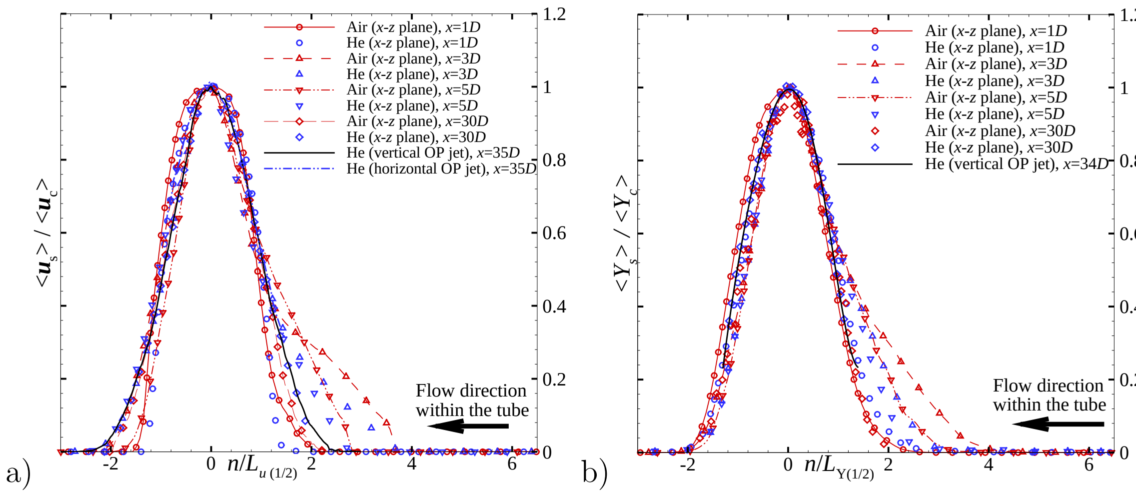

Figure 4.7: a) Normalized time-averaged velocity, and b) concentration profiles along jet centrelines in x-z plane, taken at various heights for both air and helium. Time-averaged velocity and concentration profiles are also compared to experimental axisymmetry horizontal ($Fr = 1 \times 10^6$)[4] and vertical round OP jets [107].

In the x-z plane, the normalized time-averaged s-velocity components and jet gas mass fraction profiles, for all 3D and OP jet experiments, are shown in Fig. 4.7 along the n-coordinate (see Fig. 4.1b) for several downstream locations along the jet centreline (s-curve in Fig. 4.1b). It should be noted that the s-component velocities, presented here, were normalized by the local centreline velocity magnitudes, $\langle \boldsymbol{u} \rangle_c(s)$. The time-averaged jet gas mass fractions ($\langle Y \rangle$) have been normalized by the local centreline jet gas mass fraction, $\langle Y_c \rangle(s)$. Also, in the figure, the n-coordinates, normal to the centreline s-curve, were normalized by the jet velocity half widths ($L_{u(1/2)}$), determined from Fig. 4.5b, and the jet gas mass fraction half widths ($L_{Y(1/2)}$), determined from the locations where $\langle Y/Y_c \rangle = 0.5$, respectively. In general, all 3D jet cases developed into a self-similar Gaussian-like distribution of velocity within the range $|n/L_{1/2}| < 1$ for $x \leq 5D$. However, notable deviations from the self-similar solution were observed near the tail ends of the curves in the x-z plane, beyond this range, especially in the opposite stream wise direction of the flow within the tube ($+n$ direction). For vertical 3D jets, this was previously found to be due enhanced mixing associated with the original flow orientation relative to the orifice, and also curvature of the tube [107]. Both air and helium experiments were found to exhibit significantly more velocity and jet gas mass fraction spreading to the lower side of the jet centre (in the $+n$ direction), with more spreading observed in this region for helium compared to air. Beyond $x > 5D$, in the far field, the experimental 3D air and helium jets developed into the self-similar Gaussian distribution obtained from the OP jets for the full range of n.

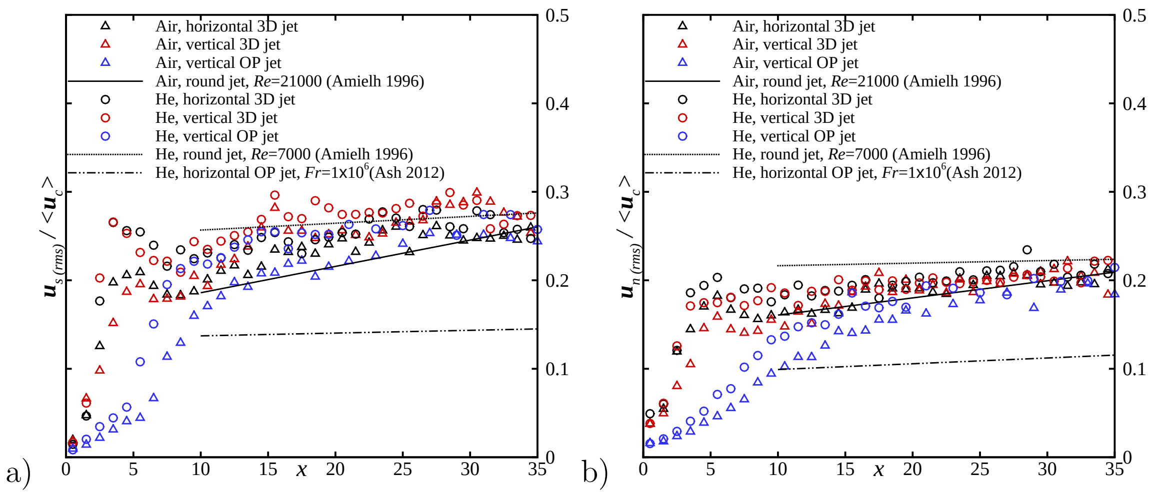

Figure 4.8: Axial development of turbulence intensities along jet centrelines, a) tangential turbulence intensity component ($\boldsymbol{u}_{s(rms)}/\langle \boldsymbol{u}_c \rangle$) and b) orthogonal turbulence intensity component ($\boldsymbol{u}_{n(rms)}/\langle \boldsymbol{u}_c \rangle$) for experiments. Also shown, for comparison are vertical 3D & OP jets, horizontal OP jet, and round pipe jet experiments [107, 4, 2].

Fig. 4.8 shows the normalized axial evolution of the r.m.s. velocity fluctuation components in the s and n directions, tangential and orthogonal to jet centreline, where $\boldsymbol{u}_{(rms)} = \langle \boldsymbol{u}'^2 \rangle^{1/2}$. It should be noted that the prime ($'$) represents the instantaneous fluctuating quantity ($\boldsymbol{u}' = \boldsymbol{u} - \langle \boldsymbol{u} \rangle$). For the 3D vertical and horizontal helium jets, the tangential turbulence intensity reached an asymptotic value of $\sim 26\%$ at $x = 3D$, whereas such a value was not observed until $x = 20D$ and $x = 15D$ for the 3D horizontal and vertical air jets, respectively. This trend was also observed in pipe jet measurements [2] and also the current vertical OP jets, where helium reached the asymptotic value closer to orifice, at $x = 15D$, compared to air at $x = 32D$. However, it appears that this asymptotic value of $\sim 26\%$ would be reached in the far field ($x > 33D$) for all jets, except the horizontal helium OP jet measurements [4]. It should be noted that lower turbulent intensities of the horizontal helium OP jet, observed in both tangential and orthogonal components, are likely due to higher initial turbulent intensities reported for the horizontal helium OP jet (not shown)[74]. Also, lower spatial resolution of the PIV measurement compared to the current experiments (almost 3 times less), may have been a factor. The same remark is valid for the orthogonal turbulence intensity, as the 3D helium jets reached the asymptotic value of $\sim 19-22\%$ more closer to orifice at $x = 5D$, compared to air at $x = 15D$. Also, the OP vertical helium jet reached this peak turbulence intensity at $x = 15D$, whereas such turbulence intensity was not recovered until $x = 30D$ for air. In general, the intensity of tangential velocity fluctuations was higher than the orthogonal components, as observed in previous studies [83, 2].

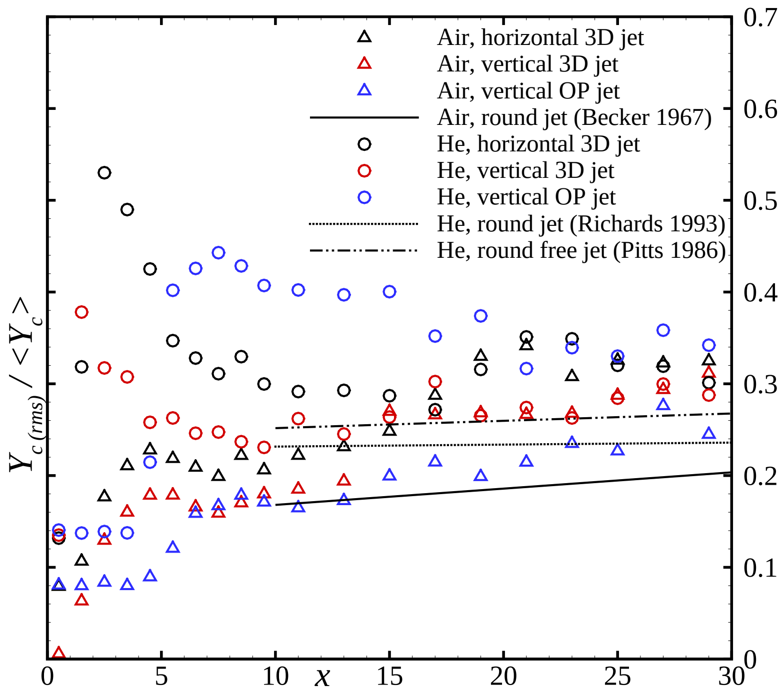

Figure 4.9: Normalized axial evolution of mass fraction fluctuation intensities along jet centrelines, $Y_{c(rms)}/\langle Y_c \rangle$, for experiments. Also shown, for comparison are vertical 3D & OP jets, and round pipe jet experiments [107, 6, 85, 93].

Fig. 4.9 shows the normalized axial evolution of the r.m.s. jet gas mass fraction fluctuations (unmixedness), $Y_{c(rms)}/\langle Y_c \rangle$, along the jet centreline, for all experiments. In the vertical 3D jets, helium reached the asymptotic value of $\sim 26\%$ at $x = 5D$, whereas such a value was not recovered until $x = 14D$ for air. This value is in good agreement of the asymptotic value previously reported in helium free jets [84]. Also, in horizontal 3D jets, helium reached an umixedness value of $\sim 33\%$ at $x = 5D$, but then decreased to the asymptotic value of the vertical jets ($\sim 26\%$) at $x = 17D$, and then again increased to the asymptotic value of $\sim 33\%$ for the rest of the measurement domain. For the horizontal 3D air jet, the unmixedness reached a value of $\sim 20-24\%$ at $5D < x < 15D$, which is in good agreement with the values reported in literature for the far field ($\sim$ 21 – 24%) [83, 15, 93]. Then, the unmixedness recovered the asymptotic value of $\sim 33\%$ at $x = 19D$ for the rest of observation domain. For the vertical OP air jet, the observed profile followed closely the values of those reported for smooth contraction (SC) air jets [6] in the near field ($5D < x < 15D$), and then increased to the asymptotic value of $\sim 23\%$ for the rest of the domain. On the other hand, for the vertical OP helium jet, the unmixedness reached a peak value of 0.43 at $x = 7D$, then slowly decreased to the value of $\sim 33\%$ in the far field, from $x > 20D$. it should be noted that, even though the unmixedness values were not consistent between the helium and air OP jets in the measurement domain, extrapolation of the data (not shown) revealed that the far field unmixedness would converged to the same value at about $x > 50D$.

Higher order statistics were also acquired for the experiments conducted here. The time-averaged Reynolds stress profiles obtained from measurements, $\langle \boldsymbol{u}'_s \boldsymbol{u}'_n \rangle$, are presented in Fig. 4.10 a). In this case, the Reynolds stress quantities have been normalized by local centreline velocity, $\langle \boldsymbol{u}_c^2 \rangle (s)$. In the x-z plane, the air and helium experiments captured well the far field self-similar profile, with the helium have slightly higher magnitude of the Reynolds stress compared to the air, as seen before in the axisymmetry jets [83, 107]. However, to the left of the jet centre (in the $-n$ direction), the horizontal 3D jet experiments were found to have a higher magnitude of the Reynolds stress compared to the axisymmetry jets, in the near field $x \leq 10D$. Also, within for $x \leq 5D$, a higher Reynolds stress was observed beyond $|n/L_{1/2}| < 1$. It should also be noted that there is an offset of the zero crossing of Reynolds stress profiles form jet centreline ($n/L_{1/2} = 0$) for $3D \leq x \leq 5D$ and $x = 3D$ for helium and air measurements, respectively . This was previously noted for the vertical 3D jet experiments [107], and brings into question the capability of conventional eddy-viscosity models to properly approximate the Reynolds stress for this type of turbulent flow.

Finally, the normalized concentration variance profiles ($\langle Y_s'^2 \rangle / \langle Y_c^2 \rangle$), obtained from experiments, are presented in Fig. 4.10 b). In the x-z plane, the initial development of the 3D air jets had a higher variance of concentration to the left of the jet centre (in the $-n$ direction) within the ranges of $x \leq 10D$. While, helium jet initial profile exhibited semi symmetry saddle-back profile up to $x \leq 2D$, after this point variances profile recovered the semi gaussian profile with a maximum magnitude

air:

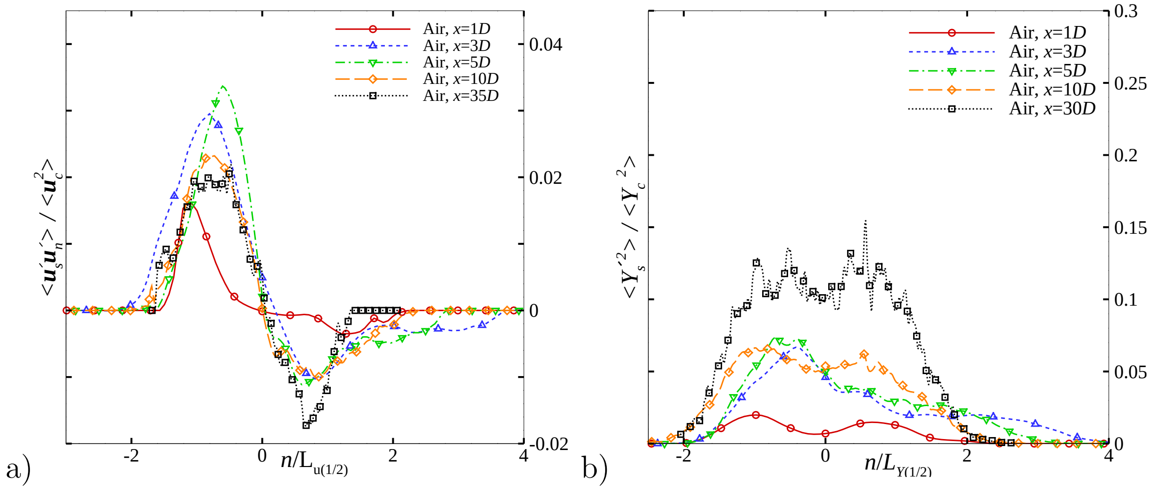

He:

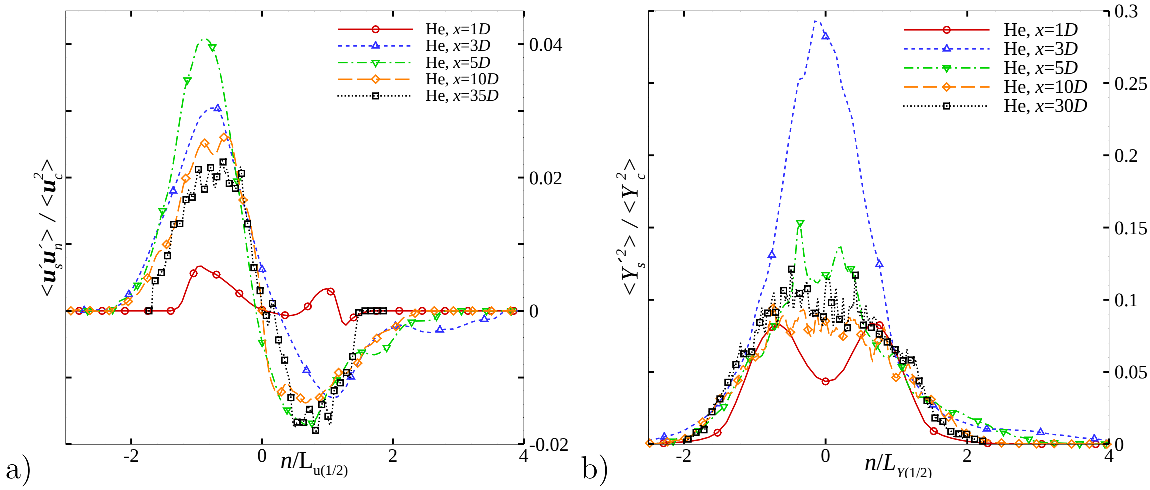

Figure 4.10: a) Normalized time-averaged Reynolds shear stress ($\langle \boldsymbol{u}'_s \boldsymbol{u}'_n \rangle / \langle \boldsymbol{u}_c^2 \rangle$) and b) concentration variance ($\langle Y_s'^2 \rangle / \langle Y_c^2 \rangle$) profiles along jet centrelines for air and helium experiments. Here, the profiles are taken at various heights for air and helium measurements in x-z planes.

at $x \sim 3D$. Beyond $x \geq 10D$ jet heights, in the far field, the concentration variance profiles revealed self-similar profile for both air and helium 3D jet experiments. Also in the core region, much like the axisymmetry jet evolutions, the 3D jet experiments were found to contain a minimum variance near the jet centre, except for helium jet at $x \sim 3D$. In general, the magnitudes of mass fraction variance of the helium were higher compared to air, more specifically in the near field.

4.5 Discussion

4.5.1 Self-similarity analysis

In the previous section, for both near and far fields, different velocity and scalar statistical properties were reported for 3D and OP jets of helium and air. It has been well established that these variations are influenced by differences in density, initial conditions and turbulence structures of the jets [93, 133, 76]. Self-similarity (or self-preservation) state in turbulent flows is described as when the flow statistical quantities can be assumed by simple scale factors which depend on only one of the variables. As a consequence, both velocity and scalar pseudo-similarity solutions, in constant or variable density jets, evolve in similar ways when appropriate similarity variables have been used [83, 85, 15]. These pseudo-similarity solutions have been used to develop the analytical models, and approximate the velocity & scalar decays and growth rates in jet flows. However, It should be noted that the turbulent structure throughout the entire flow field is particularly influenced by the initial jet outflow conditions. As a result, different similarity states in the far field are possible [35, 77]. In this section, self-similarity analyses conducted on the current measurement data are presented.

The pseudo-similarity solution, in the turbulent jet, is approximate in the pure jet region, where inertia forces dominate the flow. To estimate the extent of the pure jet region, the following non-dimensional buoyancy length scale (along the x-axis, shown in Fig. 4.1b) [15] was used:

$$x_b = Fr^{-\frac{1}{2}}(\frac{\rho_j}{\rho_\infty})^{-\frac{1}{4}}x \tag{4.5}$$

where the Froude number is Fr $(= \frac{\boldsymbol{u}_j^2\rho_j}{(\rho_\infty - \rho_j)gD})$, and g is the acceleration due to gravity. For the flow conditions reported in Table 4.1, x_b varies from 0 to 0.042 for $0 < x < 30D$, the range of current measurements. Therefore, the hypothetical range of the pure jet region [15], $x_b < 0.5$, is satisfied for all flow conditions considered in this study.

The centreline velocity and mass fraction decays for nonreacting jets, for both constant and variable density flows, can be correlated as

$$\frac{\langle \boldsymbol{u}_j \rangle}{\langle \boldsymbol{u}_c \rangle} = C_u \left[\frac{(\mathbf{X} - \mathbf{X}_{0,u})}{D^*_{ef}} \right] \tag{4.6}$$

and

$$\frac{\langle Y_j \rangle}{\langle Y_c \rangle} = C_Y \left[\frac{(\mathbf{X} - \mathbf{X}_{0,Y})}{D_{ef}} \right] \tag{4.7}$$

where the subscripts 'j' and 'c' refer to the conditions at the jet exit and centreline, respectively; $\mathbf{X}_{0,u}$ and $\mathbf{X}_{0,Y}$ are the dimensional jet virtual origins obtained from inverse centreline velocity and mass fraction decay profiles, respectively, and C_u & C_Y are empirical constants obtained with least-mean-square fitting the measured data to Eqs.[4.6]-[4.7]. The concept of effective diameter, $D_{ef} = \frac{2\dot{m}_j}{\sqrt{\pi \rho_\infty M_j}}$, is defined to account for variations in both the jet fluid density and mean jet exit velocity profile in the turbulent jet flows [117, 6, 27, 85, 93]; where $\dot{m}_j$ and M_j are the exit mass flux and momentum flux for the jet, respectively. Physically, D_{ef}, corresponds to the orifice diameter of a jet having the same momentum and mass flux, but with a density of the ambient fluid instead of the jet fluid. Since asymmetry structures were always observed at the jet exit [107], three dimensional measurements of velocity and concentration are required to accurately calculate D_{ef} in the 3D jets. However, if the density and velocity profiles are uniform at the jet exit, then D_{ef} takes the form as originally introduced by Thring & Newby[117], $D_{ef} = D(\frac{\rho_j}{\rho_\infty})^{\frac{1}{2}}$. It should be noted that in the case of constant density jet (air jet) the effective diameter is equal to the orifice diameter.

Here, different effective diameter (D_{ef}) versions available in the literature, are examined by collapsing the helium data on to the comparable air data, for both hyperbolic decay velocity and scalar laws (Eqs.[4.6]-[4.7]). For the mass fraction decay law, the original effective diameter $D_{ef} = D(\frac{\rho_j}{\rho_\infty})^{\frac{1}{2}}$ [117], used to collapse the scalar data. For the measured velocity data, a modified version of effective diameter, given as $D^{**}_{ef} = D(\frac{\rho_c}{\rho_\infty})^{\frac{1}{2}}$ [114], provides a better correlation in the near field of the flow. Here the subscript '∞' refers to the outer ambient fluid, air. However, the modified version of effective diameter ($D^{**}_{ef} = D(\frac{\rho_c}{\rho_\infty})^{\frac{1}{2}}$) requires knowledge of the local centreline concentration; this version cannot be applied in the absence of concentration data . Upon further analysis, it was found that if the second root, in the original effective diameter ($D_{ef} = D(\frac{\rho_j}{\rho_\infty})^{\frac{1}{2}}$), is replaced by $\sim$ thrid root, then the velocity data shows good correlation with the collapsed curves of the aggregate 3D jet data in both the near and far fields. Therefore, we used this new modifed version of effective diameter, $D^*_{ef} = D(\frac{\rho_j}{\rho_\infty})^{0.3}$, to correlate the centreline velocity decay (Eq.[4.6]). It should be noted that the latter modified version of effective diameter, D^*_{ef}, may only valid for the current 3D jet experiments, due to the effects of specific conditions at the jet such as geometry, flow structures, density profiles, and velocity profiles.

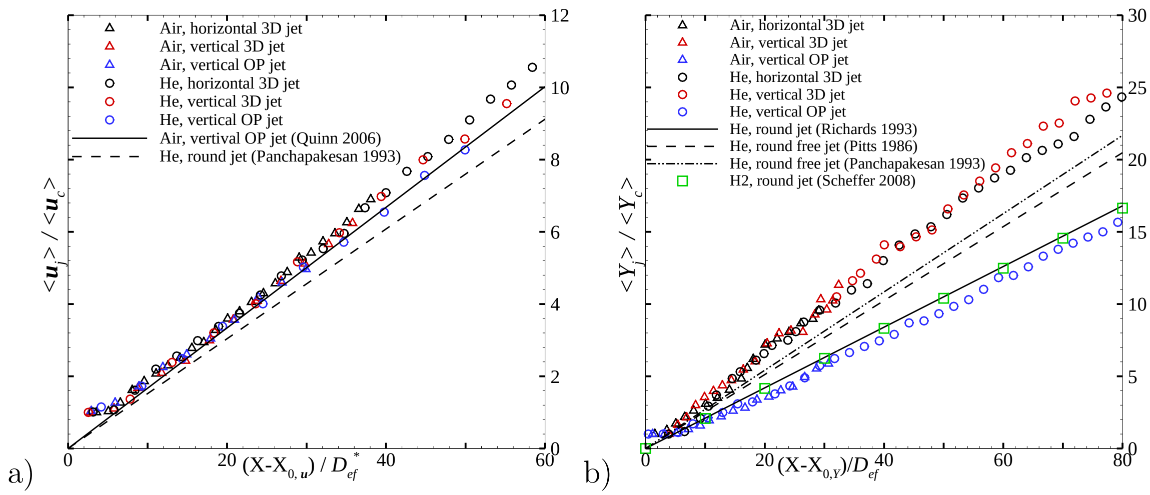

Figure 4.11: Inverse axial velocity and mass fraction decay along jet centrelines versus downstream distance non-dimensionalized by D^*_{ef} and D_{ef}, a) velocity ($\langle \boldsymbol{u}_j \rangle / \langle \boldsymbol{u}_c \rangle$) and b) mass fraction ($\langle Y_j \rangle / \langle Y_c \rangle$) for experiments. Also shown, for comparison are vertical 3D & OP jets, and round pipe He & H2 jet experiments [107, 93, 97].

In Fig. 4.11, the centreline revolution of the inverse velocity (Fig. 4.5 a) and mass fraction (Fig. 4.6 a) profiles have been reconstructed for the 3D jets as a function of distance from the virtual origins, normalized with effective diameter, i.e. ($\left[\frac{(\mathbf{X}-\mathbf{X}_0)}{D_{ef}}\right]$). Self-similarity decay lines, obtained by curve fitting the results, are also shown for OP, Smooth Contraction (SC), pipe round free, and pipe round confined jets [89, 83, 93, 84, 97]. The experimental data for all helium jets were collapsed onto the comparable air jets, verifying that the correct version of effective diameter along with virtual origin distances are the appropriate scaling parameters to correlate both velocity and scalar pseudo-similarity solutions in the constant or variable density jets. The velocity decay rates of all 3D jets are very similar to OP jets based on a comparison of velocity decay plots (4.11 a). However, the mass fraction decay profiles of 3D jets show a steeper decay rate than is observed for OP jets (4.11 b). This observation

Table 4.2: Centerline velocity and scalar pseudo-similarity decay properties

Jet	R_ρ	$\mathbf{X}_{0,u}/D$	$C_{\boldsymbol{u}}$	$\mathbf{X}_{0,Y}/D$	C_Y
Air, 3D Horizontal	1	-3.07	0.174	-1.07	0.326
Air, 3D Vertical	1	-2.78	0.170	-3.39	0.319
Air, OP Vertical	1	3.08	0.169	-0.68	0.224
Air, OP Vertical [89]	1	2.15	0.167	–	–
He, 3D Horizontal	0.14	-1.29	0.175	-0.95	0.313
He, 3D Vertical	0.14	-1.45	0.170	-6.42	0.316
He, OP Vertical	0.14	3.54	0.170	2.32	0.221
He, SC Vertical [83]	0.14	–	0.152	–	0.271
He, Pipe Vertical [93]	0.14	–	–	3.0	0.212
He, Pipe Vertical [84]	0.14	–	–	4.45	0.256
H2, Pipe Vertical [97]	0.069	–	–	4.0	0.208

further supports the fact that the velocity field spreads slower than the concentration field. This conclusion is supported by the preferential transport of scalar quantities over momentum flux that is evident in previous studies [114, 70]. It is also clear that a pipe confined jet of hydrogen [97] follows the same decay rate of those pipe confined jets of helium [93]. This observation is consistent with the fact that the scalar decay rate is independent of initial density ratio but influenced notably by the jet initial conditions and other potential factors such as measurement conditions.

Further comparisons of the centreline pseudo-similarity decay properties are shown in Table 4.2. Here, R_ρ is a ratio of the jet fluid density to the ambient fluid, $R_\rho = \frac{\rho_j}{\rho_\infty}$. For both velocity and mass fraction quantities, these self-similarity properties are obtained from data fitted by a least-mean-square algorithm to Eqs. (4.6)-(4.7). Table 4.2 also provides a comparison of self-similarity properties of OP, SC, pipe round free, and pipe round confined jets [89, 83, 93, 84, 97]. It should be noted that dimensional virtual origin distances, $\mathbf{X}_{0,u}$ and $\mathbf{X}_{0,Y}$, are normalized by the jet diameter (D).

Upon comparison of the velocity decay slopes, for the air OP jets, the value of $C_u = 0.169$ is in good agreement with the value of 0.167 reported previously for the air OP jet [89]. The small difference is associated with higher Reynolds number of $Re = 1.84 \times 10^5$ compared to present study ($Re = 1.65 \times 10^4$), which results in a decrease of the velocity decay rate. The helium OP jet shows slightly higher decay rate to that of the air OP jet, as shown previously in Fig. 4.5 a, but with a minor increase of the virtual origin, x_{0u}. It is well known that the virtual origin of a jet is highly influenced by the jet initial conditions and does not vary in any systematic manner. The vertical helium and air 3D jets have almost the same decay slopes, whereas the horizontal helium 3D jet has a slightly higher slope than the comparable horizontal air jet, as previously noticed in Fig. 4.5 a. In general, a higher velocity decay rate is observed for 3D jets compared to OP, SC and pipe jets based on a comparison of the velocity decay slopes. This is associated with enhanced turbulent mixing in the 3D jets, as a result of their asymmetry flow pattern, specifically in the near field.

In contrast, by comparing the helium mass fraction decay slopes in table 4.2, it is found that reported C_Y values in the literature for SC and pipe jets are larger than those OP values obtained in the current study. This is in contrast with the well established fact that the OP jets exhibit the highest mixing rate, followed by the SC jets and finally the pipe jets [76]. It should be noted that the value of $C_Y = 0.271$ reported for SC helium jet[83], is obtained without considering the scalar virtual origin, $\mathbf{X}_{0,Y}$, in Eq.(4.7). In addition, $C_Y = 0.256$ reported for the pipe jet [84], is correlated based on a different term in the effective diameter equation. The pipe jet data has been correlated using the factor of $(\frac{\rho_j}{\rho_\infty})^{0.6}$ instead of $(\frac{\rho_j}{\rho_\infty})^{\frac{1}{2}}$ in the original version of D_{ef} which would explain the higher C_Y value reported for the pipe jet in their measurements. The mass fraction decay slope observed for helium 3D jets is smaller than for air 3D jets. However, upon comparison of mass fraction decay slopes between the 3D and other jets, it is found that the 3D jets have the highest decay slopes. This result further supports the fact that significantly higher turbulent mixing and entertainment rates occur in the 3D jets compared to the axisymmetry jets, as recently concluded in the experimental and numerical study on the vertical 3D jet [107].

4.5.2 Buoyancy effect

For the 3D jets, it was found that the perpendicular stream-wise axis of the hole, relative to the flow direction within the tube, resulted into a deflection of the jet away from it's horizontal $x-$axis. Initially, from Fig. 4.4, all 3D jets emerged with a similar deflection angle. But only after $x > 2D$, both horizontal and vertical air jets were found to deflect more than helium jets. Buoyancy forces, aside from less significant contributors, are a probable cause of the increased deflection observed for vertical air jets in comparison to helium jets. But from the comparison of helium jets centreline trajectories (Fig. 4.4), buoyancy effect is clearly the main contributor in the significant deflection of horizontal case from the horizontal $x-$axis compared to vertical jet. Whereas such deflection were not observed in horizontal air jet compared to vertical case.

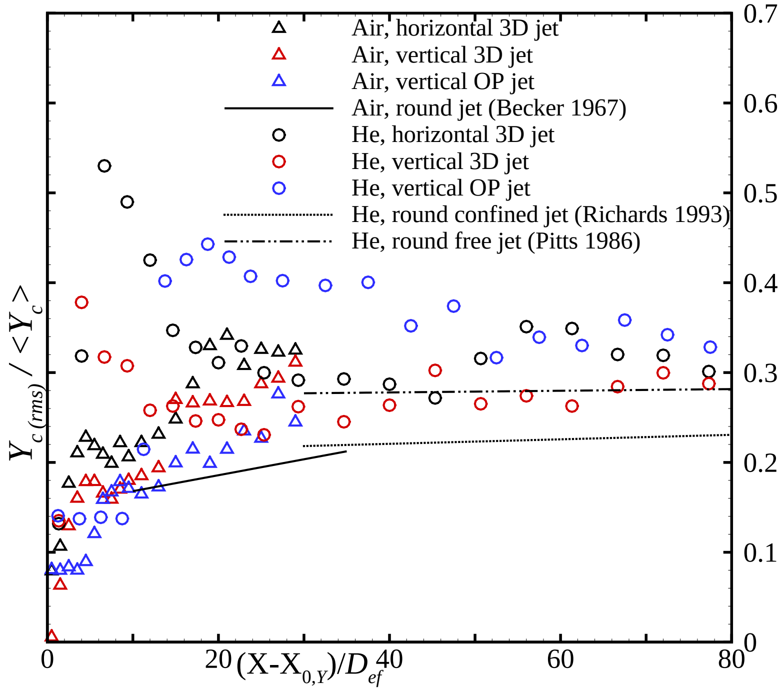

Figure 4.12: Centreline evolution of normalized mass fraction fluctuation intensities, $Y_{c(rms)}/\langle Y_c\rangle$, versus downstream distance non-dimensionalized by D_{ef} for experiments. Also shown, for comparison are vertical 3D & OP jets, and round pipe jet experiments [107, 6, 85, 93].

Figure 4.12 reconstructed the unmixedness profile (Fig. 4.9) for the 3D jets as a function of distances from the virtual origin ($\mathbf{X}_{0,Y}$) and normalized by effective diameter (D_{ef}). Along with same remarks observed as those presented in Fig. 4.9, it is clear that effective diameter would not be a necessary length scale for unmixedness profile, since helium and air data are already collapsed on the same curves by scaling with the jet orifice diameter (D). All 3D jets recovered the asymptotic value of $\sim$ 26% , reported for variable density free round jet [84], which is closer to the orifice compared to axisymmetry OP jets. Further downstream, the horizontal 3D jets reached a higher asymptotic plateau ($\sim$ 33%) in the far field. This difference would might be solely associated with buoyancy effect, which becomes dominant closer to the orifice, in the horizontal cases compared to the vertical 3D jet. Other parameters such as co-flow, initial conditions, Reynolds number, and measurement uncertainty could also play a significant role [85]. However, their effects are negligible since the similar experimental system and parameters have been used in current measurements. Despite these differences, it is clear that centreline unmixedness is independent of R_ρ and achieves asymptotic value based on the initial conditions at some downstream distance, influenced by Reynolds number. However, the initial increase in the mass fraction fluctuation intensity in the near field occurs more rapidly in lower density gas, helium compared to air.

4.5.3 Asymmetry effect

For 3D jets, flow separation of the emerging gas originating from inside the tube, similar to flow over a backward step, is always observed at the entrance of orifice. This phenomenon was also previously reported in vertical 3D jets [107]. This flow separation contributes to the velocity and scalar deficit near the edge of the orifice located on the lower side of the jet (in the $+n$ direction), and results in a slight contraction in the width of the jet has been observed in both velocity and concentration field (Figs. 4.5b & 4.6b) in the range of $1D < x < 4D$. Asymmetry structure was always observed for all 3D jet, owing to flow separation and associated deficits in velocity and scalar field. This asymmetry pattern is clearly evident in the lower side of the jet centrelines (in the $+n$ direction), where more velocity and mass fraction spreading is exhibited near the tail ends of the radial profiles, $1 < (n/L_{1/2})$ for $x \leq 5D$ (Fig. 4.7). This asymmetry pattern and three-dimensionality nature of the 3D jets, encouraged more entrainment which lead to enhanced turbulent mixing in the 3D jets compared to the axisymmetry jets. This enhancement is clearly observed, upon comparison between the 3D and axisymmetry jets, in the velocity and mass fraction decays and spreading rates, and their pseudo-similarity solution presented in Figs. 4.5, 4.6 & 4.11, respectively.

Like 3D jets, non-circular jets are also well-known to entrain ambient fluid more effectively than their axisymmetry round jets counterparts [43]. The enhanced mixing in non-circular jet is associated with a higher degree of three-dimensionality in the coherent structure of the flow. As the jet spreads, deformation dynamics of asymmetric vortices yield a complex topology, which results in interaction of streamwise and azimuthal vortices and the associated energy transfer between them. This phenomena, "axis-switching", is the main fundamental mechanism for the enhanced entrainment properties of the non-circular jets, and it has been only reported in the non-circular jets [43, 75]. Generally, the axis-switching can be observed from cross passing the jet half-width profiles in the major and minor axis planes (s-n and s-y planes). This phenomenon also can be observed from the broad humps in axial development of the tangential turbulence intensity along the jet centrelines ($\boldsymbol{u}_{s(rms)}/\langle\boldsymbol{u}_c\rangle$) as concluded in comparative experimental study on the non-circular jets [75]. In Fig. 4.8a, while no humps occurs in the variation of ($\boldsymbol{u}_{s(rms)}/\langle\boldsymbol{u}_c\rangle$) for the round OP or pipe jets, humps are present for the round 3D jets. This can be correlated with axis-switching phenomenon, and as a result of enhanced entrainment, increase in centreline velocity decay which is result into a higher values of ($\boldsymbol{u}_{s(rms)}/\langle\boldsymbol{u}_c\rangle$). This phenomenon is in fact observed in the recent study on vertical 3D jet [107], where the air jet half-width profiles cross-pass at approximately $15D$ from the orifice. Therefore, axis-switching would be one of the main underlaying phenomena responsible for enhanced turbulent mixing and entrainment of the 3D jets.

4.6 Conclusions

In this study, simultaneous velocity and concentration measurements were conducted in order to investigate horizontal turbulent jets, of varying gas densities and Reynolds numbers, issuing from a round orifice machined on the side of a round tube. The fluids considered were air and helium. The results were compared to previous studies of vertical jet, issuing from the same pipeline geometry and axisymmetric round OP jets [107]. Comparisons were also made with horizontal axisymmetric round jets, issuing through flat plates [4], and the results of other relevant experimental studies of constant and variable density turbulent axisymmetry jets.

By considering flow emerging through a hole located on the side of a tube wall, it was found that the flow arrangement caused a significant deflection from the axis normal to the orifice. This characteristic was also previously observed in vertical jets of the similar pipeline configuration [107]. In the current investigation, the helium jet deflection was found to be initially governed by the density of the gas in the near field, and it experienced further deflection due to buoyancy in the far field. The buoyancy-caused deviation in the far field was found to be well reproduced by a power law expression with the exponent ~ 1.3. In contrast, it was found that such buoyancy effects were not present in axisymmetric round jet helium experiments, where the jet issued through flat-plates, with the same Froude number. This observation suggests that the realistic leak geometry along the pipeline orientation considered in this study causes buoyancy effects to dominate much closer to the orifice than expected for axisymmetric round jets. Furthermore, it was found that buoyancy effects have a negligible impact on the decay of jet velocity and spreading rates. This implication is also true for fluctuation quantities, where buoyancy was found to not have a significant effect on centreline velocity fluctuation intensities. Nevertheless, higher centreline mass fraction fluctuation intensities ($\sim 33\%$) for the horizontal 3D jets compared to the vertical cases ($\sim 26\%$), may have been caused by buoyancy effect.

Owing to asymmetry flow structure and three-dimension nature of 3D jets, enhanced turbulent mixing was always observed in 3D jets compared to axisymmetry jets. This enhanced mixing and entrainment caused the reduction in the potential-core length, as well as increases in the decay and spreading rates of both velocity and concentration. Despite the fact that the orifice geometry is round, the axis-switching phenomenon was observed in 3D jets, and is believed to be one of the main fundamental mechanisms for the enhanced entrainment properties of the 3D jets. Furthermore, the 3D jets obey the pseudo-similarity decay law with the scaling indicated by the effective diameter. The mass fraction decay along the centreline scaled well with the original effective diameter term ($D_{ef} = D(\frac{\rho_j}{\rho_\infty})^{\frac{1}{2}}$), while the modified version of the effective diameter ($D^*_{ef} = D(\frac{\rho_j}{\rho_\infty})^{0.3}$) provided a more accurate velocity decay profile. Finally, it was shown that the turbulent velocity and scalar properties are dependent on the initial jet conditions for all regions of the flow field. Therefore, caution is required when using round axisymmetry jet assumptions to correlate the correct dispersion, velocity and concentration decay rates and, consequently, the extent of flammability envelope of a jet emitted from realistic leak geometries.

Chapter 5

Multi-Component High Aspect Ratio Turbulent Jets Issuing from Non-Planar Nozzles [1]

[1]The body of this chapter was submitted for publication in Majid Soleimani nia, Peter Oshkai and Ned Djilali, International Journal of Hydrogen Energy. MS designed the study and experimental system, conducted the measurements, performed the analysis, drafted the initial manuscript, and finalized the submitted version. PO and ND contributed to design of initial study as well as refinement of further manuscript drafts.

5.1 Preamble

Simultaneous particle image velocimetry (PIV) and planar laser-induced fluorescence (PLIF) techniques were employed to experimentally investigate the dispersion of turbulent jets issuing from high-aspect-ratio slots on the side wall of a circular tube. Two slots with an aspect ratio of 10 were considered in this study, although their configuration was aligned parallel to and perpendicular with the direction of the flow inside the tube. The effects of buoyancy and asymmetry on the resulting flow structure were studied in both vertical and horizontal orientations, and over a range of Reynolds numbers and gas densities. Significant differences were found between the centreline trajectory, spreading rate, velocity and concentration decays of current realistic jets with those of the conventional elliptical and rectangular slot jets issuing through flat surfaces. These realistic pipeline leak-representative jets were found to deflect along the jet streamwise axis. It was found that increases in aspect ratio caused a reduction in the angle of deflection, jet centreline decay rates and the width growth on both velocity and scalar fields compared to its 3D round jet counterpart, most notably in the far field.

5.2 Introduction

Non-circular jets are found in a wide range of applications in nature and engineering systems. These jets have higher entrainment rates than their axisymmetry round jet counterparts, and as a result, more effective mixing occurs [43]. The enhanced mixing is believed to be associated with the higher degree of three-dimensionality in the coherent structures of the flow, which is attributed either to the non-uniform curvature of the nozzle perimeter, or to the instabilities originating at the sharp perimeter of the nozzle. The three-dimensionality, which is highly sensitive to the initial conditions, becomes the main characteristic of non-circular jet flows, with the asymmetrical streamwise and azimuthal vorticity playing the main role in entraining ambient fluid. As the jet spreads, dynamic deformation of the asymmetric vortices yields a complex topology, with interaction of streamwise and azimuthal vortices and energy transfer between them. This "axis-switching" phenomenon has been observed in the evolution of non-circular jets [43, 75], whose cross-section can frequently develop into shapes similar to those of the origin nozzle but with axes sequentially rotated at angles characteristic of the nozzle geometry.

Among non-circular jet flows, plane jets received extensive investigation in the last couple of decades due to their two-dimensional characteristics, which made measurement and numerical simulations along with statistical analyses much easier [30, 42, 22, 23]. It was found that initial conditions organized coherent structures in the near field but their effects were also noticed in the self-similar far field region of the plane jet. It was observed that an increase in the Reynold number (Re), resulted in shortening the potential core length and increased the near field velocity spreading rate, while the far field rates of mean velocity decay and spread showed the reverse dependency, and decreased with increasing the Re [23].

Non-circular three-dimensional jets (i.e. rectangular, elliptic, triangle, and other nozzle shapes) have been studied extensively, both through experiments [44, 91, 136, 75] and numerical simulations [78, 115, 40]. In general, due to the three-dimensional nature of the jet's initial configuration, the near-field decay rates of the mean velocity and turbulence intensity are much greater compared to the axisymmetric jet. In the near field, jets that experience the axis-switching phenomenon exhibited a higher decay rate of the centreline velocity. Regardless of the nozzle shape, a change in the nozzle type (sharp-edged orifice plate (OP) and smooth contraction (SC)), results in shorter potential core length in OP jets compared to SC jets but the nozzle type does not affect the far-field centreline velocity decay rate [75, 90, 43]. Like other jet flows, the development of non-circular jets is significantly influenced by the jet initial conditions, even in the self-similar far field region. Previous studies of rectangular and elliptic jets found that the distance from the orifice, where axis-switching occurs, increases with the nozzle aspect ratio [55, 91]. Mixing in the near field is also enhanced with increasing the nozzle aspect ratio [91].

It is noteworthy that all aforementioned studies on non-circular jets have been limited to the jet flow emerging through flat surfaces, where the direction of the jet mean flow was aligned with the flow origin. However, in practical engineering applications (i.e. pipe lines or storage facilities), any accidental gas leakage would not be limited to flows through flat surfaces, and leaks through cracks in the side walls of circular pipes or storage tanks should also receive attention. The common belief was that within sufficient distance from the nozzle, non-circular jet evolution follows that of a round axisymmetry jet, only a few studies on high-aspect-ratio jet have proven that this assumption is not necessarily correct. These limited studies [73, 125], investigated the effects of the orifice shape and gas pressure on gas dispersion behavior from a failed flange joint, by the means of flow visualization and pressure measurements along the jet centreline. These effects persisted to distances up to 250 slot widths away from the orifice, and the centreline velocity decay rate could not be approximated by a round axisymmetry jet assumption. To explore the realistic gas leakage from a curved surface in more detail, recent studies investigated vertical and horizontal buoyant jet evolutions through round holes from curved surfaces, numerically and experimentally [107, 105, 72, 106, 108]. Through these recent studies, significant discrepancies were found between the evolution of axisymmetric round sharp-edged orifice plate (OP) jets through flat surfaces and those originating from curved surfaces. Most notably, jet deflection from the jet axis, and asymmetric dispersion patterns were always observed. Also, in horizontal jets, buoyancy effects were dominated much sooner than expected in axisymmetric round jets. To our knowledge, however, the dispersion of high-aspect-ratio jets from curved surfaces have not yet been investigated, by the means of simultaneous velocity and scalar measurements.

To investigate the effects of asymmetry and buoyancy on the evolution of high-aspect-ratio jets issuing from realistic pipeline geometries, jet release experiments were conducted with air and helium. Flow patterns and dispersion of gas through a curved surface originated from a source whose original velocity components were nearly perpendicular to the direction of the ensuing jets were studies. From now on, this jet configuration is referred as a 3D jet. Two slots with the same aspect ratio ($AR = 10$) as possible crack geometries were considered in this study, although their configuration was aligned in parallel to and perpendicular with the direction of flow inside the tube. These realistic high-aspect-ratio 3D jets were also compared to their 3D round jet counterparts as well as high-aspect-ratio jets issuing through flat surfaces. Particle imaging velocimetry (PIV) and planar laser-induced fluorescence (PLIF) were simultaneously used to measure high-resolution instantaneous velocity and concentration fields, respectively. The purpose of this investigation was to identify and characterize departures from non-circular jets emerging through flat surfaces, and to highlight the effects of initial conditions, buoyancy and the asymmetric nature of the 3D jets, which ensued from a practical geometry arrangement.

5.3 Experimental system and techniques

Figure 5.1 illustrates the orifice geometries along with the evolution of the jet flow from the orifices considered in this study, for both air and helium. Two high-aspect-ratio slots, with the same aspect ratio ($AR = 10$), were machined into the side of a

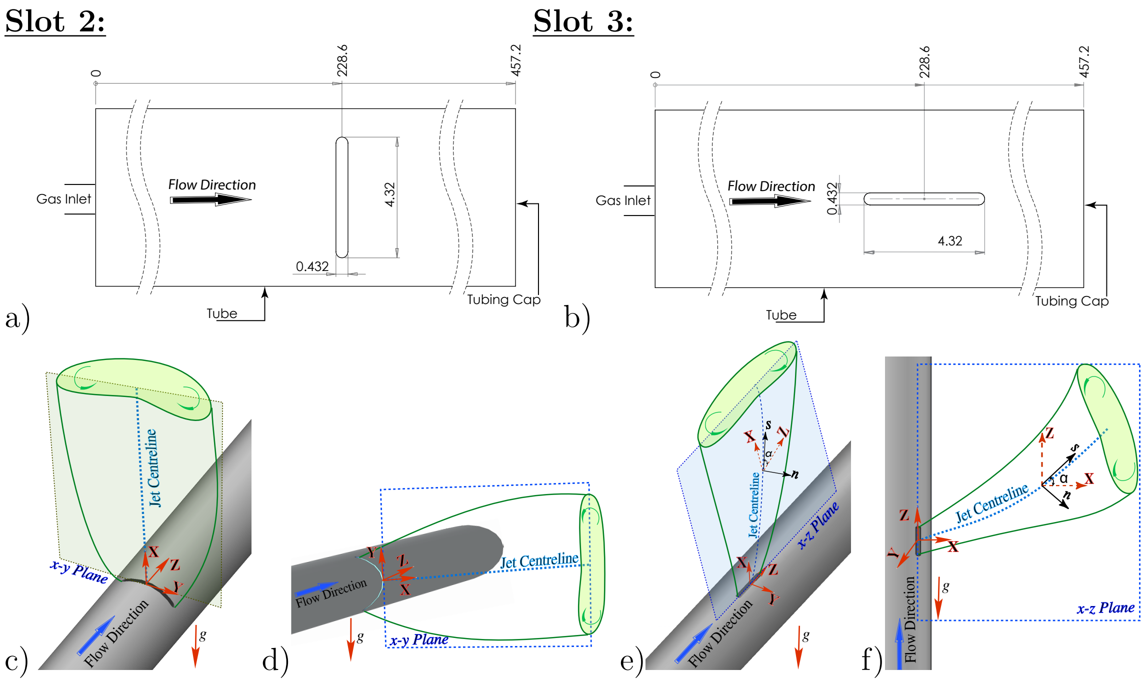

Figure 5.1: a-b) Schematic of slot 2 and 3 geometries. c-f) schematic of vertical (c & e) and horizontal (d & f) 3D slot jets flow measurement areas. All dimensions are in mm.

round tube (closed at one end) with an outer diameter of 6.36 mm and 0.82 mm wall thickness. Aspect ratio is defined as the ratio of the two symmetrical (long/short) axes of the slot geometry. These high-aspect-ratio 3D slots were aligned parallel and perpendicular to the direction of the flow inside the tube, and also compared to their 3D round ($AR = 1$) jet counterparts [107, 108]. Hereafter, slots 1, 2 and 3 refer to the round orifice, the slot perpendicular to, and the slot parallel with the direction of flow inside the tube, respectively. The new length-scale, equivalent diameter (D_{eq}), was defined to adequately characterize the jet flow [55]. Here, D_{eq}, is the diameter of an equivalent circle with the same area of the nozzle. Due to the curvature of the tube surface, and also to keep AR identical for both slots ($AR = 10$), slightly different equivalent diameters (D_{eq}) were obtained for the slots. The range of D_{eq} for the current study are 2, 1.6 and 1.53 mm for the slots 1, 2 and 3, respectively. To capture development of the jet, measurements were obtained on the two-dimensional planes aligned with the major axis of the slots. Here, the two-dimensional measurements planes are denoted as x-y and x-z (as indicated in Figs. 5.1 c-f), for the slots 2 and 3, respectively. Also shown in the figure is the jet centreline, which acts as a reference from which measurements are later obtained. Owing to potential deviation of the jet

Table 5.1: Flow properties of 3D jet experiments

Slot	Jet	Orien-tation	AR	D_{eq} [m]	Q [L/min]	$\langle \boldsymbol{u}_j \rangle_c$ [m/s]	ρ_j [Kg/m^3]	ν_j [m^2/s]	M [N/m]	Fr	Re_δ
1	Air	H	1	2×10^{-3}	15	147.5	1.17	1.54×10^{-5}	50.9	-	19,000
1	Air	V	1	2×10^{-3}	15	147.5	1.17	1.54×10^{-5}	50.9	-	19,000
2	Air	H	10	1.6×10^{-3}	15	169.7	1.17	1.54×10^{-5}	51.7	-	20,300
2	Air	V	10	1.6×10^{-3}	15	170.2	1.17	1.54×10^{-5}	51.8	-	20,300
3	Air	H	10	1.53×10^{-3}	15	209.2	1.17	1.54×10^{-5}	53.3	-	21,000
3	Air	V	10	1.53×10^{-3}	15	208.6	1.17	1.54×10^{-5}	53.2	-	21,000
1	He	H	1	2×10^{-3}	35	399.5	0.165	1.21×10^{-4}	51.3	1.34×10^6	51,500
1	He	V	1	2×10^{-3}	35	399.7	0.165	1.21×10^{-4}	51.4	1.34×10^6	51,500
2	He	H	10	1.6×10^{-3}	35	468.8	0.165	1.21×10^{-4}	52.2	2.4×10^6	50,800
2	He	V	10	1.6×10^{-3}	35	469.1	0.165	1.21×10^{-4}	52.3	2.4×10^6	50,800
3	He	H	10	1.53×10^{-3}	35	511.4	0.165	1.21×10^{-4}	52.9	2.8×10^6	51,600
3	He	V	10	1.53×10^{-3}	35	510.7	0.165	1.21×10^{-4}	52.7	2.8×10^6	51,600

(slot 3) from the orifice axis (x-axis), the jet centreline tangent and normal lines are shown as s and n coordinates in the figure, respectively. It should be noted that the jet centreline, for slot 2, is considered at geometrical centre of the orifice ($y = 0$) in the x-y measurement plane.

The experiments were conducted in a controlled stagnant environment, at room temperature and pressure ($T_o \sim 22^{\mathrm{oC}}$, $p_o \sim 100$ kPa). Flow controllers (Bronkhorst, EL-FLOW series) were used to control mass flow rates of dry air and pure scientific grade helium to the system, with a high accuracy (standard $\pm 0.5\%$ of reading plus $\pm 0.1\%$ full scale) and precision (within 0.2% of the reading). After the test gas was mixed and seeded with the PIV and PLIF tracer particles, gas flow entered the test section of the tube. Isothermal and isobaric conditions were ensured in all measurements. Further specific details of the flow facility used in the current experiments can be found in [107, 108]. The orifice, through which the gas dispersed, was located sufficiently downstream along the tube length to ensure fully developed flow inside the tube at the orifice location. Within the tube, flow controllers were used to ensure fully developed subsonic and turbulent flow inside the tube.

In order to compare the behaviour of both test gases, for each experimental setup, the averaged momentum flux (M) at the jet exit was estimated and matched for all slot 1 cases. This matching was achieved, iteratively, by varying the volumetric flow rate (Q) in the system, after which time, the same Q was considered for both slots 2 and 3 experiments. Here, M was calculated by first obtaining the time-averaged jet exit velocity from two-dimensional PIV measurements. The two-dimensional momentum flux, in units of [N/m], was then calculated from

$$M = \int_{-D/2}^{D/2} \rho_j \langle \boldsymbol{u}(r) \rangle^2 \, \mathrm{d}r \tag{5.1}$$

where the subscript 'j' refers to the conditions at the nozzle, the angle brackets '$\langle$ $\rangle$' refers to the time-averaged quantity, and also ρ and r refer to density and radius, respectively. Table 5.1 shows the flow properties used in this study, for both the horizontal and vertical high-aspect-ratio 3D jet configurations (Slot 2 & 3), as well as vertical and horizontal 3D round jets (Slot 1) which have been used for comparison [107, 108]. Here, the subscript 'c' refers to the conditions at the jet centreline, Fr is the Froude number, and H & V refer to horizontal and vertical orientations, respectively. In all cases, the jets were characterized by the outer-scale Reynolds number, $Re_\delta = \langle \boldsymbol{u}_j \rangle \delta / \nu_\infty$. Where, ν_∞ is the ambient fluid kinematic viscosity and δ is the width of the mean axial velocity profile, evaluated from limits of 5% of the centreline velocity at $x \simeq 0$.

Particle imaging velocimetry (PIV) was used to capture the two-dimensional velocity flow field information. A dual-head Nd: YAG pulsed laser (New Wave's SOLO III 15 HZ) was used to illuminate a two-dimensional cross-section of the flow, which was seeded with Di-Ethyl-Hexyl-Sebacate (DEHS), with a typical diameter of less than 1 μm, which acted as a tracer particle. The light sheet had an approximate height of 5 cm and a thickness of 1 mm. The camera's field of view (PIV CCD) was a 40×30 mm^2 window with an approximate pixel size of 6.5 μm in physical space. This resolution was estimated to be comparable to the finest scale of the flow, with respect to the Nyquist criterion [110]. Each pair of images were then processed using LaVision DaVis 8.4 software to calculate the global instantaneous flow velocity field. Following the PIV uncertainty propagation method[99], conservative uncertainty was estimated as 3% and 6% in the time-averaged velocity and Reynolds shear stress profiles, respectively.

To measure the gas concentration, we applied planar laser-induced fluorescence (PLIF). To simultaneously apply PLIF with PIV, the flow was also seeded with acetone vapour at consistent rate of $\sim$ 1% by mass fraction. A Pulsed Nd: YAG laser (Spectra-Physics INDI-40-10-HG) was used in order to excite the acetone molecules in a light sheet with an approximate height of 5 cm and a thickness of 350 μm, which was then recorded with a PLIF CCD camera. The camera's field of view for all cases corresponded to a 38×28 mm^2 window with an approximate pixel size of 6.5 μm. The images were taken at a frequency of 5 Hz and then processed using LaVision DaVis 8.4 software. After correcting for errors associated with background noise, fluctuations in cross-sectional laser beam intensity, and laser energy per pulse deviations, one can assume the remaining non-uniformity of the scalar field is due to signal to noise ratio (S/N). The error in the S/N can be estimated using the standard deviation of this ratio in a uniform low signal region of the flow field. Based on this data, and the uncertainty propagation method, the uncertainty in the time-averaged and variances of the concentration field was estimated as conservative values of 4% and 7%, respectively. For each experimental case, a total of 500 images were acquired to determine the time-averaged molar concentration ($\langle X \rangle$) and variances (X'^2). Further details of the experimental procedure can be found in [107, 108].

Finally, to retain the spatial resolution of the flow field, the full measurement region is covered by up to four individual imaging windows (depends on the slot geometry and jet orientation) with at least a 20% overlap between each window. Figure 5.2 shows an example of the instantaneous velocity and concentration fields, for helium slots 2 and 3 in the x-y and x-z planes, respectively. It should be noted that the flow fields were constructed from up to three different experiments, where individual imaging windows have been stitched together.

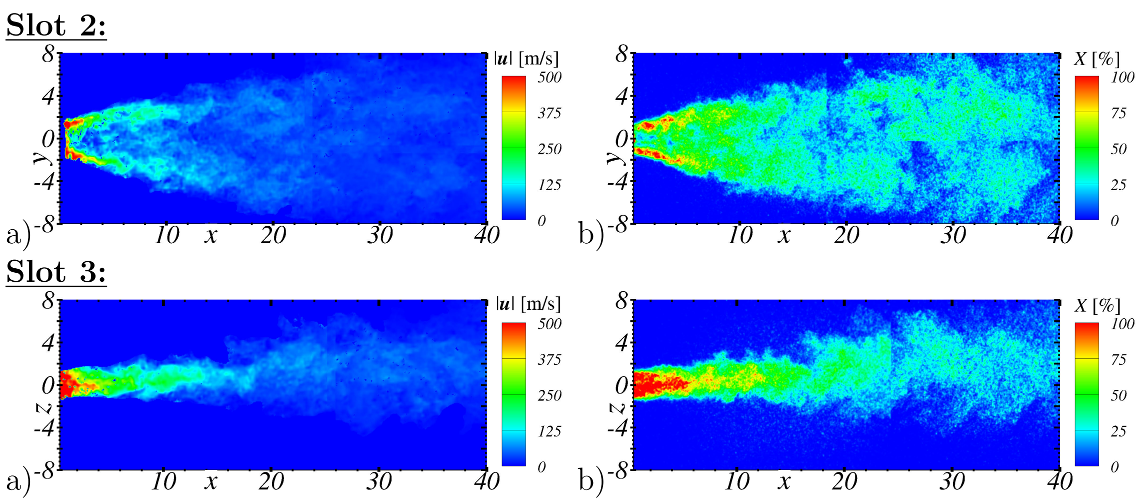

Figure 5.2: Instantaneous a) velocity and b) molar concentration fields obtained from Helium
3D slot 2 & 3 in x-y and x-z planes, respectively.

Distances reported here have been normalized such that

$$x = \frac{\mathbf{X}}{D_{eq}}, \qquad y = \frac{\mathbf{Y}}{D_{eq}}, \qquad z = \frac{\mathbf{Z}}{D_{eq}}, \qquad s = \frac{\mathbf{s}}{D_{eq}}, \qquad n = \frac{\mathbf{n}}{D_{eq}} \tag{5.2}$$

where D_{eq}, the equivalent diameter of the orifice, is taken as a reference length scale.

5.4 Results

5.4.1 Time-averaged flow fields

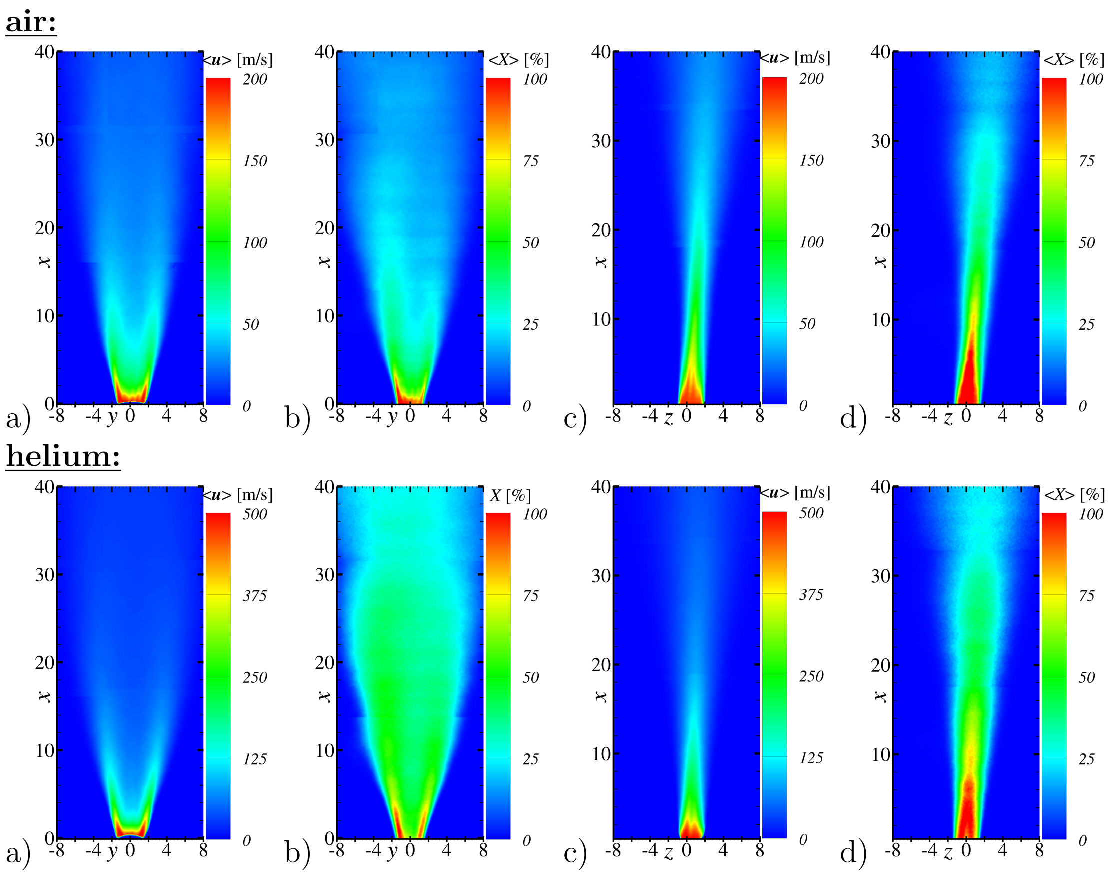

Figure 5.3: Time-averaged velocity and molar concentration contours from vertical high-aspect-ratio slot jet on side of tube (3D slot jet) for air and helium, obtained from a) slot 2 velocity contours in x-y plane, b) slot 2 molar concentration contours in x-y plane, c) slot 3 velocity contours in x-z plane and d) slot 3 molar concentration contours in x-z plane.

The time-averaged velocity and molar concentration contours obtained for all

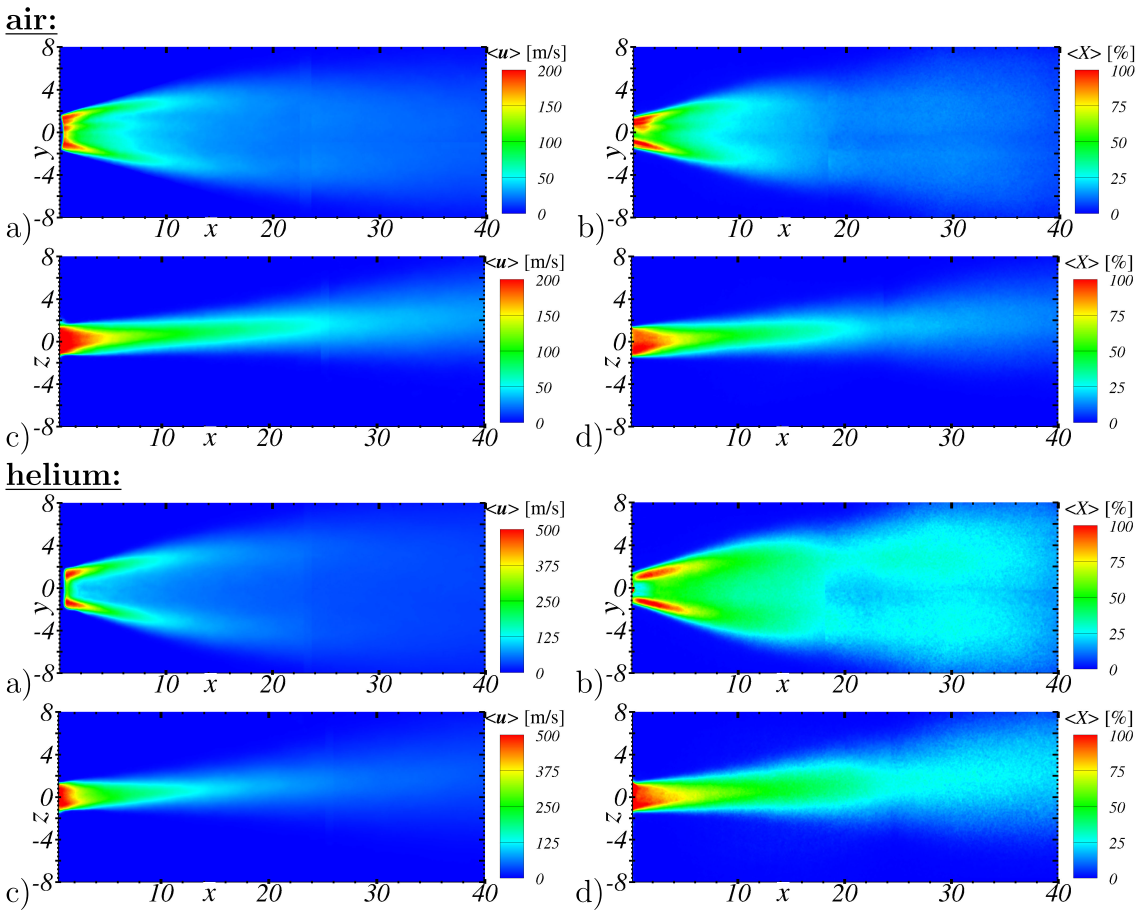

Figure 5.4: Time-averaged velocity and molar concentration contours from horizontal high-aspect-ratio slot jet on side of tube (3D slot jet) for air and helium, obtained from a) slot 2 velocity contours in x-y plane, b) slot 2 molar concentration contours in x-y plane, c) slot 3 velocity contours in x-z plane and d) slot 3 molar concentration contours in x-z plane.

vertical and horizontal 3D slot jet experiments are shown in Figs. 5.3 and 5.4, respectively. In vertical slot 2 for both gases, there were two high-velocity peaks (saddle-back behaviour), at about $y \pm 1.5D_{eq}$, on each side of the x-axis toward the edge of the jet. Slightly shorter potential-core length was observed for helium ($\simeq 2D_{eq}$), compared to air ($\simeq 3D_{eq}$). This saddle-back behaviour was previously found to originate from a velocity deficit region which forms inside the orifice due to flow separation as the gas inside the tube encounters the edge of the 3D round orifice [107]. However, another possible reason is the sharp edge of the slot along with the curvature of the tube [76]. The initial saddle-back profile and shorter potential core length for helium compared to air, were also observed in both air and helium horizontal slots 2, presented in Fig.

5.4 a.

For all vertical and horizontal slot 3 experiments, air and helium jets were found to deviate from the jet streamwise axis (x-axis), in the direction of the initial flow inside the tube. There was also a shorter potential-core length for helium ($\simeq 3D_{eq}$), compared to air ($\simeq 4D_{eq}$). Additionally, near the potential-core region, there was slightly more jet spreading on the positive n-coordinate of the jet centre compared to the opposite side. It should be noted that the n-coordinate refers to lines which are normal to the centreline, aligned with the opposite direction of flow inside the tube, and coplanar with the x-z plane (see the coordinate system in Fig.5.1 e-f). The spreading rate in the opposite direction of the flow within the tube, near the potential-core region, was previously found to be higher in the 3D round jets (Slot 1) [107, 108] compared to the slot 2 and slot 3 geometries of the current investigation.

In general, concentration profiles were qualitatively similar to the velocity profiles presented in Figs. 5.3 - 5.4, with two exceptions. First, the potential core lengths in the vertical slot 3 jets were approximately $\simeq 12D_{eq}$ and $\simeq 11D_{eq}$, for air and helium, respectively; in contrast, the potential core lengths in the horizontal slot 3 jets were approximately $\simeq 5D_{eq}$ for both gases. Also for both horizontal and vertical experiments, much higher concentration levels and higher spreading rates were observed for helium in the far field compared to air.

5.4.2 The jet centreline trajectory

In Fig. 5.5, the jet centreline trajectories, obtained in the x-z plane, are presented for all slot 3 jets. Here, the trajectories were determined by the maximum velocity magnitude, $|\langle \boldsymbol{u} \rangle|_{\max}(x)$ locations. Also shown for comparison are the jet centreline trajectories obtained in the far field (beyond $x \geq 10D_{eq}$) from previous vertical and horizontal slot 1 jet experiments [107, 108]. In general, the centrelines obtained from slot 3 experiments followed a nearly linear upward trajectory, in the direction of flow within the tube, after the potential core lengths of $x \sim 3D_{eq}$ for helium and $x \sim 4D_{eq}$ for air. Around $x \sim 17D_{eq}$ for helium, and $x \sim 25D_{eq}$ for air, a sudden change in the jet trajectory was observed. These locations coincided with the extent of the potential-core regions as shown in Figs. 5.3 - 5.4. In order to determine the effect of buoyancy on the horizontal slot 3 jets after these locations, lines of best fit, using linear regression to power law expressions were presented for the far field and are also shown in Fig. 5.5. Upon comparison of the centreline trajectories of air to

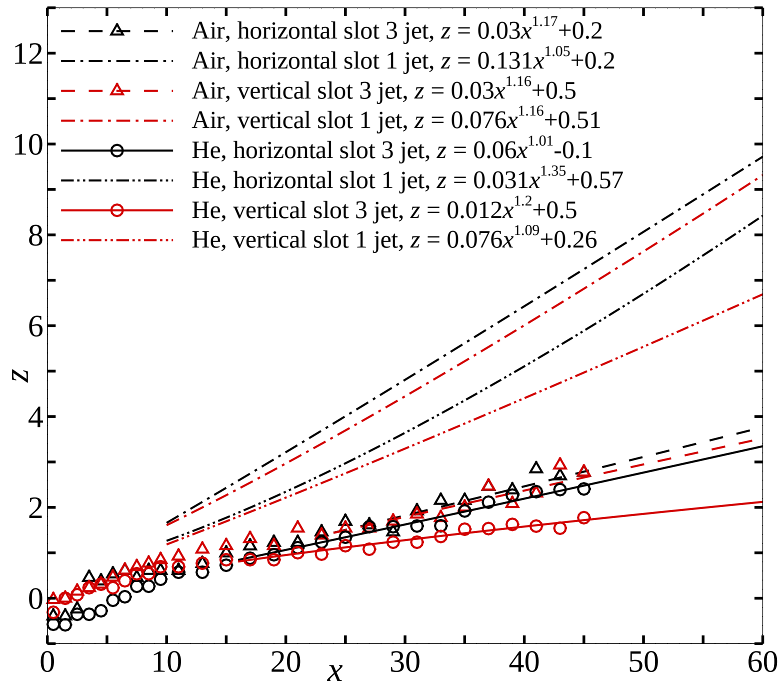

Figure 5.5: Jet centrelines taken along the location of maximum velocity magnitudes ($|\langle \boldsymbol{u} \rangle|_{\max}(x)$) in x-z plane from slot 3 measurements. Also shown, for comparison are vertical and horizontal 3D slot 1 jets experiments [107, 108].

helium, for both vertical and horizontal jets, it became clear that the buoyancy of the helium jet caused significant deflection from the horizontal axis, despite the high Froude number ($Fr = 2.8 \times 10^6$). While such buoyancy effects were not observed in the vertical and horizontal air experiments, jet centreline trajectories were almost parallel to each other (even upon extrapolating the line of best fit to the far field, beyond the experimental data collected). In addition, air was found to deviate from the x-axis to a greater extent than helium, owing to its higher gas density and negligible buoyancy effect. The same remarks were previously observed for slot 1 jets [107, 108]. However, the jet trajectory for the horizontal helium slot 3 jet was found to be described by a nearly linear relation (i.e. power law exponent ~ 1), whereas the horizontal helium slot 1 jet was previously found to have a power law exponent ~ 1.3. Slot 1 jets experienced a significant upward deflection, in the direction of flow inside the tube, compared to slot 3 jets as shown in Fig. 5.5.

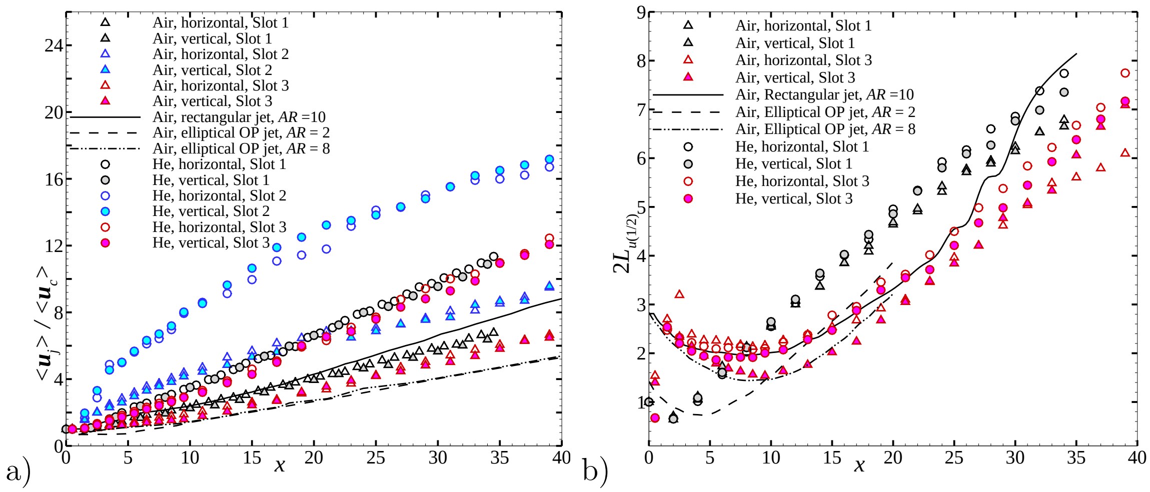

Figure 5.6: a) Inverse time-averaged velocity decay and b) jet velocity widths ($2L_{u(1/2)}$) obtained along the $|\langle \boldsymbol{u} \rangle|_{\max}(x)$ centrelines, in x-z plane from measurements. Note, n-coordinate refers to lines which are normal to the centreline, and coplanar with the x-z plane (see the coordinate system in Fig.5.1 e-f). Also shown, for comparison are vertical and horizontal 3D Slot 1 experiments [107, 108], vertical air sharp-edged rectangular and OP elliptical jet measurements [91, 55].

5.4.3 Velocity decay and jet spreading rates

Fig. 5.6 a) shows the inverse time-averaged velocity decay ($\langle \boldsymbol{u}_j \rangle / \langle \boldsymbol{u}_c \rangle$) along the jet centrelines (s-coordinate illustrated in Fig. 5.1 e-f) for all experiments. Here, the subscript 'c' refers to the conditions at the jet centreline, while the subscript 'j' refers to the jet exit condition. Also shown, for comparison, are velocity decay rates obtained from vertical and horizontal slot 1 experiments [107, 108], vertical air sharp-edged rectangular ($AR = 10$) [88] and OP elliptical jet ($AR = 2$ & 8) [55] measurements. Upon comparison of air slots 1 & 3 to the sharp-edged rectangular and OP elliptical jets, both horizontal and vertical slot 3 jets ($AR = 10$) show the same velocity decay rates to that of the OP elliptical jet with $AR = 8$ in the near field ($x < 10D_{eq}$). Within this range, a slightly higher decay rate was found for the centreline velocity of slot 3 jets compared to the OP elliptical jet with an $AR = 2$. Beyond this range, velocity decay rates for air slot 3 jets were found to be higher than both OP elliptical jets. Furthermore, both air slot 3 jets exhibited a lower velocity decay rate compared to the sharp-edged rectangular jet ($AR = 10$) within the entire domain. On the other hand, the horizontal and vertical slot 1 experiments ($AR = 1$) were found to exhibit almost the same velocity decay rate as that of the sharp-edged rectangular jet ($AR = 10$) up to $x \sim 17D_{eq}$, and after this point, the sharp-edged rectangular jet was found to have a slightly higher decay rate for the rest of the measurement's domain. In contrast, the velocity decay rates for the slot 1 jets were found to be higher than those of both OP elliptical jets within the entire domain. Comparison of the velocity decay rate of slot 3 jets with slot 1 jets [107, 108] revealed a slightly higher decay rate in slot 1 jets, with helium jet decaying faster than air jet. In general, upon comparison between horizontal and vertical 3D slot jets, buoyancy was not found to significantly affect the velocity decay rates.

Among all slot experiments, the highest velocity decay rate was observed for slot 2 cases. This was due to the geometrical centreline (along the y=0 in x-y plane) considered for this slot, where the measured velocity was essentially not the maximum value (see the initial saddle-back velocity profile observed in the time-averaged velocity contours in Figs. 5.3 - 5.4). Also, it should be noted that the fixed data acquisition plane for slot 2 cases (x-y plane) may not accurately acquire gas dispersion in the far field region, due to deflection of the jet from the streamwise axis (x -axis) in the x-z plane. While, three-dimensional velocity measurement is not currently available for slot 2 experiments, it would be impossible to point out the exact location of jet deflection from the data acquisition plane; one may visually conclude that the measurement plane has correctly acquired the jet dispersion up to $x \sim 15 - 20D_{eq}$ from the time-averaged velocity contours (Figs. 5.3 - 5.4). However, the slot 2 experiments data will be presented as qualitative results rather than quantitative data, more specifically in the far field ($x \geq 20D_{eq}$) where the result is not representative of the correct gas dispersion.

For slot 1 & 3 experiments in the x-z plane, Figure 5.6 b presents the jet velocity widths ($2L_{u(1/2)}$) obtained by determining the locations where $|\langle \boldsymbol{u} \rangle| = 0.5|\langle \boldsymbol{u} \rangle|_{\max}(x)$ along lines orthogonal to the jet centrelines. These orthogonal lines have been indicated previously as coordinate 'n' in Fig. 5.1 e-f. For the 3D jets, in slot 3 cases, a large peak was observed in the jet widths within $1D_{eq} < x < 2.5D_{eq}$ distances from the orifice, whereas in the slot 1 experiments a slight contraction has been observed from $1D_{eq} < x < 4D_{eq}$. Beyond this point for slot 3, the jet spreading rates were observed to experience a slight contraction up to $x \sim 15D_{eq}$. Where after this point, much greater spreading rates were observed in slot 1 compared to slot 3 jets for all cases. Moreover, from slot 3 experiments, the jet spreading rate was found to be comparable for both air and helium gases, with exception of vertical air slot 3 case. However, helium slot 3 jets exhibit higher spreading rates compared to air, in the far field (beyond $x \geq 15D$). This trend was slightly more clearer upon comparison of the horizontal slot 3 cases between helium and air. It should be noted that this remark is also evident in slot 1 cases, where a higher spreading rate is found in helium compared to air beyond $x \geq 13D$. Upon comparison of slot jets to rectangular [91] and OP elliptical [55] jets, the spreading rate for slot 1 was found to be much higher than others in the range of $8D_{eq} < x < 30D_{eq}$. Beyond this range, the sharp-edged rectangular jet exhibited a slightly higher spreading rate.

5.4.4 Scalar concentration decay and jet spreading rates

Figure 5.7a shows centreline evolution of the inverse time-averaged jet gas mass fraction, $\langle Y_j \rangle / \langle Y_c \rangle$, for both air and helium measurements. Here, the jet gas mass fractions were determined from the measured mole fractions through

$$Y = \frac{XW_j}{\overline{W}} \tag{5.3}$$

where X and W_j refer to the mole fraction and molecular weight of the jet gas, respectively, and $\overline{W}$ refers to the mean molecular weight of the local jet gas-ambient air mixture given by

$$\overline{W} = XW_j + (1 - X)W_{\text{air}} \tag{5.4}$$

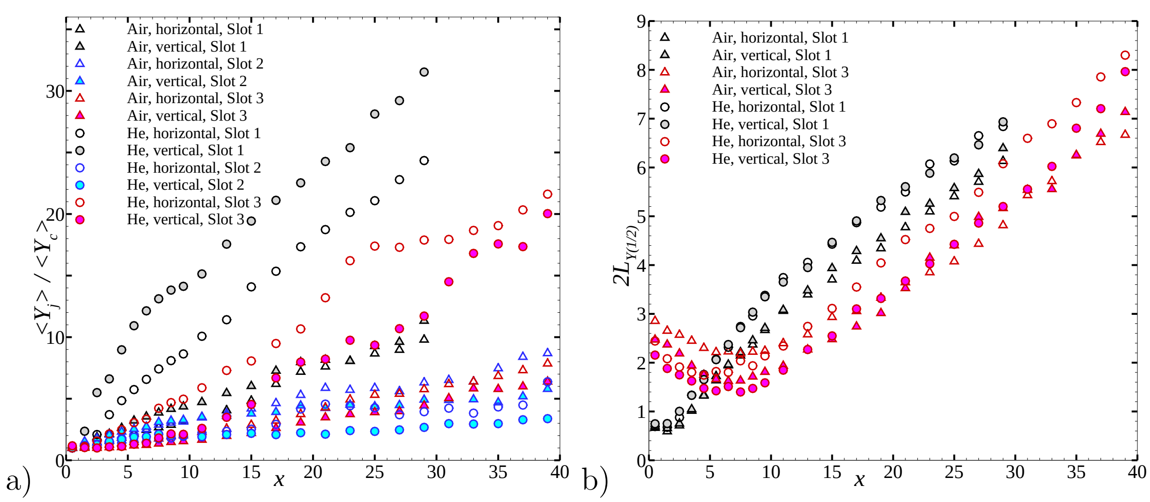

Figure 5.7: a) Inverse time-averaged jet gas mass fraction decay and b) mass fraction widths ($2L_{Y(1/2)}$) obtained along the $\langle Y \rangle_{\max}(x)$ centrelines, in x-z plane from measurements. Also shown, for comparison are vertical and horizontal 3D slot 1 jet experiments [107, 108].

Additionally shown for comparison, are the centreline mass fraction decay rates obtained from vertical and horizontal 3D slot 1 jet experiments [107, 108]. In general for all 3D slot jet cases, except the slot 2, helium jets were always observed to decay faster than air jets. It is noted, however, that the lowest decay rate observed in mass fraction for the helium slot 2 jets are likely due to the geometrical centreline ($y = 0$) where mass fraction obtained, and may not represent the location of jet centreline, as previously discussed in velocity decay profiles. Also, the centreline mass fraction decay rates observed in the experimental slot 1 jets were much faster compared to the slot 2 & 3 jets. Moreover, upon comparison of the helium slot 1 jets ($AR = 1$), the vertical orientation was found to have a faster mass fraction decay rate compared to the horizontal case. Such differences in behaviour was not observed for the air slot 1 jets, suggesting that buoyancy has a remarkable affect on the mass fraction decay rates [108]. On the other hand, for helium slot 3 experiments ($AR = 10$), a faster decay rate was observed for horizontal case compared to vertical orientation. Again, such remarks were not found to be valid for the air slot 1 jets, suggesting that the aspect ratio plays a more significant role on the mass fraction decay rates, compared to the buoyancy in the 3D high-aspect-ratio jets. Also, upon comparison to the velocity decay rates in Fig. 5.6a, it is noted that the jet centreline mass fraction decays faster than the velocity for helium, owing to the low Schmidt number ($Sc < 1$). This was also concluded in the recent experimental studies on the slot 1 jets [107, 108].

As was done for the velocity field, the jet widths based on the jet gas mass fraction ($2L_{Y(1/2)}$) have been obtained for slot jet experiments; these are presented in Fig. 5.7b. This was achieved by determining the locations where $\langle Y \rangle = 0.5 \langle Y \rangle_{\max}(x)$ along orthogonal lines to the jet centreline, in the x-z planes. Also shown, for comparison, are the jet widths based on the jet gas mass fraction obtained from vertical and horizontal slot 1 jet experiments [107, 108]. For all 3D jet cases, a slight contraction in the jet mass fraction widths were observed from $x < 4D_{eq}$ and $x < 15D_{eq}$ for slots 1 & 3, respectively, as was previously observed for the jet widths based on velocity. Beyond this point, the jet scalar growth rates, along n, were observed to be much greater in slot 1 compared to slot 3 jets for all cases. The helium jet also exhibited a faster spreading rate compared to air, in both horizontal and vertical cases.

Slot 2, vertical:

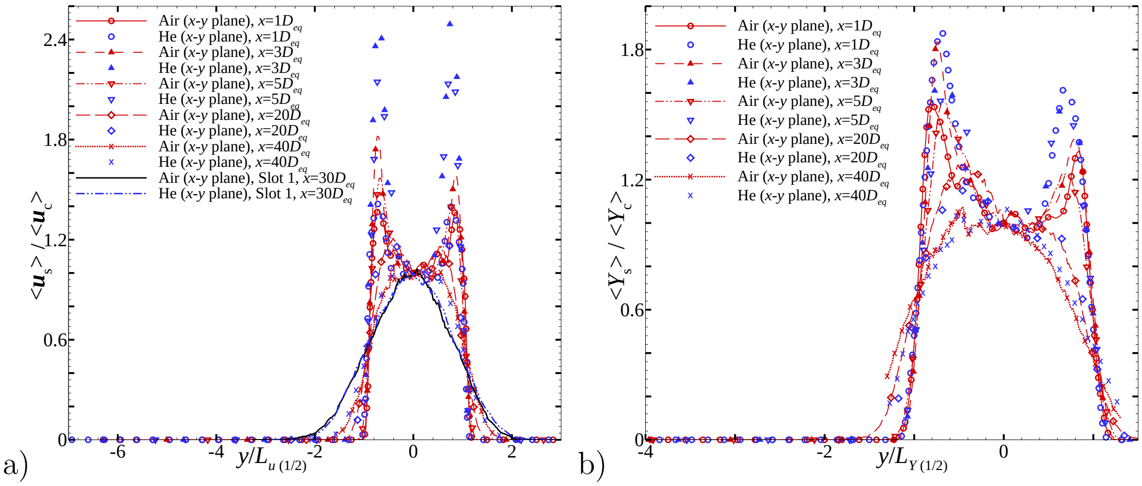

Slot 2, horizontal:

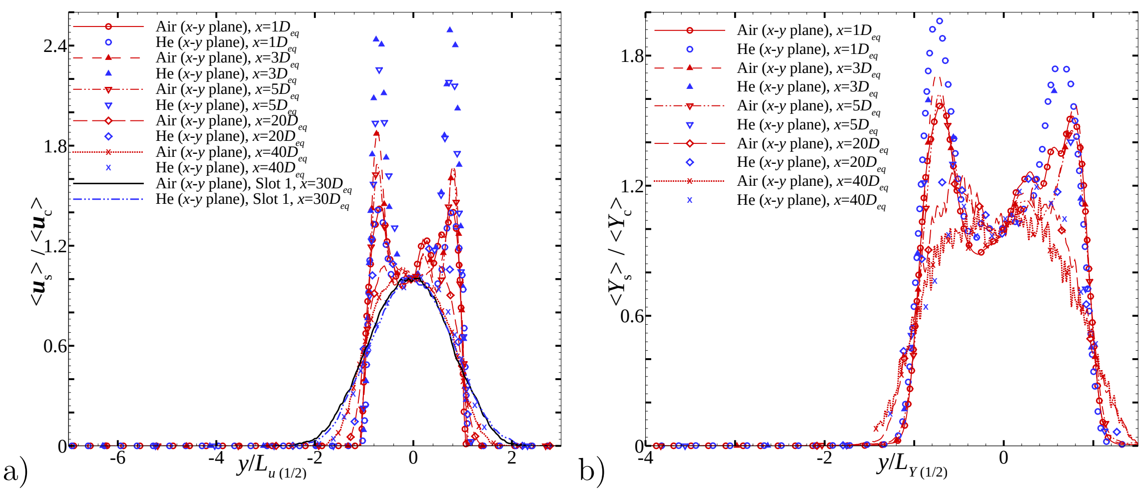

Figure 5.8: a) Normalized time-averaged velocity, and b) mass fraction profiles along jet centrelines ($y = 0$) in x-y plane, taken at various heights for both air and helium. Time-averaged velocity and mass fraction profiles are also compared to experimental vertical and horizontal 3D slot 1 jets [107, 108].

5.4.5 Jet centreline statistics

The normalized time-averaged velocity profiles for all slot 2 & 3 experiments are shown in Fig. 5.8a and Fig. 5.9a, respectively, along the y & n directions for several downstream locations along the jet centreline (s-curve Fig. 5.1). Also shown for comparison are the velocity statistics obtained for the vertical and horizontal slot 1 experiments [107, 108]. It should be noted that the s-component velocities presented here were normalized by the local centreline velocity magnitudes, $\langle \boldsymbol{u} \rangle_c(s)$. Also, the

Slot 3, vertical:

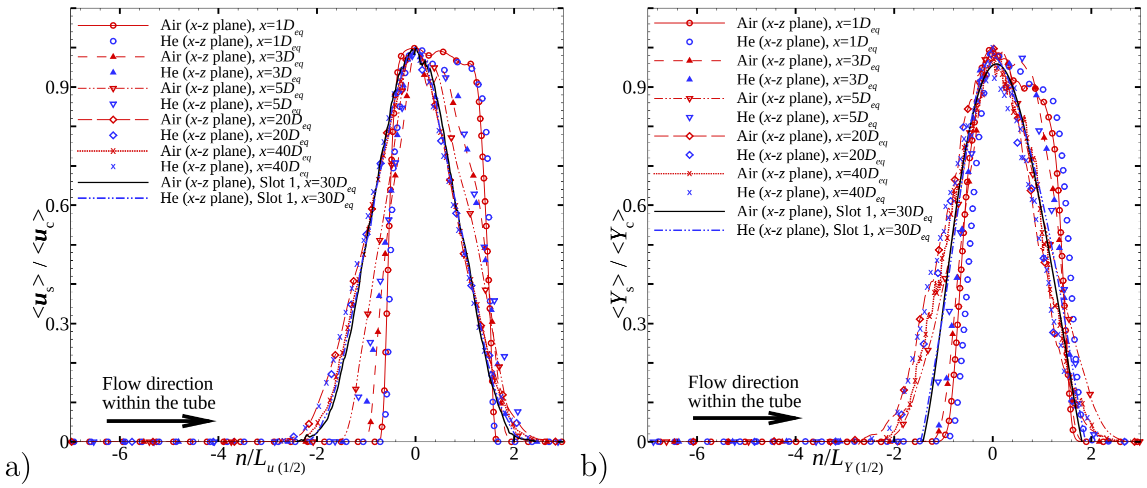

Slot 3, horizontal:

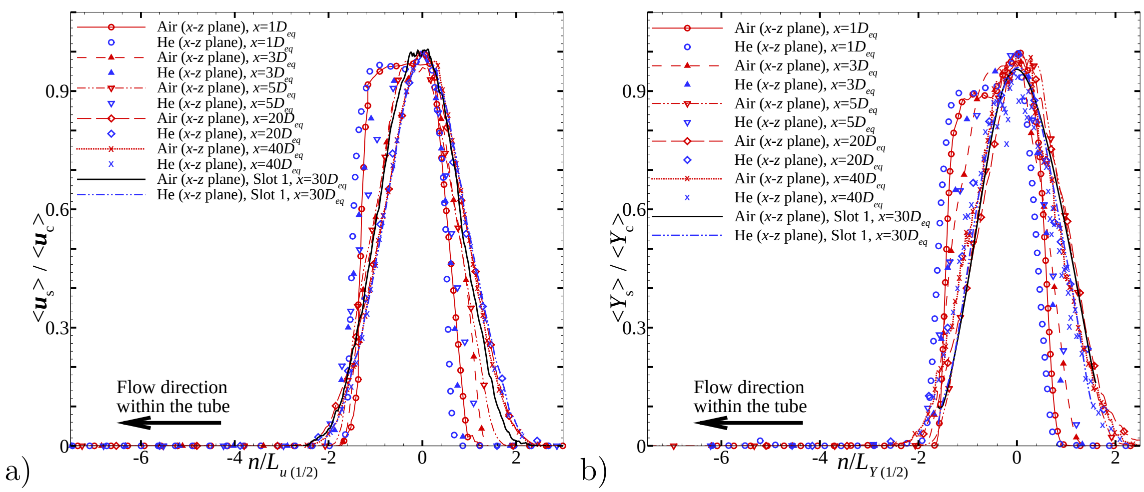

Figure 5.9: a) Normalized time-averaged velocity, and b) mass fraction profiles along jet centrelines in x-z plane, taken at various heights for both air and helium. Time-averaged velocity and mass fraction profiles are also compared to experimental vertical and horizontal 3D slot 1 jets [107, 108].

n-coordinate, which was normal to the centreline s-curve, was normalized by the jet velocity half widths ($L_{u(1/2)}$) determined from Fig. 5.6b.

For slot 2 in the x-y plane, in both orientations for air and helium experiments (Fig. 5.8a), the jets emerged from the slot with a saddle-back profile; higher humps exhibited in the helium cases compared to the air, located at $\sim (y/L_{1/2}) \pm 0.75$. This saddle-back profile was observed up to $x < 40D_{eq}$, and beyond this location, all slot 2 cases developed into a self-similar Gaussian-like distribution of velocity. Whereas in the slot 1 experiments, the velocity profiles were previously found to develop to the self-similar Gaussian distribution much closer to the orifice, beyond $x > 5D_{eq}$ [107, 108]. Finally, the curves obtained for both gases were found to be in agreement with each other in the far field region.

In the x-z plane of slot 3, in all cases (Fig. 5.9a), the jets emerged from the slot with an initial semi top-hat profile, not shown here. This behaviour was also previously observed in the slot 1 measurements [107, 108]. It should be noted that this semi top-hat profile was observed to deviate from the jet streamwise axis (x-axis) in the direction of flow inside the tube and was maintained up to $x \sim 5D_{eq}$ distance from the slot. In both orientations, air and helium experiments were found to exhibit slightly more velocity spreading to the lower side of the jet centre (in the direction of flow inside the tube) compared to the other side, with more velocity spreading was observed for helium compared to air. Beyond $x > 5D_{eq}$, in the far field, the experimental slot 3 jets developed into, and matched, the self-similar Gaussian distribution obtained from the slot 1 jets [107, 108]. Like the slot 2 experiments, the curves obtained for all gases were found to be in well agreement with each other in the far field.

The time-averaged mass fraction profiles for all slot 2 & 3 jet experiments are shown in Fig. 5.8b and Fig. 5.9b, respectively. Here, time-averaged mass fraction ($\langle Y \rangle$), have been normalized by the local centreline mass fraction, $\langle Y_c \rangle(s)$. The n and y coordinates were normalized by the jet mass fraction half widths ($L_{Y(1/2)}$) determined from the locations where $\langle Y/Y_c \rangle = 0.5$, Fig. 5.7b. In general, they were found to be qualitatively similar to the velocity profiles in all cases. For slot 2 in the x-y plane (Fig. 5.8b), the saddle-back profile with the sharp humps was observed at $\sim (y/L_{1/2}) \pm 0.75$; higher humps exhibited in the helium cases compared to the air within the range of $x < 5D_{eq}$ distance to the orifice. In all slot 2 cases, the saddle-back profile was developed into the self-similar Gaussian distribution beyond $x > 40D_{eq}$, same as velocity profiles. In the x-z plane (Fig. 5.9b), all slot 3 experiments exhibited initial top-hat mass fraction profile, with deviation from the jet streamwise axis (x-axis) in the direction of flow inside the tube. Where slightly more mass fraction spreading were found to exhibit to the lower side of the jet centre (in the direction of flow inside the tube), with more mass fraction spreading found for helium compared to air. In the far field, beyond $x > 5D_{eq}$, the mass fraction profile was found to develop quickly into the self-similar solution as observed in the slot 1 experiments [107, 108].

Fig. 5.10 shows the normalized axial evolution of the r.m.s. velocity fluctuation

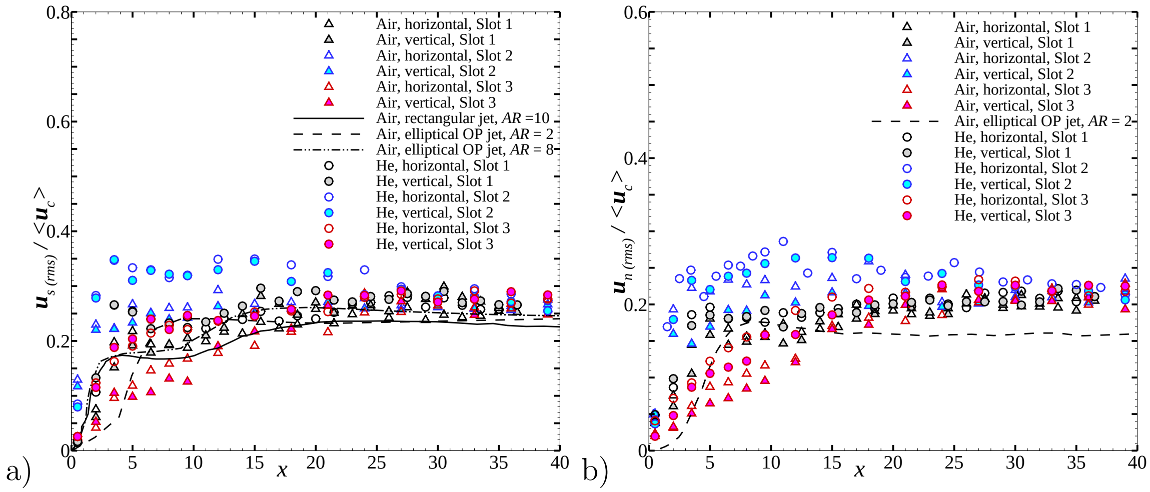

Figure 5.10: Axial development of turbulence intensities along jet centrelines, a) tangential turbulence intensity component ($\boldsymbol{u}_{s(rms)}/\langle \boldsymbol{u}_c \rangle$) and b) orthogonal turbulence intensity component ($\boldsymbol{u}_{n(rms)}/\langle \boldsymbol{u}_c \rangle$) for experiments. Also shown, for comparison are vertical and horizontal 3D Slot 1 experiments [107, 108], vertical air sharp-edged rectangular and OP elliptical jet measurements [91, 90, 55].

components in the s and n directions, tangential and orthogonal to jet centreline, where $\boldsymbol{u}_{(rms)} = \langle \boldsymbol{u}'^2 \rangle^{1/2}$. It should be noted that the prime ($'$) represents the instantaneous fluctuating quantity ($\boldsymbol{u}' = \boldsymbol{u} - \langle \boldsymbol{u} \rangle$). For helium vertical and horizontal slot 3 jets, the tangential turbulence intensity ($\boldsymbol{u}_{s(rms)}$) reached an asymptotic value of $\sim 26\%$ at $x = 15D_{eq}$, whereas such a value was not observed until $x = 25D_{eq}$ and $x = 20D_{eq}$ for air horizontal and vertical slot 3 jets, respectively. This trend was also observed in slot 1 measurements [107, 108] where helium reached the asymptotic value closer to the orifice, at $x = 3D$, compared to horizontal and vertical air at $x = 20D_{eq}$ and $x = 15D_{eq}$, respectively. However, it appears that this asymptotic value $\sim 26\%$ would be reached in the far field ($x > 33D$) for all slot jets. On the other hand, the vertical air sharp-edged rectangular [91] and OP elliptical jet [55] measurements reached the asymptotic values $\sim 23\%$ and $\sim 24\%$ in the far field, respectively. It should be noted that slightly lower turbulent intensities of the sharp-edged rectangular and OP elliptical jet, observed in both tangential and orthogonal components, are likely due to slightly higher initial turbulent intensities reported for those measurements (not shown)[74]. The same remark is valid for the orthogonal turbulence intensity, as helium slot 3 jets reached the asymptotic value $\sim 19 - 22\%$ more closer to orifice at $x = 17D_{eq}$, compared to air at $x = 27D_{eq}$. Also, the OP elliptical air jet reached the peak turbulence intensity ($\sim 18\%$) at $x = 8D_{eq}$ and then recovered the asymptotic value $\sim 16\%$ until $x = 15D_{eq}$ for the rest of the measurement domain [90]. In general, the intensity of tangential velocity fluctuations was higher than the orthogonal components, as observed in previous studies on 3D round & elliptical jets [107, 108, 90].

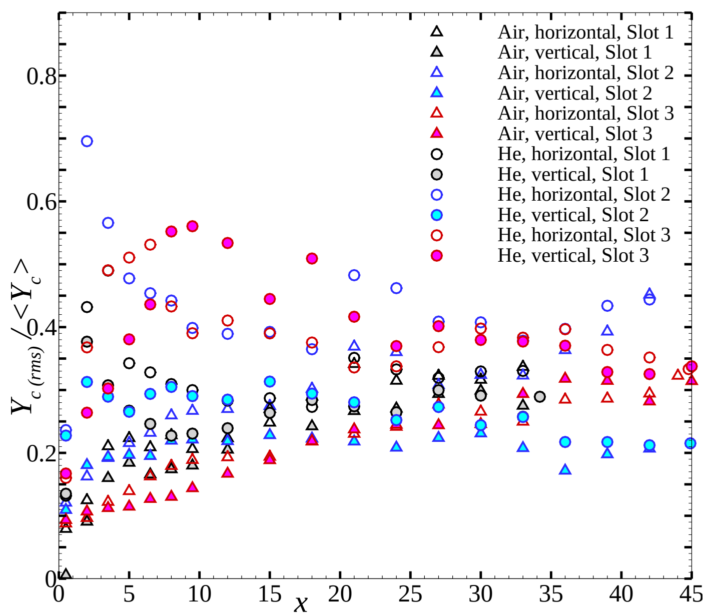

Figure 5.11: Normalized axial evolution of mass fraction fluctuation intensities along jet centrelines, $Y_{c(rms)}/\langle Y_c \rangle$, for experiments. Also shown, for comparison are vertical & horizontal 3D slot 1 jets [107, 108].

Fig. 5.11 shows the normalized axial evolution of the r.m.s. jet gas mass fraction fluctuations (unmixedness), $Y_{c(rms)}/\langle Y_c \rangle$, along the jet centreline, for all experiments. Also shown for comparison are vertical & horizontal slot 1 jets [107, 108]. In the vertical jets, helium slot 2 reached the asymptotic value $\sim 26\%$ at $x = 5D_{eq}$, which is in agreement with the value reported for helium slot 1, which then decreased slightly to the asymptotic value $\sim 21\%$ in the far field ($x > 35D_{eq}$). In contrast, for air slot 2 such a value was recovered only when $x = 8D_{eq}$ and it remained almost the same for the rest of data acquisition domain. It should be noted that this asymptotic value is in agreement with the values reported in literature for the far field of round axisymmetry jets ($\sim 21-24\%$) [83, 15, 93]. In contrast, for the vertical slot 3 cases, helium reached an unmixedness value $\sim 55\%$ where $x = 8D_{eq}$ and then recovered the asymptotic value $\sim 33\%$ in the far field ($x > 38D_{eq}$). The vertical air slot 3 also recovered this asymptotic value beyond the $x > 34D_{eq}$ range. Helium horizontal slot 2 jet also reached a pick unmixedness value of $\sim 70\%$ at $2D_{eq}$ but then decreased to the asymptotic value $\sim 44\%$ beyond the $x > 38D_{eq}$ for the rest of the measurement domain; whereas such a value was not recovered until $x = 41D_{eq}$ for air. For the horizontal slot 3 cases, helium reached an umixedness value $\sim 55\%$ at $x = 7D_{eq}$ and then recovered the asymptotic value $\sim 33\%$ at the end of measurement domain ($x > 43D_{eq}$). Similarly, air horizontal slot 3 jet recovered this value almost the same distance from the slot. This asymptotic value is in agreement with the previous measurement of horizontal slot 1 jets in the far field ($\sim 33\%$) [108].

Slot 2, vertical:

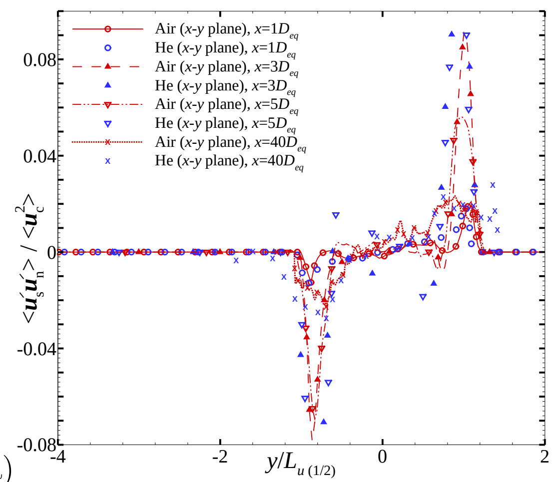

a)

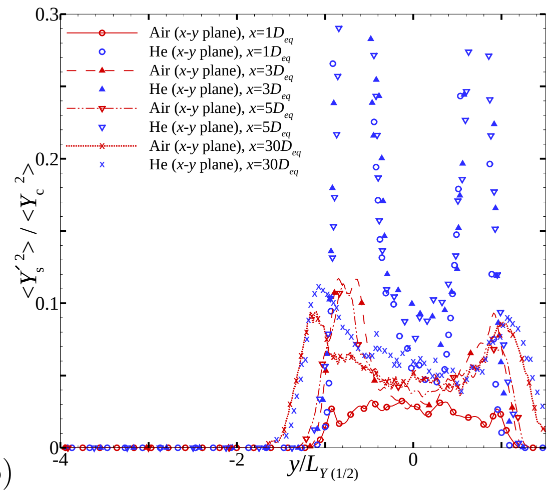

b)

Slot 2, horizontal:

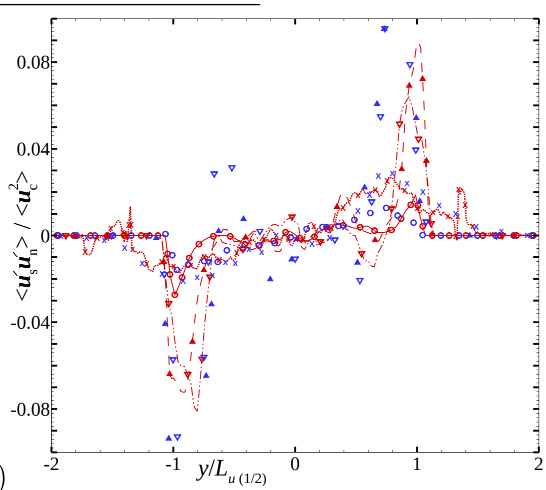

a)

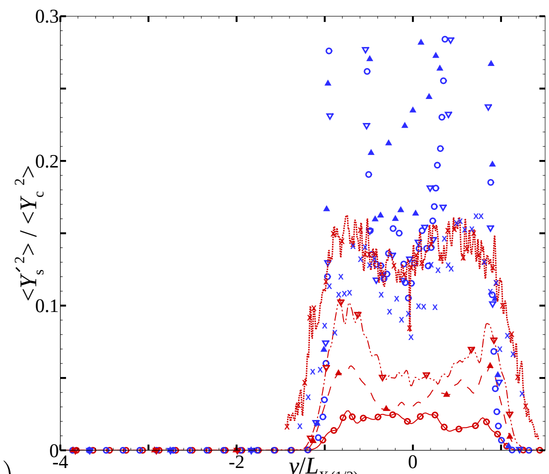

b)

Figure 5.12: a) Normalized time-averaged Reynolds shear stress ($\langle \boldsymbol{u}'_s \boldsymbol{u}'_n \rangle / \langle \boldsymbol{u}_c^2 \rangle$) and b) concentration variance ($\langle Y_s'^2 \rangle / \langle Y_c^2 \rangle$) profiles along jet centrelines for air and helium experiments. Here, the profiles are taken at various heights for air and helium measurements in x-y planes. Note, the legends in horizontal cases are same as the vertical experiments.

Slot 3, vertical:

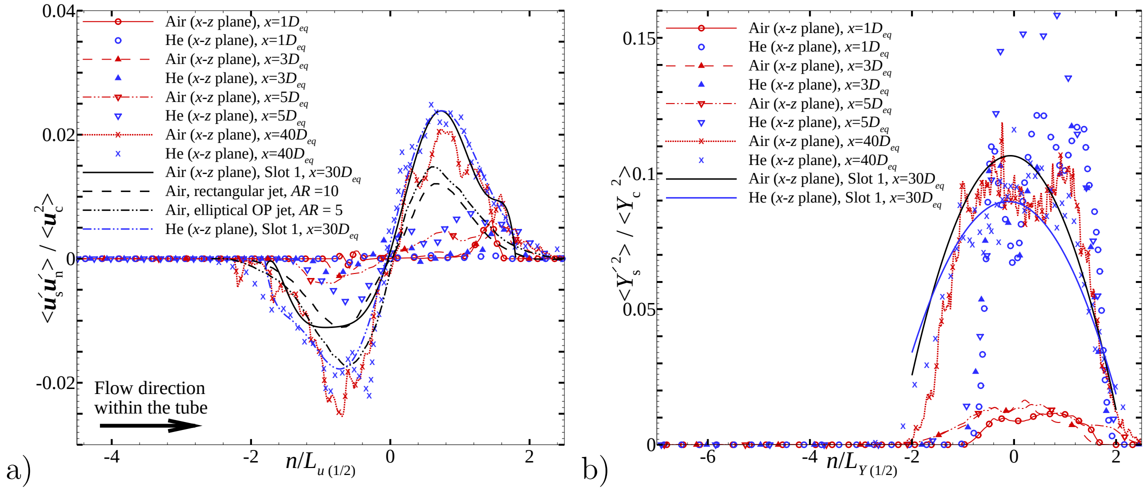

Slot 3, horizontal:

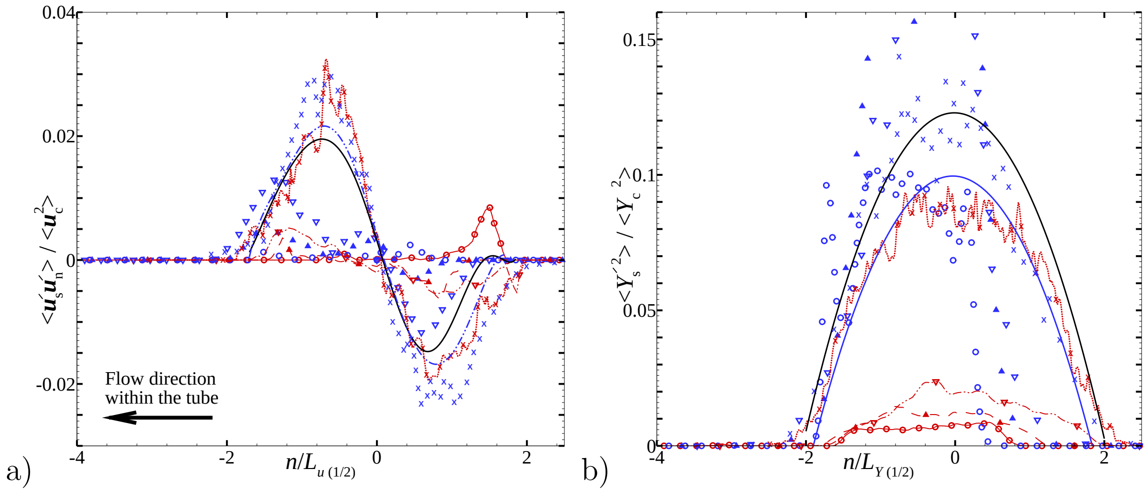

Figure 5.13: a) Normalized time-averaged Reynolds shear stress ($\langle \boldsymbol{u}'_s \boldsymbol{u}'_n \rangle / \langle \boldsymbol{u}_c^2 \rangle$) and b) concentration variance ($\langle Y_s'^2 \rangle / \langle Y_c^2 \rangle$) profiles along jet centrelines for air and helium experiments. Here, the profiles are taken at various heights for air and helium measurements in x-z planes. Note, the flow direction inside the tube illustrated for both vertical and horizontal cases. Also, the legends in horizontal cases are same as the vertical experiments.

Higher order statistics were also acquired for the high-aspect-ratio slot experiments conducted here. The time-averaged Reynolds stress profiles ($\langle \boldsymbol{u}'_s \boldsymbol{u}'_n \rangle$) obtained from slots 2 & 3 measurements, for both vertical and horizontal cases, are presented in Figs. 5.12 - 5.13 a) respectively. Also shown for comparison, in the x-z plane, are vertical & horizontal slots 1, and vertical sharp-edged rectangular (AR=10) and OP elliptical (AR=5) jet measurements [107, 108, 91, 88]. Here, the Reynolds stress quantities have been normalized by the local centreline velocity, $\langle \boldsymbol{u}_c^2 \rangle(s)$. For both slot 2 orientations (Fig. 5.12 a), air and helium jets exhibit higher Reynolds stress compared to the axisymmetric jets in the range of $x \leq 25D_{eq}$; a peak magnitude observed at $x = 3D_{eq}$ for both air and helium cases. Within this range, higher Reynolds stress was observed inside $|n/L_{1/2}| < 1$, with helium having a slightly higher Reynolds stress compared to air. However beyond this range, both air and helium measurements captured the far field self-similar profile well as seen before in slot 1 and the axisymmetric jets [107, 108, 83].

For both slot 3 orientations (Fig. 5.13 a) in the range of $x \leq 15D_{eq}$, air and helium experiments were found to have lower Reynolds stress compared to slot 1 & 2 jets. Also, within $x \leq 5D_{eq}$, higher Reynolds stress was observed beyond $|n/L_{1/2}| < 1$. However, beyond $x \geq 15D_{eq}$, air and helium experiments captured the far field self-similar profile well, with both helium and air having more Reynolds stress compared to the sharp-edged rectangular and OP elliptical jets [91, 88]. Upon comparison of slot 1 & 3 jets, the vertical slot 3 cases recovered and matched the far field self-similar profile of slot 1; whereas, the horizontal slot 3 jets have higher a magnitude of the Reynolds stress compared to slot 1. In general, for all slot 2 & 3 orientations, the magnitudes of Reynolds stress for helium were higher compared to air, more specifically in the near field. It should also be noted that there is an offset of the zero crossing of Reynolds stress profiles form jet centreline ($n/L_{1/2} = 0$) within $1D < x \leq 5D$ for both helium and air measurements in both vertical and horizontal cases. This was previously noted for both vertical and horizontal slot 1 experiments [107, 108]. This brings into question the suitability of conventional eddy-viscosity models for this type of turbulent flow, as this class of turbulence models assumes Reynolds stresses are directly related to the mean strain.

Finally, the normalized mass fraction variance profiles ($\langle Y_s'^2 \rangle / \langle Y_c^2 \rangle$), obtained from slots 2 & 3 measurements, for both vertical and horizontal cases, are presented in Figs. 5.12 - 5.13 b) respectively. In the x-y plane for both slot 2 orientations, helium jet exhibited a semi symmetry saddle-back profile in the whole domain of measurements, whereas air jet showed the same trend only after $x = 1D_{eq}$. In both vertical and horizontal orientations, the maximum magnitude of mass fraction variances were observed at $x \sim 3D_{eq}$ for both gases. Also within $x \leq 5D_{eq}$, the variance peaks were observed inside $|n/L_{1/2}| < 1$. However, both gases return to self-similarity in the far field, with helium having slightly higher magnitude of mass fraction variance compared to air. Also, the magnitude of mass fraction variances were higher in the far field of horizontal cases compared to the vertical orientation. In general, the magnitudes of mass fraction variances for helium were higher compared to air, specially in the near field.

For the vertical slot 3 jets in the x-z plane (Fig. 5.13 b), the initial development of slot jets had a higher variance of mass fraction to the right of the jet centre (in the $+n$ direction aligned with the flow direction within the tube) within the ranges of $x \leq 10D_{eq}$ and $x \leq 6D_{eq}$ for the air and helium jets, respectively. Beyond this range, air jet exhibited semi symmetry saddle-back profile up to $x \leq 25D$ and after this point the variances recovered the semi Gaussian profile; whereas, helium (beyond $x \geq 6D_{eq}$) revealed semi Gaussian profile with a maximum magnitude at $x \sim 10D_{eq}$. In contrast, the initial development of horizontal slot 3 jets had a higher variance of mass fraction to the left of the jet centre (in the $-n$ direction) within the same range found for the vertical cases ($x \leq 10D_{eq}$ and $x \leq 6D_{eq}$ for the air and helium jets, respectively). It should be noted that the initial shifts in variance profiles to the right or left of the jet centre, are consistent between both vertical and horizontal orientation, and aligned with the direction of flow within the tube (see Fig. 5.13). Beyond the range of $x \leq 10D_{eq}$, the horizontal air slot 3 jet revealed semi symmetry saddle-backed profile up to $x \leq 20D$, after this point variances recovered the semi Gaussian profile; whereas, helium (beyond $x \leq 6D_{eq}$) exhibited a semi Gaussian profile with a maximum magnitude at $x \sim 7D_{eq}$. For all slot 3 experiments in the far field, beyond $x \geq 30D_{eq}$ jet heights, mass fraction variances revealed self-similar profile. In general, helium jets exhibited higher magnitudes of mass fraction variances compared to air, more specifically in the near field.

5.5 Discussion

5.5.1 Aspect Ratio effects

Velocity and scalar statistical properties obtained from vertical and horizontal high-aspect-ratio slots 2 & 3 ($AR = 10$) were reported in the previous section. The results were compared to round 3D jet counterparts (slot 1 with $AR = 1$) [107, 108] and with results available in the literature for high-aspect-ratio rectangular ($AR = 10$) and elliptical OP ($AR = 2 - 8$) jets issuing through flat surfaces. It was found that the perpendicular nature of the slot, relative to the direction of flow within the tube, caused a deflection of the jet away from the jet streamwise axis (x-axis).

This deflection is demonstrated in Fig. 5.5, where the jet centreline trajectories, are presented for all slots 1 & 3 jets. Significant deflection, in the direction of flow within the tube were observed in both orientations of slot 1 compared to vertical and horizontal slot 3 experiments. Also, the jet trajectory for the horizontal helium slot 1 jet was found to be described by a power law exponent ~ 1.3, whereas the horizontal helium slot 3 jet's trajectory was found to be described by a nearly linear relation (i.e. power law exponent ~ 1). Upon these observations, it became clear that the aspect ratio is the main player in governing the deflection angle in 3D jets; an increase in the aspect ratio results in a decrease of deflection angle of jets. However, it is not clear yet how the deflection angle scales with the aspect ratio; more measurements with a broad range of aspect ratios are needed to quantify such scales.

As previously observed from the time-averaged velocity and molar concentration contours (Figs. 5.3 - 5.4), slightly shorter potential core length were found for helium ($x \sim 3D_{eq}$) and air ($x \sim 4D_{eq}$) in slot 3 jets compared to $x \sim 4D_{eq}$ and $x \sim 5D_{eq}$ for helium & air slot 1 jets [107, 108], respectively. This is consistent with the very thin vortical structure of high-aspect-ratio slot 3 near the jet exit compared to slot 1, which allows the dynamics of the rolled-up vortical structure to govern the initial development of jet's centre region. In addition, due to the higher entrainment rate that occur in the higher aspect ratio jets, a shorter potential core length and faster decay rate of the jet centreline velocity is expected.

Further interesting observations are made from Fig. 5.6 a), which shows that all slot 1 experiments have a slightly higher velocity decay compared to slot 3 after their potential core region (in the far field beyond $x \leq 5D_{eq}$), as seen previously in OP elliptical jet experiments [55, 88, 90]. But within the range of $x \leq 4D_{eq}$ for helium and $x \leq 5D_{eq}$ for air, all slot 3 experiments demonstrates slightly higher velocity decay rate compared to slot 1 jets. The higher velocity decay rate in the near field region, is more clear in the results reported previously for the sharp-edged rectangular [91] and OP elliptical jets [55] compared to the current slot jets. The non-linear decay region within the near field, called the "characteristic decay" region [102], is significantly influenced by the geometry and aspect ratio of a nozzle. That might be the main reason for the higher velocity decay rates are reported in OP elliptical or rectangular jets compared to slot jets. It should be noted that the reported measurements in rectangular and elliptical jets are limited to the flow emerging through flat surface, where the large curvature on the major axis of the vortical structure plays the main role on the initial development of jet. Whereas in 3D jet, due to the curvature of tube surface (where orifice is machined), dynamics of initial vortical structure may depend on both curvatures of major and minor axes. Three dimensional measurement is required to reveal such complicated vortical dynamics in 3D jets.

The same remarks were also observed from mass fraction decay profiles in Fig. 5.7 a), where slower decay rate was observed in centreline mass fraction for slot 3 in the far field compared to slot 1. The similar observation can also be made from the jet velocity and the scalar width growth presented in Figs. 5.6 - 5.7 b), where all slot 1 experiments experience much higher growth rates in both velocity and scalar fields compared to the slot 3 in the far field. But within the range of $x \sim\leq 8D_{eq}$ faster growth were observed for all slot 3 experiments in the major plane (x-z plane). In general, upon comparison of only two sets of slot aspect ratio (AR= 1 vs AR= 10), higher aspect ratio resulted in a decrease on the jet centreline decay rates and a growth rates on both velocity and scalar fields in the 3D jets, more specifically in the far field.

Upon comparison of the far field's axial evolution of turbulent intensities and unmixedness of slot 3 and 1 along the jet centreline (Figs. 5.10-5.11), all slot 3 jets recovered the asymptotic value of those previously reported for slot 1 jets [107, 108]. These remarks indicate that the far field's development of turbulent intensities and unmixedness in 3D slot jets, same as other jet flows [91, 55], are independent of the slot aspect ratio.

Asymmetric flow pattern were previously reported in the lower side of slot 1 jet's centreline (in the opposite direction of flow within the tube), where more velocity and mass fraction spreading were exhibited near the tail ends of radial profiles ($1\pm < (n/L_{1/2})$) within the range of $x \leq 5D_{eq}$ [107, 108]. It was previously found that the flow separation at the exit of the orifice and the resulting deficits along with the curvature of the tube, relative to the size of the orifice, have contributed to the asymmetric flow patterns observed in the near field of slot 1 jet. Although the flow separation is still persists in all slot 3 jets due to the un-parallelism nature of 3D jet flows, the higher aspect ratio ($AR = 10$) reduced the effects of flow separation and resulting deficits; as a result, the asymmetric patterns toward the edge of jet boundaries were not observed in slot 3 jets. However, the asymmetric patterns were shifted towards the jet centreline ($(n/L_{1/2}) < \pm 1$) within the range of $x \leq 5D_{eq}$ in slot 3 jets, as observed in both radial velocity and scalar profiles (Fig. 5.9).

5.5.2 Buoyancy effects

As previously observed from the jet centreline trajectories (Fig. 5.5), all slot 3 jets experienced a deflection in the jet away from its streamwise axis ($x-$axis). This deflection was also previously reported in slot 1 jets [107, 108], and the major player was found to be the perpendicular streamwise axis of the slot, relative to the flow direction within the tube. As a result, both vertical and horizontal air (heavier gas) slot 3 jets were found to deflect more than their helium (lighter gas) jet counterparts after $x \sim 3D_{eq}$ and $x \sim 4D_{eq}$, respectively. Even though other factors might play a role, the higher deflection of the vertical air jets compared to the vertical helium jets is consistent with the relative strength of the corresponding vertical buoyancy force. However, buoyancy force was clearly the main contributor in the significant deflection of horizontal helium case from the horizontal $x-$axis compared to vertical helium jet in the far field ($x \geq 17D_{eq}$); where such effect were not observed in neither of orientations for air slot 3 jet.

Further interesting observations are made upon comparison of the axial evolution of the turbulent intensities and the unmixedness of slot 3 along the jet centreline (Figs. 5.10-5.11). It was found that helium jets reached the asymptotic values more closer to the orifice at $x = 15D_{eq}$ and $x = 17D_{eq}$ compared to air jets at $x \geq 20D_{eq}$ and $x = 27D_{eq}$ in tangential and orthogonal turbulent intensities, respectively. In axial evolution of unmixedness, while all slot 3 jets would recovered the asymptotic value of $\sim 33\%$ at some distance from the orifice; but the initial increase of the mass fraction fluctuation intensities in the near field occurred more rapidly with lower density gases. These remarks would might be solely associated with the buoyancy effect, which is become the major player in helium jets compared to air jets. It should be noted that such buoyancy effect were also previously observed in slot 1 measurements [107, 108]. Other parameters such as co-flow, initial conditions, Reynolds number, and measurement uncertainty could also influence the evolution of the turbulent intensities and the unmixedness [85]. However, their effects are negligible since the similar experimental system and parameters have been used in current measurements.

5.6 Conclusions

In this study, simultaneous velocity and concentration measurements were conducted in order to investigate vertical and horizontal turbulent jets, of varying gas densities and Reynolds numbers, issuing from a high-aspect-ratio slots machined into the side of a round tube. Two slots with the same aspect ratio ($AR = 10$), as possible crack geometries were considered in this study; although their configurations was aligned parallel to and perpendicular with the direction of flow inside the tube. The fluids considered were air and helium. The results were compared to the previous studies of the vertical and horizontal 3D round jets (slot 1), issuing from the same experimental system and pipeline geometry but with aspect ratio of $AR = 1$ [107, 108]. Comparison was also made to the non-circular jets, OP elliptical and rectangular jets issuing through flat surfaces [91, 90, 55].

By considering flow emerging through a slot, machined on the side of a tube, it was found that the flow arrangement caused a significant deflection from the axis normal to the orifice (streamwise axis, x) as was previously observed in vertical and horizontal slot 1 jets with similar arrangement [107, 108]. For the horizontal helium slot 3 jet, this deflection was found to be initially governed by the density of the gas in the near field, and it has experienced further deflection due to the buoyancy in the far field regardless of the high Froude number ($Fr = 2.8 \times 10^6$). Such deviation due to the buoyancy in the far field was also previously observed for the horizontal helium slot 1. However, such deviation for the horizontal helium slot 3 jet was found to be well described by a nearly linear relation (i.e. power law exponent ~ 1), whereas the horizontal helium slot 1 jet was previously found to have a power law exponent ~ 1.3. This difference may arise due to the higher aspect ratio in slot 3 ($AR = 10$) compared to $AR = 1$ in slot 1. Although other factors might contribute, the lower deflection of all slot 3 jets compared to slot 1 jets is consistent with relative importance of aspect ratio effect in development of 3D jet flows. In general, higher aspect ratio resulted in less deviation for all jets from their streamwise axis (x-axis) and also reduced the order of power law exponent from ~ 1.3 to ~ 1 in the centreline trajectory correlations of horizontal helium slots 1 & 3, respectively. Upon comparison of the only two sets of aspect ratios (AR=1 & AR=10), it also can be generalized that an increase in aspect ratio causes a reduction in the jet centreline decay rates and growth rates on both velocity and scalar fields in the 3D jets, more specifically in the far field. In contrast, the axial evolutions of turbulent intensities and unmixedness of slot 3 jets were found to be independent of the aspect ratio effects, and were reached the similar asymptotic values which are previously reported for slot 1 jets. In addition, a higher aspect ratio reduced the effects of the flow separation at the orifice exit and the resulting deficits in the near field development of slot 3 jets; consequently the asymmetric pattern, which was previously observed close to the edge of slot 1 jet's boundary ($1\pm < (n/L_{1/2})$), was shifted toward the slot 3 jet's centreline ($(n/L_{1/2}) < \pm 1$) within the range of $x \leq 5D_{eq}$ in both radial velocity and scalar profiles.

Chapter 6

Summary and contributions

Hydrogen, as renewable energy vector, is currently viewed as a clean alternative to traditional hydrocarbon-based fuels for transportation and energy storage applications. However, development of modern safety standards for hydrogen infrastructure requires fundamental insight into the physics of buoyant gas dispersion into ambient air. This dissertation assesses the capability of conventional jet assumptions to predict the correct gas dispersion from realistic geometries. A novel piping arrangement considered in this study, where the dispersion of realistic jets which emerged through different orifice geometries located in the side wall of a round tube, perpendicular to the mean flow within the tube. This jet configuration is referred as a 3D jet in this research.

The aim of this dissertation is to provide insight into the flow structures associated with hydrogen outflow from different realistic fuel leak scenarios. For this reason, simultaneous velocity and concentration measurements were conducted in order to investigate turbulent multi-component jets, of varying gas densities and Reynolds numbers, issuing from a round orifice and two high-aspect-ratio slots machined on the side of a round tube. Additionally, large eddy simulation (LES) was also employed to provide additional detail with regards to the three-dimensionality of realistic 3D jets, and also contribute to further insight into the measurements observed trends. The fluids examined numerically and experimentally were helium and air. Hydrogen was also considered for the LES simulation. The broad range of fluid density, Reynolds number, orifice geometry and jet orientation were examined in this study to quantify the effects of buoyancy, initial conditions and orifice geometry on the evolution of 3D jets.

6.1 Key findings

The results of this research demonstrate a crucial need of caution when using conventional jet assumptions to describe the correct dispersion, velocity decay, and ignition limits of a jet emitted from realistic geometries. The detailed findings of this dissertation were discussed in three studies presented as contributions in chapters 3 to 5, and the key findings are summarized as follow:

6.1.1 Vertical round 3D jets

- The flow within the tube, perpendicular to the upward facing round orifice, caused the resulting jet outside the tube to form at a deflection angle relative to the vertical axis, in the direction of the flow within the tube itself.
- The deflection was influenced by the buoyancy of the jet, where heavier gases were found to deflect more than the lighter gases.
- Flow separation inside the tube, at the orifice, and curvature of the tube, relative to the size of the hole, have contributed to the asymmetric flow patterns observed in the round 3D jets.
- Both air and helium round 3D jets experienced significantly more jet spreading compared to the axisymmetric jet experiments.
- In the near field, more jet spreading was observed on the upstream side of the asymmetric 3D jets compared to the axisymmetric case; whereas in the far field, air and helium simulations were found to have substantially more jet spreading along the direction of the pipe, compared to all other directions.
- The enhanced mixing in the asymmetric case caused a reduction in the potential-core length, and an increase in the velocity decay rate.
- Air and helium 3D jet experiments were found to have significantly different patterns in the second-order concentration fluctuations compared to the OP jets.

6.1.2 Horizontal round 3D jets

- The flow arrangement caused a significant deflection from the horizontal axis normal to the orifice as was previously observed in the vertical 3D jets.

- The helium 3D jet deflection was found to be initially governed by the density of the gas in the near field and it experienced further deflection due to buoyancy in the far field. The buoyancy-caused deviation in the far field was found to be reproduced well by a power law expression with the exponent ~ 1.3.

- The realistic leak geometry along with the pipeline orientation considered in this study, caused buoyancy effects to dominate much closer to the orifice than expected for the axisymmetric round jet.

- Buoyancy had a negligible impact on the decay of jet velocity and spreading rates, and centreline velocity fluctuations intensities. However, higher centreline mass fraction fluctuation intensities ($\sim$ 33%) for the horizontal 3D jets compared to the vertical cases ($\sim$ 26%), may have been caused by buoyancy effect.

- Enhanced mixing and entrainment, owing to the asymmetric flow structure and the three-dimensional nature of 3D jets, caused a reduction in the potential-core length, and an increase in both decay and spreading rates of velocity and concentration fields.

- Despite the fact that the orifice geometry is round, the axis-switching phenomenon was observed in the realistic 3D jets, and is believed to be one of the main fundamental mechanisms for the enhanced entrainment properties of the 3D jets.

- The 3D jets, obey the pseudo-similarity decay law with the scaling indicated by the effective diameter. The mass fraction decay along the centreline scaled well with the original effective diameter term ($D_{ef} = D(\frac{\rho_j}{\rho_\infty})^{\frac{1}{2}}$), while the modified version of the effective diameter ($D^*_{ef} = D(\frac{\rho_j}{\rho_\infty})^{0.3}$) provided a more accurate velocity decay profile.

- Turbulent properties, both velocity and scalar, are dependent on the initial jet conditions for all regions of the flow field.

6.1.3 Vertical and horizontal high-aspect-ratio 3D jets

- Once again, realistic pipeline geometry and flow arrangement caused a significant deflection from the jet streamwise axis as was previously observed in the vertical and horizontal round 3D jets with the same arrangement.

- In the far field, the deflection for horizontal helium slot 3 jet was found to be reproduced well by a nearly linear relation (i.e. power law exponent ~ 1), whereas the horizontal helium 3D round jet was found previously to have a power law exponent ~ 1.3.

- Although other factors might contribute, the lower deflection of all high-aspect-ratio 3D jets compared to 3D round jets is consistent with relative importance of aspect ratio effect in development of 3D jet flows.

- Upon comparison of only the two sets of aspect ratios (AR=1 & AR=10), it can also be generalized that an increase in aspect ratio cause a reduction in the jet centreline decay rates and growth rates on both velocity and scalar fields in the high-aspect-ratio 3D jets, more specifically in the far field.

- Also, higher aspect ratio was reduced the effects of flow separation at the orifice exit and the resulting deficits in the near field development of high-aspect-ratio 3D jets; and consequently the asymmetric pattern which was previously observed close to the edge of the 3D round jet's boundary $(1\pm < (n/L_{1/2}))$, was shifted toward the jet centreline $((n/L_{1/2}) < \pm 1)$ within the range of $x \leq 5D_{eq}$ in both radial velocity and scalar profiles.

- However, the axial evolutions of turbulent intensities and unmixedness of high-aspect-ratio 3D jets were found to be independent of the aspect ratio and recovered the asymptotic value of those previously reported for the 3D round jets.

6.2 Future work

The 3D jet experiments were found to have significantly different flow structures and patterns in both velocity and scalar fields compared to the conventional axisymmetry jets. Particularly, the 3D jet measurements revealed remarkable distinct patterns in the second-order concentration fluctuations. Should the development of concentration variance for hydrogen behave the same, ignition of hydrogen may also be influenced by such changes in variance due to the geometries considered. for this reason, future work should consider expanding the measurements domain to a larger flow fields, to capture the far field evolution of realistic leak geometries from practical pipeline or high pressure vessels configurations; in order to determine at what point higher-order self-similarity becomes valid.

A range of fluid density, Reynolds number, orifice geometry and jet orientation are examined in this study to quantify the effects of buoyancy, initial conditions and orifice geometry on the evolution of 3D jets. However, the broader range of these key parameters along with other potential important variables (e.g. co-flow, obstacles and ventilation) should be considered in future studies to precisely parameterized each potential factors and their associated effects on the unintended gas leak from realistic geometries. For example, broader range of gas density and Reynold numbers needed to accurately quantify the deflection angle of 3D jets and the buoyancy effect on it, or much wider range of aspect ratio should be considered to adequately determine the aspect ratio effects on the development of 3D jets.

Further three dimensional measurements will also be required to provide more insight in the development of 3D jet flows in the realistic configurations, and accurately quantify the key parameters on governing the flow structure for 3D jets (i.e. initial conditions, orifice geometry, buoyancy, etc.). Due to measurements limitation and associated uncertainty with the measurements at the orifice, higher resolution simulations of the near-field should also be conducted to fully resolve fine-scale turbulent motions near and at the orifice. However, These recommendations add considerable experimental and computational expense. Finally, higher order statistical analysis as well as scalar flux correlations should also be conducted to provide further insight into the physics of 3D jet flows.

Appendix A

PERMISSION LETTERS FOR COPYRIGHTED MATERIAL

Springer license

This Agreement between Mr. Majid Soleimani nia ("You") and Springer Nature ("Springer Nature") consists of your license details and the terms and conditions provided by Springer Nature and Copyright Clearance Center.

License Number	4456600251713
License date	Oct 26, 2018
Licensed Content Publisher	Springer Nature
Licensed Content Publication	Experiments in Fluids
Licensed Content Title	Digital particle image velocimetry
Licensed Content Author	C. E. Willert, M. Gharib
Licensed Content Date	Jan 1, 1991
Licensed Content Volume	10
Licensed Content Issue	4
Type of Use	Thesis/Dissertation
Requestor type	academic/university or research institute
Format	print and electronic
Portion	figures/tables/illustrations
Number of figures/tables/illustrations	1
Will you be translating?	no
Circulation/distribution	<501
Author of this Springer Nature content	no
Title	Experimental investigation of multi-component jets issuing from model pipeline geometries with application to hydrogen safety
Institution name	University of Victoria
Expected presentation date	Dec 2018
Portions	Figure 5.
Requestor Location	Mr. Majid Soleimani nia University of Victoria Institute for Integrated Energy Systems PO Box 1700 STN CSC Victoria, BC V8W 2Y2 Canada Attn: Mr. Majid Soleimani nia
Billing Type	Invoice
Billing Address	Mr. Majid Soleimani nia University of Victoria Institute for Integrated Energy Systems PO Box 1700 STN CSC Victoria, BC V8W 2Y2 Canada Attn: Mr. Majid Soleimani nia
Total	0.00 CAD

Springer Nature Terms and Conditions for RightsLink Permissions

Springer Nature Customer Service Centre GmbH (the Licensor) hereby grants you a non-exclusive, world-wide licence to reproduce the material and for the purpose and requirements specified in the attached copy of your order form, and for no other use, subject to the conditions below:

1. The Licensor warrants that it has, to the best of its knowledge, the rights to license reuse of this material. However, you should ensure that the material you are requesting is original to the Licensor and does not carry the copyright of another entity (as credited in the published version).

   If the credit line on any part of the material you have requested indicates that it was reprinted or adapted with permission from another source, then you should also seek permission from that source to reuse the material.

2. Where **print only** permission has been granted for a fee, separate permission must be obtained for any additional electronic re-use.

3. Permission granted **free of charge** for material in print is also usually granted for any electronic version of that work, provided that the material is incidental to your work as a whole and that the electronic version is essentially equivalent to, or substitutes for, the print version.

4. A licence for 'post on a website' is valid for 12 months from the licence date. This licence does not cover use of full text articles on websites.

5. Where **'reuse in a dissertation/thesis'** has been selected the following terms apply: Print rights of the final author's accepted manuscript (for clarity, NOT the published version) for up to 100 copies, electronic rights for use only on a personal website or institutional repository as defined by the Sherpa guideline (www.sherpa.ac.uk/romeo/).

6. Permission granted for books and journals is granted for the lifetime of the first edition and does not apply to second and subsequent editions (except where the first edition permission was granted free of charge or for signatories to the STM Permissions Guidelines http://www.stm-assoc.org/copyright-legal-affairs/permissions/permissions-guidelines/), and does not apply for editions in other languages unless additional translation rights have been granted separately in the licence.

7. Rights for additional components such as custom editions and derivatives require additional permission and may be subject to an additional fee. Please ap-

ply to Journalpermissions@springernature.com/bookpermissions@springernature.com for these rights.

8. The Licensor's permission must be acknowledged next to the licensed material in print. In electronic form, this acknowledgement must be visible at the same time as the figures/tables/illustrations or abstract, and must be hyperlinked to the journal/book's homepage. Our required acknowledgement format is in the Appendix below.

9. Use of the material for incidental promotional use, minor editing privileges (this does not include cropping, adapting, omitting material or any other changes that affect the meaning, intention or moral rights of the author) and copies for the disabled are permitted under this licence.

10. Minor adaptations of single figures (changes of format, colour and style) do not require the Licensor's approval. However, the adaptation should be credited as shown in Appendix below.

LaVision license

Dr. Steve Anderson
LaVision Inc.
211 W. Michigan Ave. Suite 100
Ypsilanti, MI 48197, USA

October 26, 2018

Majid Soleimani nia
Institute for Integrated Energy Systems(IESVic)
Department of Mechanical Engineering
University of Victoria

Dear Dr. Steve Anderson,

I am completing a PhD dissertation at the University of Victoria, British Columbia, Canada, entitled "Experimental investigation of multi-component jets issuing from model pipeline geometries with application to hydrogen safety." I would like your permission to reprint in my dissertation an image from the following:

LaVision. GaseousLIF. LaVision GmbH, Davis 8.4 edition, March 2017. Manual No. 1004077.

The image to be reproduced is:

Figure 4.36: Workflow for 1-color LIF concentration measurements

The requested permission extends to any future revisions and editions of my dissertation, including non-exclusive world rights in all languages, and to the prospective publication of my dissertation by the National Library of Canada and Proquest. Dissertations published at the University of Victoria are also made digitally available on the Internet for public access via the university's Institutional Repository (UVi Space). For more information on the UVic Space see: https://dspace.library.uvic.ca:8443/.

These rights will in no way restrict republication of the material in any other form by you or by others authorized by you. Your signing of this letter will also confirm that you own (or your company owns) the copyright to the above-described material.

If these arrangements meet with your approval, please sign this letter where indicated below and return to me in the enclosed return envelope. Thank you very much.

Sincerely,

Majid Soleimani nia

PERMISSION GRANTED FOR THE USE REQUESTED ABOVE:

Bibliography

[1] R.J. Adrian and J. Westerweel. *Particle Image Velocimetry*. Cambridge University Press, 2011.

[2] M. Amielh, T. Djeridane, F. Anselmet, and L. Fulachier. Velocity near-field of variable density turbulent jets. *International Journal of Heat and Mass Transfer*, 39(10):2149–2164, 1996.

[3] R. A. Antonia and Q. Zhao. Effect of initial conditions on a circular jet. *Experiments in Fluids*, 31(3):319–323, 2001.

[4] A. Ash. Quantitative imaging of multi-component turbulent jets. Master's thesis, University of Victoria, April 2012.

[5] C.G. Ball, H. Fellouah, and A. Pollard. The flow field in turbulent round free jets. *Progress in Aerospace Sciences*, 50:1 – 26, 2012.

[6] H. A. Becker, H. C. Hottel, and G. C. Williams. The nozzle-fluid concentration field of the round, turbulent , free jet. *Journal of Fluid Mechanics*, 30:285–303, 1967.

[7] Sahand Behboodi, David P. Chassin, Curran Crawford, and Ned Djilali. Renewable resources portfolio optimization in the presence of demand response. *Applied Energy*, 162:139 – 148, 2016.

[8] Julius S Bendat and Allan G Piersol. *Random data: analysis and measurement procedures*, volume 729. John Wiley & Sons, 2011.

[9] L. H. Benedict and R. D. Gould. Towards better uncertainty estimates for turbulence statistics. *Experiments in Fluids*, 22(2):129–136, Dec 1996.

[10] B. J. Boersma, G. Brethouwer, and F. T. M. Nieuwstadt. A numerical investigation on the effect of the inflow conditions on the self-similar region of a round jet. *Physics of Fluids*, 10(4):899–909, 1998.

[11] C Bogey and C Bailly. *Direct and Large-Eddy Simulation VII*, chapter A Study of the Influence of the Reynolds Number on Jet Self-Similarity Using Large-Eddy Simulation, pages 13–18. Springer, 2010.

[12] Francesco Bonelli, Annarita Viggiano, and Vinicio Magi. How does a high density ratio affect the near- and intermediate-field of high-re hydrogen jets? *International Journal of Hydrogen Energy*, 41(33):15007 – 15025, 2016.

[13] G. Carazzo, E. Kaminski, and S. Tait. The route to self-similarity in turbulent jets and plumes. *Journal of Fluid Mechanics*, 547:137–148, 2006.

[14] V K Chakravarthy and S Menon. Linear eddy simulations of Reynolds number and Schmidt number effects on turbulent scalar mixing. *Physics of Fluids*, 13:488–499, 2001.

[15] C. J. Chen and W. Rodi. *Vertical turbulent buoyant jets : a review of experimental data*. Pergamon Press, Oxford; New York, 1980.

[16] B. Chernyavsky, P. Benard, P. Oshkai, and N. Djilali. Numerical investigation of subsonic hydrogen jet release. *International Journal of Hydrogen Energy*, 39(11):6242 – 6251, 2014.

[17] B. Chernyavsky, T. C. Wu, F. Pèneau, P. Bènard, P. Oshkai, and N. Djilali. Numerical and experimental investigation of buoyant gas release: Application to hydrogen jets. *International Journal of Hydrogen Energy*, 36(3):2645–2655, 2011.

[18] Hugh W Coleman and W Glenn Steele. *Experimentation, validation, and uncertainty analysis for engineers*. John Wiley & Sons, 2018.

[19] H F Coward and G W Jones. Limits of flammability of gases and vapors. pittsburgh, pa: Us department of the interior, bureau of mines. *Bulletin*, 503, 1952.

[20] Fabrizio De Gregorio. Free compressible jet investigation. *Experiments in Fluids*, 55(3):1693, 2014.

[21] J R DeBonis and J N Scott. Large eddy simulation of a turbulent compressible round jet. *AIAA Journal*, 40 (7):1346–1354, 2002.

[22] R. C. Deo, J. Mi, and G. J. Nathan. The influence of nozzle aspect ratio on plane jets. *Experimental Thermal and Fluid Science*, 31(8):825–838, 2007.

[23] Ravinesh C. Deo, Jianchun Mi, and Graham J. Nathan. The influence of reynolds number on a plane jet. *Physics of Fluids*, 20(7):075108, 2008.

[24] PAUL E. DIMOTAKIS. The mixing transition in turbulent flows. *Journal of Fluid Mechanics*, 409:69–98, 2000.

[25] T Djeridane, M Amielh, F Anselmet, and L Fulachier. Velocity turbulence properties in the near-field region of axisymmetric variable density jets. *Physics of Fluids*, 8 (6):1614–1630, 1996.

[26] C D Donaldson and K E Gray. Theoretical and experimental investigation of the compressible free mixing of two dissimilar gases. *AIAA Journal*, 4 (11):2017–2025, 1966.

[27] D. R. Dowling and P. E. Dimotakis. Similarity of the concentration field of gas-phase turbulent jets. *Journal of Fluid Mechanics*, 218:109, 1990.

[28] J M Eggels, F Unger, M H Weiss, J Westerweel, R J Adrian, R Friedrich, and F T M Nieuwstadt. Fully developed turbulent pipe flow: a comparison between direct numerical simulation and experiment. *Journal of Fluid Mechanics*, 268:175–209, 1994.

[29] I. W. Ekoto, W. G. Houf, G. H. Evans, E. G. Merilo, and M. A. Groethe. Experimental investigation of hydrogen release and ignition from fuel cell powered forklifts in enclosed spaces. *International Journal of Hydrogen Energy*, 37(22):17446 – 17456, 2012. HySafe 1.

[30] K. W. Everitt and A. G. Robins. The development and structure of turbulent plane jets. *Journal of Fluid Mechanics*, 88(3):563583, 1978.

[31] S A E G Falle. Self-similar jets. *Mon. Not. R. Astr. Soc.*, 250:581–596, 1991.

[32] S A E G Falle and J R Giddings. *Numerical Methods for Fluid Dynamics IV*, chapter Body capturing using adaptive cartesian grids, pages 337–343. Oxford University Press, 1993.

[33] S A E G Falle and S S Komissarov. An upwind numerical scheme for relativistic hydrodynamics with a general equation of state. *Mon. Not. R. Astron. Soc.*, 278:586–602, 1996.

[34] H. Fellouah, C.G. Ball, and A. Pollard. Reynolds number effects within the development region of a turbulent round free jet. *International Journal of Heat and Mass Transfer*, 52(1718):3943 – 3954, 2009. Special Issue Honoring Professor D. Brian Spalding.

[35] W. K. George. The self-preservation of turbulent flows and its relation to initial conditions and coherent structures. *Advances in turbulence (Arndt, R. E. A. & George, W. K., Eds.)*, pages 39–73, 1989.

[36] M. Gharib and A. Roshko. The effect of flow oscillations on cavity drag. *Journal of Fluid Mechanics*, 177:501–530, 1987.

[37] J J Gottlieb and C P T Groth. Assessment of Riemann solvers for unsteady one-dimensional inviscid flows of perfect gases. *Journal of Computational Physics*, 78:437–458, 1988.

[38] Manuel Götz, Jonathan Lefebvre, Friedemann Mörs, Amy McDaniel Koch, Frank Graf, Siegfried Bajohr, Rainer Reimert, and Thomas Kolb. Renewable power-to-gas: A technological and economic review. *Renewable Energy*, 85:1371 – 1390, 2016.

[39] E W Grandmaison, D E Rathgeber, and H A Becker. Some characteristics of concentration fluctuations in free turbulent jets. *Canadian Journal of Chemical Engineering*, 60:212–219, 1982.

[40] F. F. Grinstein, E. Gutmark, and T. Parr. Near field dynamics of subsonic free square jets. a computational and experimental study. *Physics of Fluids*, 7(6):1483–1497, 1995.

[41] E. Gutmark, K. C. Schadow, T. P. Parr, D. M. Hanson-Parr, and K. J. Wilson. Noncircular jets in combustion systems. *Experiments in Fluids*, 7(4):248–258, 1989/02/01 1989.

[42] E. Gutmark and I. Wygnanski. The planar turbulent jet. *Journal of Fluid Mechanics*, 73(3):465495, 1976.

[43] E. J. Gutmark and F. F. Grinstein. Flow control with noncircular jets. *Annual Review of Fluid Mechanics*, 31(1):239–272, 1999.

[44] Ephraim Gutmark and Klaus C. Schadow. Flow characteristics of orifice and tapered jets. *The Physics of Fluids*, 30(11):3448–3454, 1987.

[45] Y. Hajji, B. Jouini, M. Bouteraa, A. Elcafsi, A. Belghith, and P. Bournot. Numerical study of hydrogen release accidents in a residential garage. *International Journal of Hydrogen Energy*, 40(31):9747 – 9759, 2015.

[46] Sang Heon Han, Daejun Chang, and Jong Soo Kim. Experimental investigation of highly pressurized hydrogen release through a small hole. *International Journal of Hydrogen Energy*, 39(17):9552 – 9561, 2014.

[47] Ronald K. Hanson, Jerry M. Seitzman, and Phillip H. Paul. Planar laser-fluorescence imaging of combustion gases. *Applied Physics B*, 50(6):441–454, Jun 1990.

[48] D. P. Hart. Piv error correction. *Experiments in Fluids*, 29(1):13–22, Jul 2000.

[49] William C Hinds. *Aerosol technology: properties, behavior, and measurement of airborne particles*. John Wiley & Sons, 2nd edition, 2012.

[50] J. 0. HINZE. *Turbulence*. McGraw-Hill, 1975.

[51] Thomas Y. Hou and Philippe G. Le Floch. Why nonconservative schemes converge to wrong solutions: Error analysis. *Mathematics of Computation*, 62(206):497–530, April 1994.

[52] W. Houf and R. Schefer. Analytical and experimental investigation of small-scale unintended releases of hydrogen. *International Journal of Hydrogen Energy*, 33(4):1435 – 1444, 2008.

[53] W. Houf, R. Schefer, G. Evans, E. Merilo, and M. Groethe. Evaluation of barrier walls for mitigation of unintended releases of hydrogen. *International Journal of Hydrogen Energy*, 35(10):4758 – 4775, 2010. Novel Hydrogen Production Technologies and Applications.

[54] W.G. Houf, G.H. Evans, I.W. Ekoto, E.G. Merilo, and M.A. Groethe. Hydrogen fuel-cell forklift vehicle releases in enclosed spaces. *International Journal of Hydrogen Energy*, 38(19):8179 – 8189, 2013.

[55] Fazle Hussain and Hyder S. Husain. Elliptic jets. part 1. characteristics of unexcited and excited jets. *Journal of Fluid Mechanics*, 208:257–320, 1989.

[56] H. J. Hussein, S. P. Capp, and W. K. George. Velocity measurements in a high-reynolds-number, momentum-conserving, axisymmetric, turbulent jet. *Journal of Fluid Mechanics*, 258:31–75, 1994.

[57] D. Iverson, J. DeVaal, J. Kerr, and P. Oshkai. Investigation of ignited hydrogen leaks from tube fittings. *International Journal of Hydrogen Energy*, 40(38):13134 – 13145, 2015.

[58] Ronald J. Adrian Jerry Westerweel, Gerrit E. Elsinga. Particle image velocimetry for complex and turbulent flows. *Annual Review of Fluid Mechanics*, 45(1):409–436, 2013.

[59] J D Kapner, K Li, and R H Larson. An experimental study of mixing phenomena of turbulent supersonic jets. *International Journal of Heat and Mass Transfer*, 13:932–937, 1970.

[60] R D Keane and R J Adrian. Optimization of particle image velocimeters. i. double pulsed systems. *Measurement Science and Technology*, 1(11):1202, 1990.

[61] M Klein, A Sadiki, and J Janicka. A digital filter based generation of inflow data for spatially developing direct numerical or large eddy simulations. *Journal of Computational Physics*, 186:652–665, 2003.

[62] N. Kotchourko, M. Kuznetsov, A. Kotchourko, J. Grune, A. Lelyakin, and T. Jordan. Concentration measurements in a round hydrogen jet using background oriented schlieren (bos) technique. *International Journal of Hydrogen Energy*, 39(11):6201 – 6209, 2014.

[63] LaVision. *FlowMaster*. LaVision GmbH, Davis 8.4 edition, January 2017. Manual No. 1003005.

[64] LaVision. *GaseousLIF*. LaVision GmbH, Davis 8.4 edition, March 2017. Manual No. 1004077.

[65] R J Leveque. *Finite Volume Methods for Hyperbolic Problems*. Cambridge University Press, New York, 2002.

[66] B. Lewis and G. von Elbe. *Combustion, Flames and Explosions of Gases*. Academic Press, New York, second edition, 1961.

[67] G. Lipari and P. K. Stansby. Review of experimental data on incompressible turbulent round jets. *Flow, Turbulence and Combustion*, 87(1):79–114, Jul 2011.

[68] A. Lozano. *Laser-Excited Luminescent Tracers for Planar Concentration Measurements in Gaseous Jets*. PhD thesis, STANFORD UNIVERSITY., 1992.

[69] a. Lozano, B. Yip, and R.K. Hanson. Acetone: a tracer for concentration measurements in gaseous flows by planar laser-induced fluorescence. *Experiments in Fluids*, 13:369–376, 1992.

[70] C. L. Lubbers, G. Brethouwer, and B. J. Boersma. Simulation of the mixing of a passive scalar in a round turbulent jet. *Fluid Dynamics Research*, 28(3):189, 2001.

[71] Humrutha G. M. Kaushik, R. Kumar. Review of computational fluid dynamics studies on jets. *American Journal of Fluid Dynamic*, 5(A):1–11, 2015.

[72] B. Maxwell, M. Soleimani nia, P. Oshkai, and N. Djilali. Large eddy simulations of asymmetric turbulent hydrogen jets issuing from realistic pipe geometries. In *Proceedings of the 7th International Conference on Hydrogen Safety, Hamburg, Germany*, 2017.

[73] Anthony John Meares. *An experimental study of gas leak jets relevant to offshore structures.* PhD thesis, University of Herfordshire, 1998.

[74] J. Mi, P. Kalt, G. J. Nathan, and C. Y. Wong. Piv measurements of a turbulent jet issuing from round sharp-edged plate. *Experiments in Fluids*, 42(4):625–637, 2007.

[75] J. Mi and G. J. Nathan. Statistical properties of turbulent free jets issuing from nine differently-shaped nozzles. *Flow, Turbulence and Combustion*, 84(4):583–606, 2010/06/01 2010.

[76] J. Mi, G. J. Nathan, and D. S. Nobes. Mixing characteristics of axisymmetric free jets from a contoured nozzle, an orifice plate and a pipe. *Journal of Fluids Engineering*, 123(4):878–883, June 2001.

[77] J. Mi, D. S. Nobes, and G. J. Nathan. Influence of jet exit conditions on the passive scalar field of an axisymmetric free jet. *Journal of Fluid Mechanics*, 432:91–125, 2001.

[78] R. S. Miller, C. K. Madnia, and P. Givi. Numerical simulation of non-circular jets. *Computers & Fluids*, 24(1):1–25, 1995.

[79] S M Mitran. Adaptive mesh refinement computation of turbulent flows - pitfalls and escapes. In N V Pogorelov, E Audit, P Colella, and G P Zank, editors, *Numerical Modeling of Space Plasma Flows: ASTRONUM 2008*, volume 406, pages 249–254. ASP Conf. Series, 2009.

[80] P. Moin. Advances in large eddy simulation methodology for complex flows. *International Journal of Heat and Fluid Flow*, 23:710, 2002.

[81] G.J. Nathan, J. Mi, Z.T. Alwahabi, G.J.R. Newbold, and D.S. Nobes. Impacts of a jet's exit flow pattern on mixing and combustion performance. *Progress in Energy and Combustion Science*, 32(56):496 – 538, 2006.

[82] N. R. Panchapakesan and J. L. Lumley. Turbulence measurements in axisymmetric jets of air and helium. part 1. air jet. *Journal of Fluid Mechanics*, 246:197–223, 1993.

[83] N. R. Panchapakesan and J. L. Lumley. Turbulence measurements in axisymmetric jets of air and helium. part 2. helium jet. *Journal of Fluid Mechanics*, 246:225–247, 1993.

[84] W. M. Pitts. *Effects of global density and Reynolds number variations on mixing in turbulent, axisymmetric jets*. NBSIR 86-3340. National Bureau of Standards, US Department of Commerce, 1986.

[85] W. M. Pitts. Effects of global density ratio on the centerline mixing behavior of axisymmetric turbulent jets. *Experiments in Fluids*, 11(2):125–134, 1991.

[86] W. M. Pitts. Reynolds number effects on the mixing behavior of axisymmetric turbulent jets. *Experiments in Fluids*, 11(2):135–141, 1991.

[87] F. Pneau, G. Pedro, P. Oshkai, P. Bnard, and N. Djilali. Transient supersonic release of hydrogen from a high pressure vessel: A computational analysis.

International Journal of Hydrogen Energy, 34(14):5817 – 5827, 2009. 2nd International Conference on Hydrogen Safety.

[88] W. R. Quinn. On mixing in an elliptic turbulent free jet. *Physics of Fluids A*, 1(10):1716, 1989.

[89] W. R. Quinn. Upstream nozzle shaping effects on near field flow in round turbulent free jets. *European Journal of Mechanics - B/Fluids*, 25(3):279–301, 2006.

[90] W. R. Quinn. Experimental study of the near field and transition region of a free jet issuing from a sharp-edged elliptic orifice plate. *European Journal of Mechanics - B/Fluids*, 26(4):583–614, 2007.

[91] W.R. Quinn. Turbulent free jet flows issuing from sharp-edged rectangular slots: The influence of slot aspect ratio. *Experimental Thermal and Fluid Science*, 5(2):203 – 215, 1992.

[92] M. Raffel, C.E. Willert, S.T. Wereley, and J. Kompenhans. *Particle Image Velocimetry: A Practical Guide*. Springer, 2007.

[93] C. D. Richards and W. M. Pitts. Global density effects on the self-preservation behaviour of turbulent free jets. *Journal of Fluid Mechanics*, 254:417435, 1993.

[94] W. Rodi. *Turbulent buoyant jets and plumes*. Pergamon Press, Oxford; New York, 1st edition, 1982.

[95] G. P. ROMANO and R. A. ANTONIA. Longitudinal and transverse structure functions in a turbulent round jet: effect of initial conditions and reynolds number. *Journal of Fluid Mechanics*, 436:231248, 2001.

[96] R. W. Schefer, W. G. Houf, and T. C. Williams. Investigation of small-scale unintended releases of hydrogen: Buoyancy effects. *International Journal of Hydrogen Energy*, 33(17):4702–4712, 2008.

[97] R. W. Schefer, W. G. Houf, and T. C. Williams. Investigation of small-scale unintended releases of hydrogen: momentum-dominated regime. *International Journal of Hydrogen Energy*, 33(21):6373–6384, 2008.

[98] R. W. Schefer, W. G. Houf, T. C. Williams, B. Bourne, and J. Colton. Characterization of high-pressure, underexpanded hydrogen-jet flames. *International Journal of Hydrogen Energy*, 32(12):2081–2093, 2007.

[99] A. Sciacchitano and B. Wieneke. Piv uncertainty propagation. *Measurement Science and Technology*, 27(8):084006, 2016.

[100] Andrea Sciacchitano, Douglas R Neal, Barton L Smith, Scott O Warner, Pavlos P Vlachos, Bernhard Wieneke, and Fulvio Scarano. Collaborative framework for piv uncertainty quantification: comparative assessment of methods. *Measurement Science and Technology*, 26(7):074004, 2015.

[101] J. M. Seitzman and R. K. Hanson. *Planar Fluorescence Imaging: Basic Concepts for Scalar and Velocity Measurements*, pages 137–157. Springer Netherlands, Dordrecht, 1992.

[102] P. M. Sforza and W. Stasi. Heated three-dimensional turbulent jets. *Journal of Heat Transfer*, 101(2):353, 1979.

[103] K M Shyue. An efficient shock-capturing algorithm for compressible multicomponent problems. *Journal of Computational Physics*, 142:208–242, 1998.

[104] R. M. C. So, J. Y. Zhu, M. V. tgen, and B. C. Hwang. Some measurements in a binary gas jet. *Experiments in Fluids*, 9(5):273–284, 1990.

[105] M. Soleimani nia, B. Maxwell, P. Oshkai, and N. Djilali. Measurements of flow velocity and scalar concentration in turbulent multi-component jets. In *Proceedings of the 7th International Conference on Hydrogen Safety, Hamburg, Germany*, 2017.

[106] M. Soleimani nia, B. Maxwell, P. Oshkai, and N. Djilali. Buoyancy effect on the velocity and concentration distributions in turbulent multi-component jets issuing from a pipe with a realistic leak geometry. In *Proceedings of 9th International Symposium on Fluid-Structure Interactions, Flow-Sound Interactions, Flow-Induced Vibration & Noise, Toronto, Canada*, July 2018.

[107] M. Soleimani nia, B. Maxwell, P. Oshkai, and N. Djilali. Experimental and Numerical Investigation of Turbulent Jets Issuing Through a Realistic Pipeline Geometry: Asymmetry Effects for Air, Helium, and Hydrogen. *International Journal of Hydrogen Energy*, 43(19):9379–9398, May 2018.

[108] M. Soleimani nia, B. Maxwell, P. Oshkai, and N. Djilali. Measurements of Flow Velocity and Scalar Concentration in Turbulent Multi-component Jets: Asymmetry and Buoyancy Effects. *ArXiv e-prints*, November 2018.

[109] M. Soleimani nia, P. Oshkai, and N. Djilali. Multi-Component High Aspect Ratio Turbulent Jets Issuing from Non-Planar Nozzles. *ArXiv e-prints*, November 2018.

[110] L. K. Su and N. T. Clemens. The structure of fine-scale scalar mixing in gas-phase planar turbulent jets. *Journal of Fluid Mechanics*, 488:1–29, 2003.

[111] L. K. Su, D. B. Helmer, and C. J. Brownell. Quantitative planar imaging of turbulent buoyant jet mixing. *Journal of Fluid Mechanics*, 643:59–95, 2010.

[112] H Suto, K Matusara, M Kobayashi, and Y Kaneko. Large eddy simulation of flow and scalar transport in a round jet. *Heat TransferAsian Research*, 33 (3):175–188, 2004.

[113] N Tajallipour, V Kumar, and M Paraschivoiu. Large-eddy simulation of a compressible free jet flow on unstructured elements. *International Journal of Numerical Methods for Heat & Fluid Flow*, 23 (2):336–354, 2013.

[114] B. Talbot, N. Mazellier, B. Renou, L. Danaila, and M. Boukhalfa. Time-resolved velocity and concentration measurements in variable-viscosity turbulent jet flow. *Experiments in Fluids*, 47(4-5):769–787, 2009/10/01 2009.

[115] Christopher K. W. Tam and Andrew T. Thies. Instability of rectangular jets. *Journal of Fluid Mechanics*, 248:425448, 1993.

[116] J C Tannehill, D A Anderson, and R H Pletcher. *Computational Fluid Mechanics and Heat Transfer*. CRC Press, 2nd edition, 1997.

[117] M. W. Thring and M. P. Newby. Combustion length of enclosed turbulent jet flames. *Symposium (International) on Combustion*, 4(1):789 – 796, 1953. Fourth Symposium (International) on Combustion.

[118] Walter Tollmien. Berechnung turbulenter ausbreitungsvorgnge. *ZAMM - Journal of Applied Mathematics and Mechanics / Zeitschrift fr Angewandte Mathematik und Mechanik*, 6(6):468–478, 1926.

[119] A. A. TOWNSEND. *The Structure of Turbulent Shear Flow.* Cambridge University Press, 1976.

[120] I. van Cruyningen, A. Lozano, and R. K. Hanson. Quantitative imaging of concentration by planar laser-induced fluorescence. *Experiments in Fluids*, 10(1):41–49, 1990/10/01 1990.

[121] B van Leer. Towards the ultimate conservative difference scheme III. Upstream-centered finite-difference schemes for ideal compressible flow. *Journal of Computational Physics*, 23:263–275, 1977.

[122] M Vanella, U Piomelli, and E Balaras. Effect of grid discontinuities on large-eddy simulation statistics and flow fields. *Journal of Turbulence*, 9: 32:1–23, 2008.

[123] A. Veser, M. Kuznetsov, G. Fast, A. Friedrich, N. Kotchourko, G. Stern, M. Schwall, and W. Breitung. The structure and flame propagation regimes in turbulent hydrogen jets. *International Journal of Hydrogen Energy*, 36(3):2351–2359, February 2011.

[124] J. C. Vogel and J. K. Eaton. Combined heat transfer and fluid dynamic measurements downstream of a backward-facing step. *Journal of Heat Transfer*, 107(4):922–929, November 1985.

[125] S.J Wakes, A.E Hold, and A.J Meares. Experimental investigation of the effect orifice shape and fluid pressure has on high aspect ratio cross-sectional jet behaviour. *Journal of Hazardous Materials*, 89(1):1 – 27, 2002.

[126] J Westerweel. Fundamentals of digital particle image velocimetry. *Measurement Science and Technology*, 8(12):1379, 1997.

[127] B. Wieneke and K. Pfeiffer. Adaptive PIV with variable interrogation window size and shape. In *15th Int Symp on Applications of Laser Techniques to Fluid Mechanics, Lisbon, Portugal*, 2010.

[128] Bernhard Wieneke. Piv uncertainty quantification from correlation statistics. *Measurement Science and Technology*, 26(7):074002, 2015.

[129] C. E. Willert and M. Gharib. Digital particle image velocimetry. *Experiments in Fluids*, 10(4):181–193, Jan 1991.

[130] P. O. Witze. Centerline Velocity Decay of Compressible Free Jets. *AIAA Journal*, 12:417–418, April 1974.

[131] I. Wygnanski and H. Fiedler. Some measurements in the self-preserving jet. *Journal of Fluid Mechanics*, 38(03):577–612, 1969.

[132] J. Xiao, J.R. Travis, and W. Breitung. Hydrogen release from a high pressure gaseous hydrogen reservoir in case of a small leak. *International Journal of Hydrogen Energy*, 36(3):2545 – 2554, 2011. The Third Annual International Conference on Hydrogen Safety.

[133] G. Xu and R. Antonia. Effect of different initial conditions on a turbulent round free jet. *Experiments in Fluids*, 33(5):677–683, 2002/11/01 2002.

[134] K. B. M. Q. Zaman. Asymptotic spreading rate of initially compressible jets-experiment and analysis. *Physics of Fluids*, 10(10):2652–2660, 1998.

[135] K. B. M. Q. Zaman. Spreading characteristics of compressible jets from nozzles of various geometries. *Journal of Fluid Mechanics*, 383:197–228, 1999.

[136] K.B.M.Q. Zaman. Spreading characteristics and thrust of jets from asymmetric nozzles. *AIAA*, (96-0200), 1996.